CHALMERS
UNIVERSITY OF TECHNOLOGY

Hydro-dynamic design, system design and control system for a model-scale foiling boat

Joint project with SSRS & SSPA

Master's thesis in Naval Architecture & Ocean Engineering

Nils Lundqvist
Elias L. Favrum

DEPARTMENT OF MECHANICS & MARITIME SCIENCES
CHALMERS UNIVERSITY OF TECHNOLOGY
Gothenburg, Sweden 2022
www.chalmers.se

Master's thesis in naval architecture & ocean engineering

Hydrodynamic design, system design and control system for a model-scale foiling boat

Nils Lundqvist
Elias L. Favrum

CHALMERS
UNIVERSITY OF TECHNOLOGY

Department of Mechanics and Maritime Sciences
Division of Marine Technology
Chalmers University of Technology
Gothenburg, Sweden 2022

Hydrodynamic design, system design and control system for a model-scale foiling boat
NILS LUNDQVIST
ELIAS L. FAVRUM

Master's thesis 2022:15
Department of Mechanics & Maritime Sciences
Division of Marine Technology
Chalmers University of Technology
SE-412 96 Göteborg
Sweden
Telephone: +46 (0)31-772 1000

Cover: Model-scale foiling boat sitting on the wings by Rådasjön lake during field testing.

Typeset in LaTeX
Gothenburg, Sweden 2022

Hydrodynamic design, system design and control system for a model-scale foiling boat
Joint project with SSRS & SSPA
NILS LUNDQVIST
ELIAS L. FAVRUM
Department of Mechanics & Maritime Sciences
Division of Marine Technology
Chalmers University of Technology

Abstract

Hydrofoils can help improve the efficiency of naval vehicles but not so many manufacturers are in the hydrofoil boat market yet. This work focuses on designing and manufacturing a system that allows hydrofoil positioning to be variable in three dimensions on a model-scale boat. The designed front wings and struts are analyzed through CFD simulations and compared to experimental tests performed at SSPA's facilities. Finally, an active control system is installed on the model. It is operated via the firmware Ardupilot. This project is intended as a development project and as a platform for obtaining knowledge towards the installation of hydrofoils on full-scale rescue boats in SSRS's fleet. This thesis is the first design iteration of many thus improvements are to be done to the model-scale foiling boat.

Keywords: Hydrofoil, experimental testing, numerical analysis, CFD, active control system, RC boat, Ardupilot, system design, 3D printing.

Acknowledgements

We would like to express our sincerest appreciation for the guidance and good discussions we have had with our Chalmers supervisor Arash Eslamdoost and SSPA project manager Alex Shiri. All inputs have been valuable and constructive during every step of the project.

A special thanks to Magnus Wikander from SSPA for always constructive feedback and help with some testing at SSPA's facilities.

We are grateful for the assistance all the technicians at SSPA were able to give during the tests. A special thanks to Christoffer Whitworth who volunteered to assist us for several hours to conduct some tests.

Special thanks go to the workshop employees in the prototype laboratory at Chalmers University of Technology and especially Jan Bragge who helped us produce all of the parts in steel. Without the expertise, the manufacturing of the parts for this project would not have been possible.

Special thanks go to Fredrik Falkman from SSRS who provided us with some electrical RC components and general guidance within the RC community.

Special thanks go to Adam Persson from SSPA who helped set up CFD simulations and gave some guidance with PID controllers in STAR CCM+.

Thanks to Håvard Holm from the Norwegian University of Science and Technology (NTNU) for participating as an additional supervisor.

Nils Lunqvist and Elias Favrum, Gothenburg, June 2022

Acronyms

AMR	Adaptive Mesh Refinement
AoA	Angle of Attack
AR	Aspect Ratio
CAD	Computer Aided Design
CFD	Computational Fluid Dynamics
CoG	Center of Gravity
EFD	Experimental Fluid Dynamics
ESC	Electronic Speed Control
GCS	Ground Control Station
GPIO	General Purpose Input/Output
GPS	Global Positioning System
IMU	Internal Measurement Unit
LiPo	Lithium Polymer
MIMO	Multiple Input Multiple Output
MP	Mission Planner
PETG	Polyethylene Terephthalate Glycol
PID	Propotional, Integral and Derivative
RC	Radio Control
SISO	Single Input Single Output
SSPA	SSPA Sweden AB
SSRS	Swedish Sea Rescue Society
VOF	Volume of Fluid

Nomenclature

A_p	Projected area
b	Span length
c	Chord length
C_D	Drag coefficient
C_F	Skin friction coefficient
C_L	Lift coefficient
C_P	Pressure coefficient
d	Depth
D	Drag
e	Error
F_r	Froude number
g	Gravitational acceleration
K_d	Derivative term
K_i	Integral term
K_p	Proportional term
L	Lift
μ	Heading angle relative to wave direction
μ	Dynamic viscosity
ν	Fluid viscosity
ω	Wave pulsation
ω_e	Measured pulsation of encountered waves
Ω	Vorticity tensor
P	Static pressure
P_∞	Static pressure in the free stream
Q	Q-criterion
ρ	Fluid density
R	Resistance
R_e	Reynolds number
S	Strain rate tensor
t	Time
τ_w	Skin shear stress
T_d	Derivative time term

T_i	Integral time term
u	Rate of change
U	Foil velocity for wave period determination
V	Velocity

Contents

List of Figures

List of Tables

1
Introduction

This project is carried out in collaboration with the Swedish Sea Rescue Society (SSRS) and SSPA Sweden AB (SSPA). The objective of the project is to develop a model-scale foiling boat platform. The elements of the platform need to be changeable thus requiring some system design that facilitates this need is important. This chapter introduces the background of the hydro-foiling concept and the scope of the project.

1.1 Background

Hydro-foiling is not a new concept. In the early twentieth century, Alexander Graham Bell was among the first to build a hydrofoil boat. From that point on, hydrofoil boats have been built in various sizes. The famous U.S navy vessel "Pegasus" was a great example of the concept working for extremely large-sized vessels. In the modern era, hydrofoils are seen on smaller boats such as "Candela" and "SEAir" or even surfboards. These boats can reach speeds around 30-40 knots when foilborne, giving the passengers smooth and comfortable rides without feeling the motion of the waves.

Not many different manufacturers are on the market yet for hydrofoil boats. This can be due to several factors such as safety in case of failure or production of the parts. SSRS is keen to get hydrofoil boats in their fleet as their rescue boats will be able to go as fast as they do already but at a much lower effort. The boats will then be able to be adapted with electric propulsion instead of traditional diesel engines which will secure their contribution to a greener future.

1.2 Purpose

The objective of this project is to develop and produce a model-scale foiling boat platform. Different constellations of sizes and locations of foils will yield many different solutions. It is therefore very important that the parts are easy to replace to test different setups. The results of the model-scale boat are not directly scalable for full-scale but can give an estimation of what will work for a full-scale boat. The expenses of producing the foils at full scale are very costly, thus model-scale tests are necessary.

This project can be divided into three subjects. First, is the hydro-dynamic aspect in terms of analyzing the foils and the behavior they yield. Second, the design of the system to change the parts. Third, is the control system of the foils. Programming a control system for a hydrofoil boat is not an easy task and can be a different project by itself with the help of control engineers. For the scope of this project, the help of Ardupilot[1] will be used to achieve some control of the system.

1.3 Limitations

All major projects can be associated with the project management triangle defining the relation between the scope, the cost, and the time for the project as shown in Figure 1.1. This project is no different. As mentioned, this project can be broken into three subjects, all being very time-consuming.

Figure 1.1: Project management triangle

Time is a constraint for this project since only five months are available. Starting from scratch designing a system and manufacturing everything consumes many hours. For this project, only the components that need structural integrity are either bought off the shelves or have been manufactured in the prototype laboratory at Chalmers University of Technology. For weight purposes, many pieces have also been 3D printed. The cost of 3D printing is low but time-consuming.

Early in the project, an application to the Rolf Sörmans fund was sent. This fund supports projects associated with the Naval Architecture and Ocean Engineering master's program. This project was awarded 65.000 SEK to carry out tests at SSPA. The money has been helpful to obtain results from the testing as well as for the procurement of manufacturing materials.

Given the time frame, the budget, and the ambition of the project it is hard to produce a fully finished model, but it is possible to come a long way and give the best possible circumstances for the next set of students willing to continue the development of the model foiling boat.

[1] https://ardupilot.org/

2
Theory

To develop a testing platform for the boat, it is necessary to understand a few theories. The behavior of the foils is of great importance when put into different conditions. Understanding this behavior will lead to knowledge of the mechanisms needed to obtain a successful control system.

2.1 Foil theory

Foils are used in many different applications such as turbines, air-crafts, motor-sports, etc. The use of hydrofoils is applicable to generate enough lift for maritime vessels. This lift will result in the vessel becoming foilborne and thereby operating out of the water. This mode of operation requires a substantially less amount of power since the resistance of the vessel is much lower than in hullborne operation. The concept of hydrofoiling can be related directly to aircraft theory. The flow across the foil can be described through two principles.

Bernoulli's principle states that the increment of speed in a fluid occurs simultaneously with the decrease of pressure for the same fluid. Figure 2.1 shows a general foil geometry. As the fluid is moving across the foil, the fluid on the top side of the foil will naturally gain speed due to the displacement from the geometry and thereby have lower pressure on the same side of the foil. On the lower side of the foil, this will be inverted compared to the upper side. Bernoulli's principle has some limitations and cannot explain lift on its own as it does not answer how lift is created.

Newton's third law states that an acting force creates a reacting force. As the fluid is moving across the foil, the force acting on the pressure side will create an up-going reacting force normal to the fluid direction. This is known as lift. For some foils, the angle of attack (AoA) will result in a higher lift coefficient hence more lift.

2.1.1 Foil geometry

Foils come in many different shapes which are carefully selected in order to obtain certain properties. Figure 2.1 shows the main particulars of an asymmetrical foil profile. Asymmetrical profiles will generate lift even at 0^o AoA which on the contrary symmetrical foil profiles do not. Asymmetrical profiles are therefore used on applications where lift is desired at 0^o AoA and negative AoA operation might not be used as much. For foiling, it is a desire to control the lift or the downforce on the

wings, thus symmetrical or close to symmetrical wings will yield in a wider range of operating angle hence more control than asymmetrical. Symmetrical profiles usually have smaller lift coefficients which is therefore a design compromise.

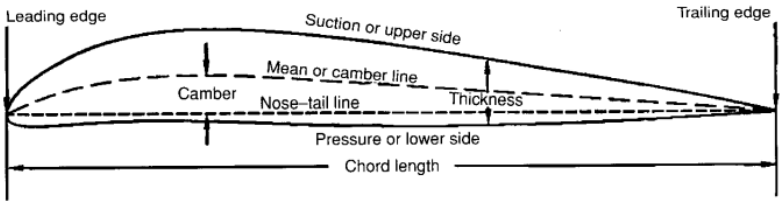

Figure 2.1: Foil geometry (Faltinsen, 2005)

2.1.2 Lift and drag

Lift and drag are the two central properties when working with foils. The geometry of the foil is carefully designed in order to obtain lift with a small amount of drag. No foil will have zero drag. Foil designs are useful for different applications. Different properties of lift and drag can therefore be desirable in various circumstances. It is often a good parameter to analyze the lift/drag ratio since it describes the efficiency of the foil. Lift is defined as:

$$L = \frac{1}{2} \cdot \rho \cdot V^2 \cdot C_L \cdot A_p \tag{2.1}$$

Drag is defined as:

$$D = \frac{1}{2} \cdot \rho \cdot V^2 \cdot C_D \cdot A_p \tag{2.2}$$

Where the projected area $A_p = b \cdot c$ for rectangular wings.
Figure 2.2 shows the direction of the lift and drag components for a general foil geometry. The drag is directed in the fluid direction. The lift is generated in the direction normal to the fluid. The amount of lift and drag will vary with the AoA. Linear foil theory can be assumed at small AoA ($< 10^o$).

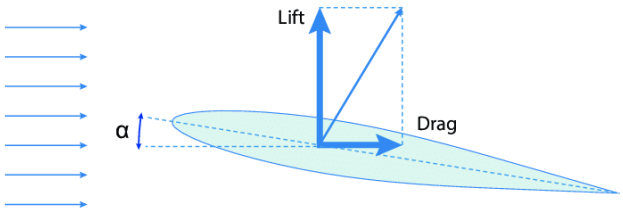

Figure 2.2: Lift and drag directions for general foil geometry (Ploé, 2018)

2.1.3 Aspect ratio

The aspect ratio (AR) is an important geometrical definition within foil theory. It describes the relationship between the wing span and the foil area. Faltinsen (2005)

describes the aspect ratio as:

$$\text{Aspect ratio} = \frac{\text{span}^2}{\text{projected foil area}}$$

Which can be derived for rectangular wing shapes as:

$$\text{Aspect ratio} = \frac{b^2}{b \cdot c} = \frac{b}{c} \tag{2.3}$$

Faltinsen (2005) presents aspect ratios in the range of $4 - 10$ for different vessels. Low aspect ratio foils will be subject to higher loading, as the required amount of lift will be generated from a smaller area. Furthermore, the induced drag depends on the aspect ratio. White (2011) demonstrates how higher aspect ratios result in more lift and lower drag but the stall angle occurs at smaller AoA.

2.1.4 Foil configuration

Johnston (1985) presents the different foil configurations as shown in Figure 2.3. The terms "conventional" and "canard" are derived from aircraft terminology. In these configurations, 65% or more of the total weight is supported by either the front or the rear wing. If the weight distribution is even between the rear and front wing, the configuration is called "tandem".

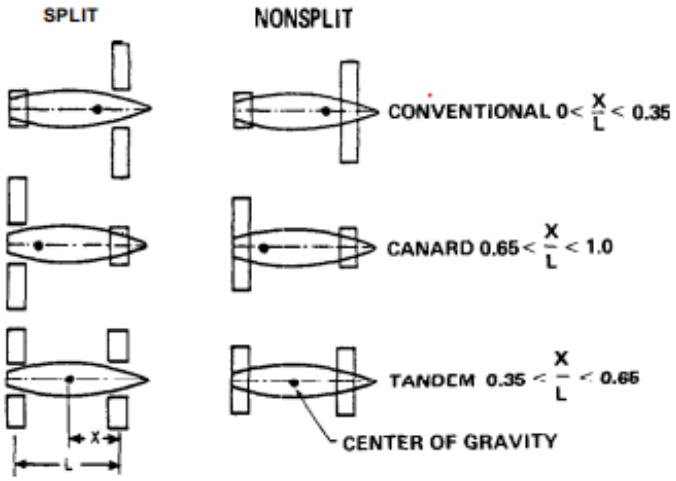

Figure 2.3: Hydrofoil configurations (Johnston, 1985)

Boat manufacturers rarely declare where the center of gravity is located on the boat thus it is difficult to use any empirical data to predict any optimal setup for the wings. On a small light model boat, the location of the main wings is of great importance to determine the longitudinal center of gravity since the weight of the wings is a great percentage of the whole weight of the boat.

2.2 Scaling laws

SSRS intends to build a full-scale hydrofoil boat, thus this project is intended as a model scale project. Different scaling laws are applicable to represent the full-scale

system as close as possible (Steen, 2014).

2.2.1 Froude similarity

Froude similarity is generally applied for scaling the velocity between full scale and model scale displacement vessels. It secures that there is a kinematic and geometric similarity between the model and full scale. Equality in Froude numbers will ensure similarity between inertia and gravity forces (Steen, 2014), which implies that wave resistance coefficients will be equal between the model and full scale.

$$F_r = \frac{V}{\sqrt{g \cdot c}} \tag{2.4}$$

Due to the low amount of water surface contact in foilborne condition, Froude similarity is not applicable in this project.

2.2.2 Reynolds similarity

Reynolds number describes the ratio between inertia and viscous forces. The similarity between model and full-scale Reynolds numbers will ensure correct viscous force scaling. The fully submerged hydrofoil system will at all times be subject to water flow across the geometry, thus Reynolds similarity is crucial in this project.

$$R_e = \frac{V \cdot c}{\nu} \tag{2.5}$$

Scaling of the velocity concerning Reynolds similarity yields at very high speeds for model scale. The Reynolds similarity is shown below and the model speed is isolated.

$$\begin{aligned} \frac{V_s \cdot c_s}{\nu} &= \frac{V_s \cdot c_s}{\nu} \\ V_s \cdot c_s &= V_m \cdot c_m \\ V_m &= V_s \cdot \frac{c_s}{c_m} \end{aligned} \tag{2.6}$$

It is evident that the scaling factor will be the deciding factor in this matter. Moonesun et al. (2014) showcases the problem for a submarine in fully submerged condition. The submarine is scaled at a ratio of 1:100 and a full-scale cruising speed of 10 m/s, the resulting model test speed is therefore 100 m/s. This is of course not obtainable at testing facilities. A way of manipulating the Reynolds similarity in this project is to change the chord length, hence manipulating the scaling factor. This creates a paradox where the geometrical scaling is not completely correct. Prolonging the foils will result in more lift which calls for more weight in the model.

2.3 Control theory

The control of hydrofoil vessels depends on the foil system. A passive control system consists of piercing surface foils that will correct for any undesired motion by itself.

Surface piercing foils will in large waves be fully submerged which will result in more lift, hence more upright heave motion. When the foil exits the wave, the system will now balance out hence a downward heave motion will occur. In bad conditions, the passive control system can therefore be unreliable and unpleasant to some extent.

The active control system is operated through fully submerged hydrofoils. For regular displacement vessels, roll motions from incoming waves are naturally countered by the up-righting moment. This is not true for foilborne hydrofoil vessels. The struts are impacted by incoming waves hence the vessel will roll. The active control system is controlled by accelerometers and gyroscopes to counter this roll motion. The signal will be sent to the foils which change the AoA to gain either lift or drag that satisfies the need to get to the correct upright position of the vessel. Figure 2.4 illustrates the six different degrees of freedom which need to be considered for an active control system.

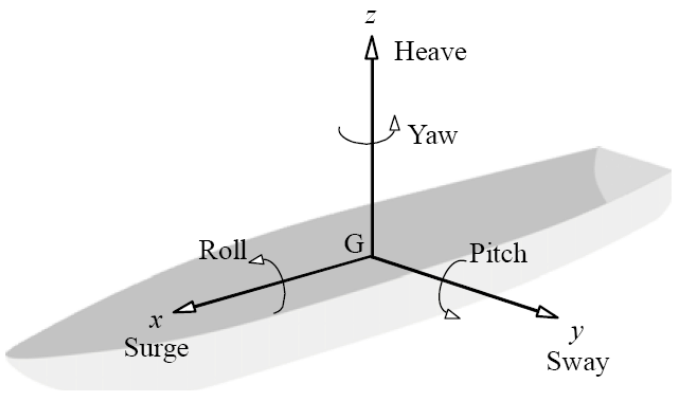

Figure 2.4: Six degrees of freedom for vessels (Tanaka, 2018)

Controlling all motions in six degrees of freedom with fully submerged hydrofoils is dependent on a feedback system. Such a system receives inputs from sensors, then sends the data to a controller which can use actuators to adapt to the circumstances. Feedback control of dynamic systems is a very old concept (Franklin et al., 2009). In a feedback system reliant on live data, there will always be disturbances from the outside of the system.

Figure 2.5 shows a generic simple feedback system. This system can directly be linked to how a hydrofoil boat can operate.

- Process: The angle of the hydrofoils that needs to be controlled.
- Disturbance: Interference on the wings affecting the output, e.g. waves.
- Sensor: Components that read live data, e.g. GPS, IMU and sonar sensors.
- Actuators: Components that uses the data received from the controller to make an adjustment to the wings, e.g. servo motors.
- Controller: Sends and receives signals from sensors to the actuators, e.g. an Ardupilot flight controller.
- Reference: The desired operating value for the output, e.g. ride height above the water surface.

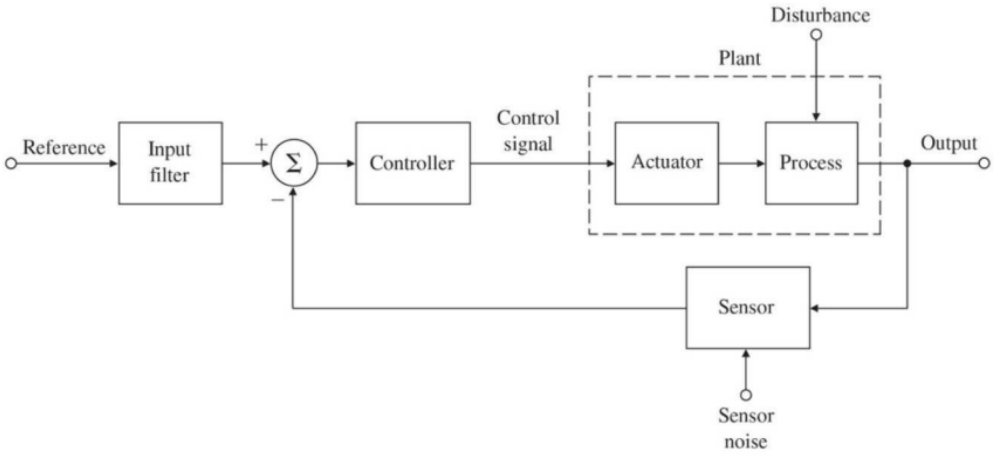

Figure 2.5: Simple feedback system (Franklin et al., 2009)

- Input filter: Component that converts input signals to energy.

For a fully personal control system, the firmware on the controller is using advanced algorithms. It is dependent on the complexity of the feedback loop. If the system only has one variable, it is called single-input single-output (SISO) control system. For multiple-input multiple-output (MIMO) control systems, the level of complexity is higher than for SISO systems since each variable requires a control feedback loop and the loops may interact with each other.

2.3.1 PID controller

PID control is a three-term control feedback loop. By evaluating the error present in the system relative to any desired action and constantly reporting back to the system, the PID controller uses the proportional term (P) when the feedback control signal is linearly proportional to the system error (Franklin et al., 2009). Integral feedback (I) occurs when the feedback control signal is linearly proportional to the integral of the system error. The integral term keeps track of all past errors by making a summation of all past errors, hence the integral over time. The derivative term (D) is called the rate feedback and is dependent on the variation rate of the error. This term helps improve system stability as well as speed up the transient response and reduce overshoot (Franklin et al., 2009). The mathematical formulation for PID controllers can be expressed as:

$$u(t) = K_p \cdot e(t) + K_i \int_0^t e(\tau) + K_d \frac{\mathrm{d}e(t)}{\mathrm{d}t} \tag{2.7}$$

Where:

- u is the rate of change of the controlled variable
- K_p , K_i and K_d are tuning coefficients
- e is the error defined as the difference between the target and the measured quantity

For this project, Ardupilot firmware is being used. Via the software Mission Planner, it is easy to change parameters in the system. Ardupilot uses PID controllers to adjust the motions by reading the current deviation from the desired position called error.

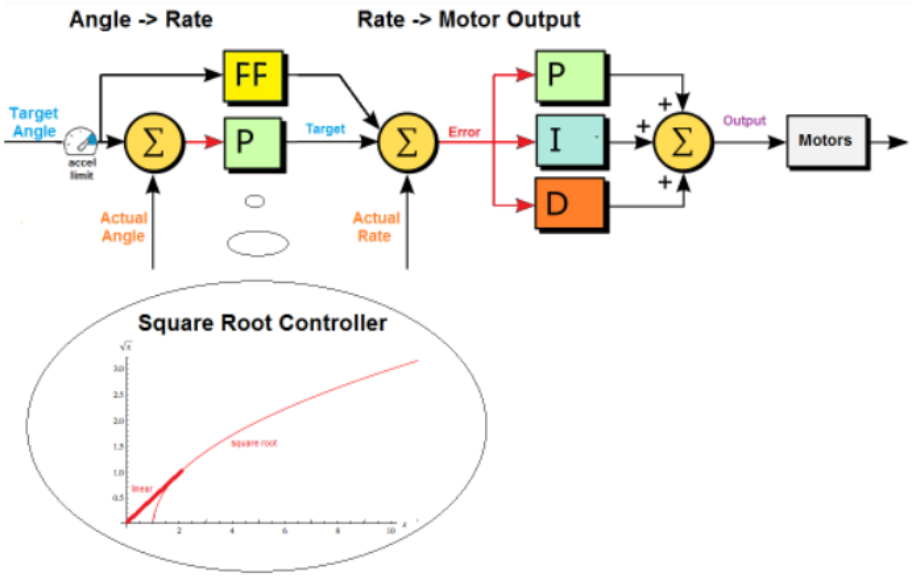

Figure 2.6: Ardupilot PID control system[1]

Figure 2.6 shows a schematic of the Ardupilot PID control system. On the left-hand side of the schematic, the system receives signals given by the user. The signals are processed and new target positions are called for through the proportional controller. The error is found which then calls for the three terms PID controller on the right-hand side.

2.3.2 Similarities to aircraft control

The control system for this project can very much be related to conventional aircraft control systems. These operate with flaps on the two main wings (called ailerons) for roll motion, one or multiple rear wings (called elevators) for pitch control, and a rudder for yaw control.

When a conventional airplane takes off, it will encounter a large pitch motion as a result of the location of the elevator wing. Some airplanes have experimented with the concept of elevons e.g. the famous Concorde. This is a type of wing which has the function of both ailerons and elevators. A plane with elevons on each side can therefore roll to either side if inverting the rotation of the elevons or changing its vertical position by rotating the elevons the same amount in synchronization.

For an active control system on a foiling boat, the elevon concept can be implemented as well. Because a rudder and propulsion system is needed on any boat, there is also

[1] https://ardupilot.org/dev/docs/apmcopter-programming-attitude-control-2.html

room for an elevator wing on the rudder. As a result, the foils on the main wings will control the roll and heave motion. The foils on the rear wing will control the pitch and heave motion. Yaw and surge motions are still controlled by the rudder and propulsion respectively. The sway motion is almost negligible for fully submerged foils since the wetted surface of the struts is small. The control system of the fully submerged hydrofoil system is recapped in Table 2.1.

Table 2.1: Means of control for six degrees of freedom for submerged hydrofoil system

Degree of freedom	Mean of control
Surge	Propulsion
Roll	Elevons
Sway	-
Pitch	Elevator and elevons
Heave	Elevator and elevons
Yaw	Rudder

3
Methods

The following method section describes the processes that lead to the making of the model and its features. First, a frame and foiling setup is designed on a structural and hydro-dynamical basis. Next, different electronic components need to be installed and calibrated. The final assembly can then be tested in an open field and compared to numerical analysis through CFD. The method for each of the steps in the development of the foiling boat will be explained in detail in this chapter.

3.1 System design

A general requirement for the model is to build the system in modules to be able to modify minor components with ease in the future. This is also resulting in the ability to change more variables in the system. The modularization is implemented for as many parts as possible. The system can be broken into different sections which are the following: the frame connecting the struts to the boat, the front struts holding the front wings, and the rudder holding the aft wing and propulsion system. All parts are drawn and assembled in AutoCAD. A list of all components can be found in Table D.1.

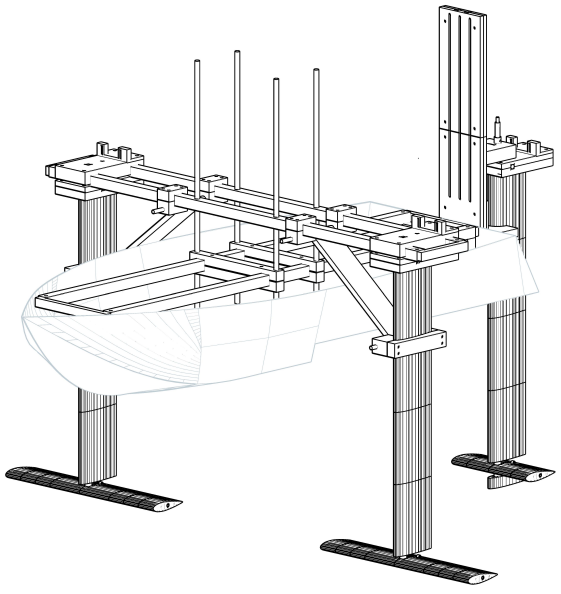

Figure 3.1: System design

Figure 3.1 shows the design and installation on a generically created hull. The figure shows the two main wings connected to individual struts connected to the frame system. In the aft part, the rudder is connected to a separate vertical rail system giving the possibility to elevate the rudder independently of the remaining system. The total weight of the system including the hull is 13.76 kg.

3.1.1 Frame system

The frame system is the foundation for connecting the hull to the struts. It is made of hollow 20x20 mm aluminum profiles with 1.5 mm wall thickness (ID: 1.1 and 1.2), resulting in enough strength to withstand the deflection caused by the lifting forces and offering a lightweight solution.

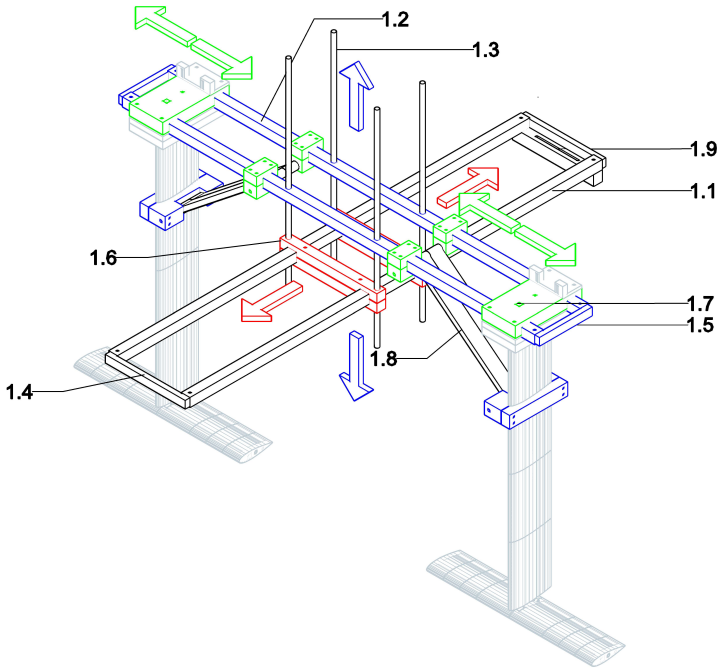

Figure 3.2: Frame system design

The frame system is designed in such a way that it acts as a three-dimensional positioning system for the front struts illustrated via the colors in Figure 3.2 where red-colored parts can move longitudinally, blue-colored parts can move vertically and green-colored parts can move transversely. All parts are locked into position with nuts and bolts.

The longitudinal fixation of the wing system (ID: 1.6) is connecting the longitudinal aluminum profiles (ID: 1.1) to the vertical bolts (ID: 1.3). The height of the transversal aluminum profiles (ID: 1.2) is controlled via the vertical bolts (ID: 1.3) and tightened nuts. To obtain more rigidness in the system, a girder system (ID: 1.8) is added. The position of the system (both on the aluminum profiles and the struts) can be changed to any testing setup desired. The end piece (ID: 1.4) is the

connection to the hull both in the bow and aft. A spacer (ID: 1.9) is required in the aft to keep the system level. The end pieces (ID: 1.5) on the transversal profiles are not mandatory but help keep the transversal profiles parallel to each other.

The positioning of the wings is defined by the three-dimensional system. The longitudinal variable is theoretically the entire length (1000 mm) of the longitudinal aluminum tubes but due to foil configurations, the main wings will never be located so far aft that the entire span will ever be used. The transversal aluminum tubes connecting the struts are also 1000 mm wide. Due to the beam of the hull, roughly 200 mm are variable to each side for transversal positioning of the wings. The vertical variable is 250 mm.

3.1.2 Wing geometry

One of the design goals is to have the AR of the front wings adjustable for the sake of stability and maneuvering studies. This feature is obtained by dividing the wings into several modules that are removable and thus the same geometry is conserved from one AR to another. This allows for consistency to study the influence of the AR on the control of the model.

An estimation of the lift coefficients needed for different speeds and different AR led to narrowing down the possible chord lengths and precise the characteristics of the profile required. The first design constraint is that it is necessary to make sure that the smallest AR provides enough lift for the desired take-off speed. To prevent stalling during the take-off phase, the operating AoA during take-off needs to be sufficiently small compared to the critical stall angle. Indeed, disturbances may require increasing the AoA above the operating angle for stabilization purposes. Another constraint is that the foils need to have a range of angles going at least from -10 to +10 degrees. This way the control system can take advantage of positive and negative lift as well as a wide range of angles to stabilize the boat.

On top of the constraints linked to the performances, practicalities have to be accounted for. For instance, the thickness of the wing needs to be large enough to fit the stiffeners and ensure a strong enough pivot link with the strut.

Based on the lift coefficient estimation and the geometry constraints, it was decided that the chord length would be 80 mm and the maximum thickness had to be 16 mm. Thus, the maximum thickness had to be 20% of the chord length. Table 3.1 shows the lift coefficient required for the wings in a speed range varying from $2 - 4$ m/s and a model weight of 13.5 kg.

Table 3.1 shows the required lift coefficient which varies between 0.26 (AR = 10, V = 4m/s) and 1.13 (AR = 6, V = 2.5m/s). Therefore, the wing profile GOE460 has been chosen as it fulfills the requirements. The characteristics of a GOE460 foil can be seen in Figure B.1. It can be noted that the lift stalls at 10^o with approximately $C_L = 1.1$. It should be noted that the characteristics of the foil vary

Table 3.1: Lift coefficient estimations dependent on AR and velocity

AR/V	2 m/s	2.5 m/s	4 m/s
6	1.72	1.13	0.43
8	1.30	0.83	0.32
10	1.03	0.66	0.26

with Reynolds numbers. The Reynolds number for the chord length of this project will vary between $160,000 - 320,000$. Deviations from the characteristics shown in Figure B.1 can therefore be expected.

Figure 3.3 shows the design of the GOE460 wing profile. As mentioned, several constraints and practicalities have to be worked into the geometry. Connecting modules side by side to increase the AR is taken care of with the help of the carbon fiber tubes. The tolerance of the holes is +0.2 mm when printing the modules for a tight fit. A bolt is also going through the modules and is then tightened on the wing end modules with nuts. The remaining compartments of the profile are voids. This help keep the weight to a minimum.

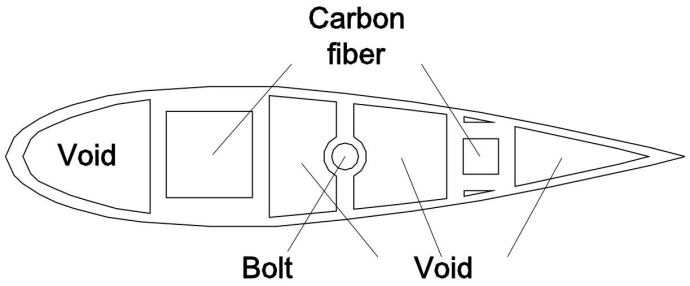

Figure 3.3: GOE460 wing profile design

3.1.3 Strut geometry

The focus when designing the struts is to keep the drag as low as possible and have a profile thick enough to fit stiffeners, the push rod, and ensure linkage between the strut and the wing and between the strut and the rails.

It was decided that the strut would have a symmetric profile with a chord length of 100 mm and a maximum thickness of 15 mm (15% of the chord length). In addition, the drag had to be minimized. Based on those constraints, the NACA0015 was selected and its characteristics are shown in Figure B.2.

The lift coefficient of the NACA0015 profile is of less importance compared to the GOE460 as the strut modules will not generate any lift. The drag coefficient is low at zero AoA, thus making the NACA0015 profile a great choice for the strut modules of the front wings. It is desired to have the same profile for the rudder as for

the front wing struts. Liu and Hekkenberg (2015) showcase what impact different NACA profiles have on maneuverability. The lift coefficient is slightly higher for the smaller thicknesses but slightly higher drag as well. For the ease of manufacturing in this project, the same NACA0015 profile is therefore used for the rudder as well. Figure 3.4 shows the design of the strut and rudder modules. The same concept is being used for having carbon fiber tubes connecting the modules. A tolerance of +0.2 mm is being used when printing the modules for a tight fit. Voids are added to keep the weight to a minimum.

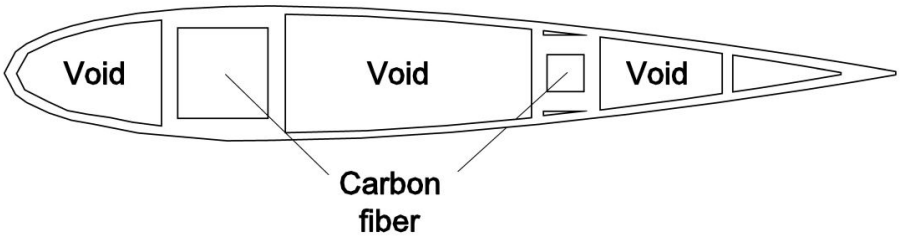

Figure 3.4: NACA0015 profile design

3.1.4 Front struts and wings - Assembly

The front wings are subject to forces in different circumstances. In general, when controlling the heave of the boat, the wings will rotate downwards. To control roll motions, the wings can rotate upwards if needed. Forces can therefore be unpredictable in certain scenarios. To simplify the force prediction, especially of the dynamic forces that can be difficult to estimate, a safety factor of 3 is used. Steel pieces (ID: 2.7 and 2.11) are made to withstand the forces produced by each wing. The forces are transferred into a vertical carbon fiber tube (ID: 2.10) and horizontal carbon fiber tubes (ID: 2.8 and 2.12). In this manner, no 3D printed components are subject to major forces e.g. the strut module (ID: 2.3) has no structural integrity and its sole purpose is to cover the carbon fiber tube and create a hydro-dynamically better flow around the strut.

The top strut component (ID: 2.2) is the counterpart to the strut fixation piece in the frame system (ID: 1.7 in Figure 3.2). To rotate the wings, a servo is installed with the servo fixation piece (ID: 2.1). The servo is controlling a pushrod made of steel down through the strut guided by a 4x4 mm with Ø2 extrusion carbon fiber tube (ID: 2.9). The pushrod is then connected to the center wing module (ID: 2.4). The AR of the wings can be adjusted by changing the number of wing modules (ID: 2.5). In Figure 3.5, two wing modules are added to each side of the strut. At the end of each wing is located a specific wing end module (ID: 2.6). This piece has a hole for a Ø3 bolt (ID: 2.14) on each end to tighten the wing modules together. For further stiffness and alignment of the modules, a 4x4 mm carbon fiber tube (ID: 2.13) is added inside the wing.

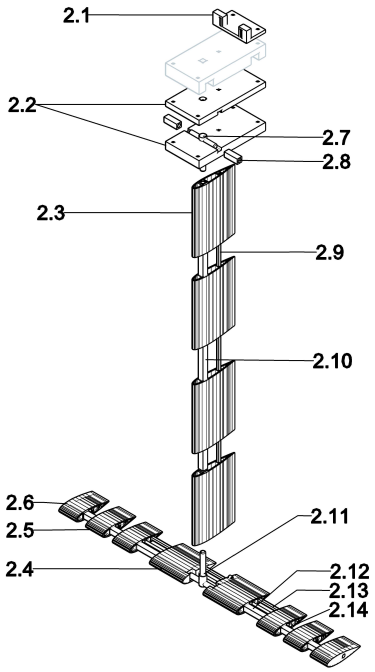

Figure 3.5: Front strut and wing

3.1.5 Rudder, rear wing and propulsion - Assembly

Most naval vehicles use a rudder to control the yaw movement. For a foiling boat, the rudder needs to be more submerged to still have any influence when in foilborne mode. In this project, the rudder is also acting like a strut for the rear wing. The installation of the propulsion can also be done in various ways. In this particular project, the rudder is also holding the propulsion. There are therefore many different components in the rudder design. Figure 3.6 shows the assembly of all the components.

The rudder is installed separately to the frame system from section 3.1.1. The reason for this is to be able to modify the height of the entire rudder piece, thus the vertical position of the rear wing and the propeller. The rail piece (ID: 3.1) consists of a clamp solution around two massive 8x8 mm carbon fiber profiles (ID: 3.10). The rudder is supported by a fixed piece (ID: 3.3) and is elevated by a shelf piece (ID: 3.2) that also holds the servo controlling the rudder.

From the design of the front wings, the same concept is used to transfer the forces via a steel cross joint (ID: 3.11) clamped around a top strut piece (ID: 3.4). The difference between this joint piece and the ones for the front wings is that in this scenario, it also acts as the center of rotation for the rudder. This means that the servo on the shelf piece (ID: 3.2) is connected via an arm to the cross joint (ID: 3.11). To lock the shelf piece vertically, an o-ring made of steel (ID: 3.13) is placed around the top part of the cross joint and locked via a bolt. A servo fixation piece (ID: 3.5) is added to the top part. This piece allows the installation of a servo to

control a pushrod attached to the wing.

As for the front wings, identical strut modules (ID: 3.6) are being used. Forces are transferred vertically through a 10x10 mm with Ø8 extrusion carbon fiber tube (ID: 3.14). A 4x4 mm with Ø2 extrusion carbon fiber tube (ID: 3.15) is guiding the pushrod through the strut modules.

In the wing region, a cross joint piece made of steel (ID: 3.16) is connecting the center wing modules (ID: 3.7) and the end wing modules (ID: 3.8) via carbon fiber tubes (ID: 3.18 and ID: 3.19). A Ø3 bolt (ID: 3.20) is clamping the wing together with nuts on each side of the end modules of the wing. The initial design concept is to install the propulsion on the very bottom of the entire structure on a small strut module (ID: 3.9). This feature will be explained in detail as the propulsion system is subject to design iterations.

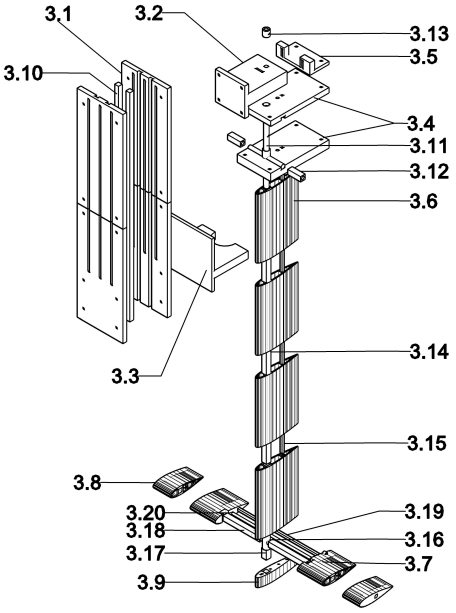

Figure 3.6: Rudder and rear wing

Propulsion

Early in the project, an estimation of the required power was done through Maxsurf. A generically generated rib was created with close dimensions to the actual model. Figure 3.7 shows the estimated resistance and power required for velocity as low as 10 knots.

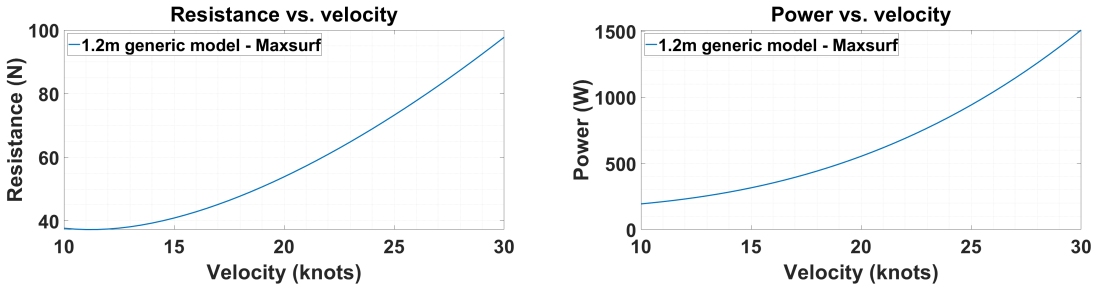

(a) Resistance estimation **(b)** Power estimation

Figure 3.7: Resistance and power estimation of a 1.2 m generic rib boat model in Maxsurf

The initial procurement of motors was therefore based on having enough power to obtain speeds of $4-5$ m/s. As a backup, twice the power amount was acquired. To test various setups for propulsion, the initial propulsion fixation (ID: 3.9) is subject to change as it is designed specifically for one RC thruster. Such a setup is shown in Figure 3.8(a). Alternatively, a dual setup was tested as shown in Figure 3.8(b).

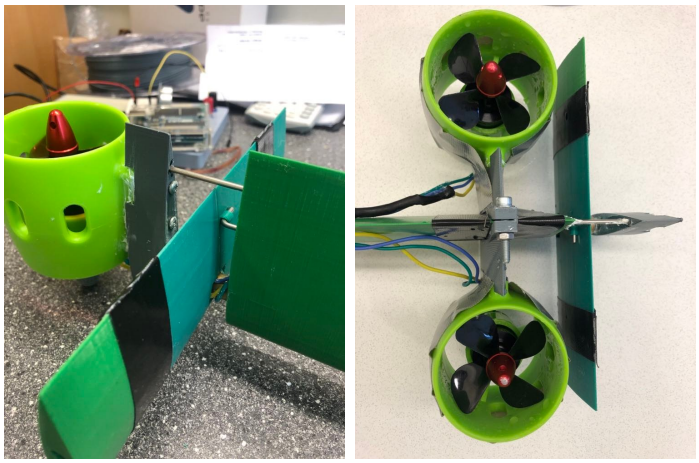

(a) Single setup **(b)** Dual setup

Figure 3.8: Different setups of thrusters

3.1.6 Materials and processes

For every single component, there is a weight to strength relation. For easier foiling, the boat needs to be as light as possible but the forces acting on the wings can result in fractures of crucial components if the material is not chosen wisely. As a result of this relation, the parts in the system are composed of PETG, steel, aluminum, or carbon fiber.

3D printing

PETG is a polycarbonate well suited for 3D printing. It is a widely chosen filament because of its mechanical properties making it a viable choice when printing stronger pieces. It also has some very good thermostatic properties making it easy to heat and mold to any desired shape.

In this project, PETG is used for any piece not subject to any major force. This means that any wing or strut modules are not carrying any load. Its sole purpose is to hide the carbon fiber tubes inside the modules and create a hydro-dynamically better flow. For the pieces ensuring connection to the frame system, PETG is a viable solution since the pieces can be printed as more solid objects with more infill than the foil pieces.

As a result of choosing PETG for many parts, the weight of the entire boat is kept to a minimum. This is resulting in a long production time as 3D printing is a slow process. The total amount of printing time is summed up to over 380 hours for the currently installed setup. Many parts have been iterated several times, thus many hours have been used iterating the pieces as well.

The tolerance of 3D printed parts is important. Prusa MK3 printers are being used for this project. The tolerance informed by the manufacturer of such a printer is 0.1 mm on the z-axis and 0.3 mm on the x- and y-axis. When fitting parts to 10x10mm or 8x8 mm carbon fiber tubes, holes have been printed in either 10.2x10.2 mm or 8.2x8.2 mm for a fit that allows the smallest deviation possible while still being able to add glue in the fittings. Holes of 0.1 mm less are still viable but are tight and make it difficult to add any glue to the fittings.

Prototype laboratory

For the t-joint pieces (ID: 2.7 and ID: 2.11) and the cross joint pieces (ID: 3.11 and ID: 3.16), steel is the chosen material. In this manner, the carrying ends have diameters of 8 mm meaning that they can fit inside the foil geometries. For this project, the prototype laboratory at Chalmers University of Technology has given an extensive amount of help preparing these steel pieces.

Procurement of off the shelf materials

The frame system is consisting of four 1000 mm long 20x20 mm profiles with 1.5 mm wall thickness aluminum tubes. This is a standardized measurement that can be bought in any hardware store. When lifting the boat out of the water at the maximum testing width, the deflection is estimated to be $<$ 1mm. The deflection can be reduced by installing thicker or in general larger aluminum tubes. This will have a massive effect on the weight of the system which will end up complicating foiling. It is therefore assumed that 1mm deflection is an acceptable compromise to

maintain it lightweight.

The struts, wings, rudder, and rudder rail are consisting of carbon fiber with different dimensions. A 4x4 mm with Ø2 extrusion tube is used for guiding the pushrod through the struts and the rudder. It is also used for holding the wing modules together and aligning them. 10x10 mm with Ø8 extrusion tubes are used to transfer the forces from the wings up through the struts and rudder via the steel joints. Massive 8x8 mm tubes are used for stiffening the rudder rail.

3.1.7 Electronics

The electric system used to control the boat is inspired by RC airplane setups since they have similar operation modes (see section 2.3 on control theory). The model is controlled through a transmitter that communicates with the system on board and is supported by the software Mission Planner. This software is introduced in section 3.1.8.

Table 3.2 shows a list of all electrical components used in the system. The components are divided into four groups according to their function.

Table 3.2: Electronic components list

Group	Item	Unit
Actuator	Servo	20 kgcm & waterproof
	Motor	100W-300 W RC thruster
Sensor	GPS	CUAV NEO V2
	Sonar	JSN-SR04T
Communication	Receiver	FS-iA6B
	Transmitter	Flysky FS-I6
	Flight controller	CUAV v5 nano
	Telemetry	3DXR 433 MHz
Power system	Battery	6S LiPo 22.2 V 4000 mAh
	ESC	50A brushless
	Power module	CUAV HV PM 60v 60 A

The centerpiece of the system is the flight controller. Its role is to process the data from the sensors and the communication system. To do so, the flight controller is equipped with the firmware ArduPlane[1] which then communicates to the actuators the appropriate response to control the behavior of the model.

The control of the model is divided between the inputs sent by the user and the commands sent by the flight controller resulting from the data processing. Depend-

[1] https://ardupilot.org/plane/

ing on the flight mode, the degree of control that the user has will vary. This way one can have the full manual control or on contrary have a pre-established path that will be followed automatically. Such flight modes of interest for the project are described in section 3.1.8. The communication channel between the user and the model is established through the receiver and the transmitter. Those signals are also communicated to the flight controller for the error correction and stabilization process.

To adapt to external perturbations, the system needs to sense its environment through the GPS and the sonar. The GPS informs about the position and the motions of the model such as speeds and accelerations in the three dimensions. IMUs in the flight controller also reads the motions of the model. On the other hand, the sonar measures the ride height and detects the water surface to anticipate incoming waves.

The steering of the control surfaces is realized by servos acting on the elevons, the elevator, and the rudder. The thrust is produced by an underwater electric motor placed on the rudder.

The onboard system is powered by a LiPo (Lithium Polymer) battery pack connected to the power module and the ESC. The ESC serves as a power regulator and buffers the current provided by the battery to the motor and the servos. Similarly, the power modules regulate the current supplied to the flight controller.

Wiring

The design of the flight controller makes the wiring relatively easy. The component is divided into two regions. A rail at the top of the flight controller is intended for the connection of actuators (motor/ESC, servos), the sonar, and the receiver. The rest is intended for the connection of the GPS and the telemetry antenna. It should be noted that those two regions are powered through independent cables. The battery supplies power to the power module and is then redistributed through two different channels. The rail is powered through the ESC that is connected to the power module and the rest is powered by a cable directly connected from the power module to the flight controller. Without a direct power supply to the rail, the servos will not work.

The rail is composed of two different types of outlets. On the CUAV V5 nano, there are 8 main outlets and 4 auxiliary ones. The receiver is connected to another specific outlet on the rail destined for this purpose. The sonar is composed of two signal channels: one for the trigger (sound-emitting part of the sonar) and one for the echo (sound receiving part). Therefore, the sonar requires two auxiliary connectors, one for each communication channel. It should also be mentioned that the auxiliary channels have to be converted to GPIO (General Purpose Input/Output) in Mission Planner to ensure signal communication. The components are plugged

in the arrangement shown in Table 3.3.

Table 3.3: Flight controller output board list

RC	Receiver
M1	Motor 1
M2	Servo Elevator
M3	Motor 2
M4	Servo Rudder
M5	Servo Elevon Left
M6	Servo Elevon Right
M7	Power supply from extra ESC
A1	Trigger sonar
A2	Echo sonar

The wiring diagram in Figure 3.9 shows the connection between all the electrical components. It should be noted that connections and soldering of the wires can be done much smoother with more expertise.

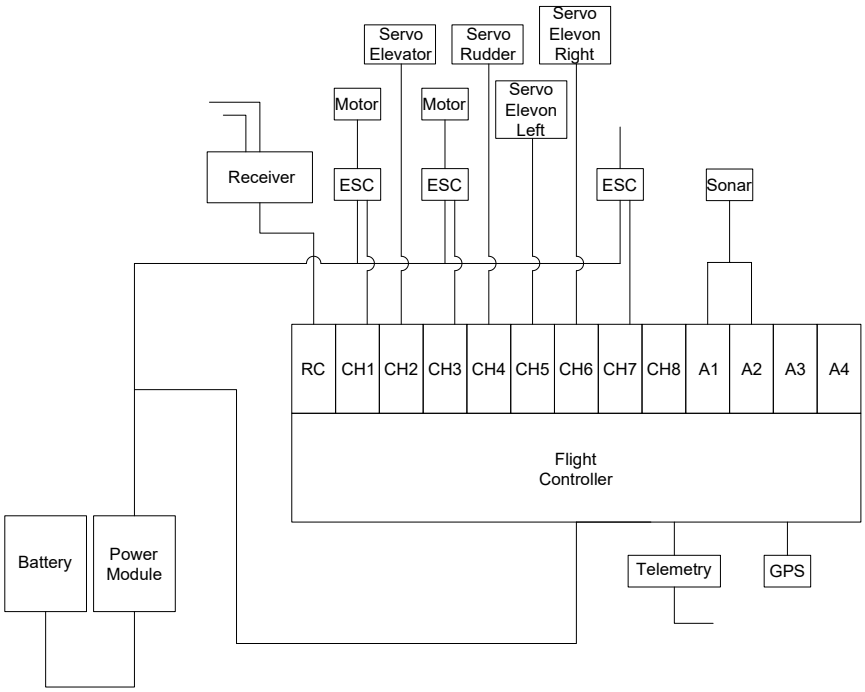

Figure 3.9: Wire diagram

Transmitter Channels

The transmitter used for this project (FlySky FS-I6[2]) is composed of two joysticks that control the motions of the model. A 3-position switch on the transmitter is used to change flight modes during operation. Following a common setup among the RC community members, each channel controls a different motion as displayed in Table 3.4 and Figure 3.10.

Table 3.4: Transmitter channels

CH1	Roll
CH2	Pitch
CH3	Throttle
CH4	Yaw
CH5/Switch	Flight modes

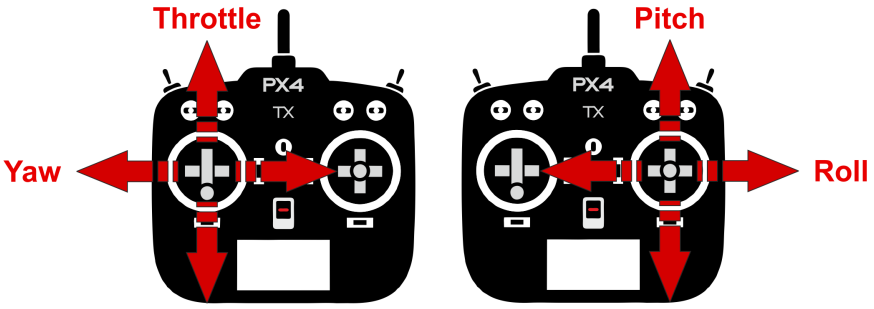

Figure 3.10: Motion controls on transmitter[3]

When switching flight modes, some motions are not controllable anymore and consequently the corresponding channels can be assigned another motion. It is for instance the case when switching to the cruise flight mode. Roll and pitch are then not controllable and thus both Channel 1 and 4 can be used to control the yaw motion.

3.1.8 Ground control station (GCS) - Mission Planner

Mission Planner[4] is an open-source ground control station software for numerous types of vehicles. It allows the user to load firmware on flight controllers, tune

[2]https://www.flysky-cn.com/i6-gaishu
[3]https://docs.px4.io/master/en/getting_started/rc_transmitter_receiver.html
[4]https://ardupilot.org/planner/docs/mission-planner-installation.html

and configure the system, and load and analyze the data acquired during the vehicle's mission. It serves as an interface between the flight controller and the user to monitor and set up the vehicle through a telemetry antenna (or a USB cable). The software is also used for arming/disarming vehicles as a safety mechanism. No physical throttle can be obtained without arming first.

A firmware is a piece of code loaded on the flight controller that will dictate how the motions should be controlled to maintain stability and maneuverability. Through Mission Planner, it is possible to load different firmware designed for different types of vehicles. As mentioned earlier, the most adequate firmware for the foiling boat is the ArduPlane firmware due to the close operation modes (see section 2.3.2 on aircraft control). To ensure reliability and stability over the control, the firmware relies on PID control systems (see section 2.3.1). The parameters of such PID system can be tuned in Mission Planner, along with other variables to refine the stability, to ensure better performances and a better flight experience. The parameters modified in this project are listed in Table E.1. Many more parameters can be modified inside Mission Planner.

Different levels of control can be selected during flight by changing the flight modes. Depending on the situation, the user might want to have full manual control over the vehicle or leave some freedom to the flight controller in exchange for more stability. In the present project, two main flight modes are of interest: manual and stabilize. ArduPlane has many more flight modes, each with different settings hence it is possible to obtain self-stabilizing effects from several different flight modes.

- Manual flight mode: The manual mode leaves full control of the model to the user. The stabilization system is turned off and all motions are dependent on the user's inputs.

- Stabilize flight mode: This mode controls the pitch and roll motions of the vehicle. The user will still have control of the throttle and yaw and it is therefore suited for simple maneuvering operations.

As mentioned in section 2.3.1, the firmware participating in the stabilization process uses a PID control system. The system processes the data read by the sensors (GPS and sonar) to calculate the adequate response that will be communicated to the actuators through an electric signal.

The data acquired during the flights can be reviewed and analyzed in Mission Planner's interface. When connecting the flight controller to Mission Planner, a file containing all the measured quantities is created. This file is then fed with the information accumulated by the flight controller and communicated to the computer via the telemetry antennas. A feature in Mission Planner can then graph the data or convert it for other uses.

3.2 Numerical analysis using CFD

In parallel to the manufacturing and experiments, some CFD studies have been carried out. The first study focuses on observing the influence of the water surface proximity on the performance of the wings. The second study aims to implement a PID controller on the lift and use the results to tune the active control system. Finally, a CFD study was realized to compare simulations and results from experiments done at SSPA's towing tank.

Each study shares a common base when it comes to models used and mesh conditions. The common points are explained in the following paragraphs and the variations specific to each study are detailed in the corresponding sections.

Models

The different models used for the simulation are listed below:

- SST K-Omega: The SST k-omega model combines two models adapted for different regions of the flow. On one hand, the k-omega model is adapted to simulate the flow near the wall. On the other hand, the k-epsilon model is well suited to simulate flows away from the wall.

- All-y+ treatment: Two approaches are usually used to model the boundary layer. With the high-y+ treatment, wall boundary functions are used. With the low-y+ treatment, a fine mesh close to the wall is required to solve the boundary layer. The all-y+ treatment is a model combining both approaches.

- Implicit unsteady: This model is used when the phenomena studied are time-dependent as is the case in the following studies since the flow is turbulent and the water surface is disturbed. Through this model, the time step can be selected.

- Eulerian multiphase mixture: This set of models is implemented to simulate the presence of the water surface and more generally when there are several immiscible phases in the flow. A mixture of the phases occurs when the air penetrates the water when there are waves for instance.

- VOF waves: The Volume Of Fluid wave model is used to simulate the behavior of gravity waves at the interface between immiscible light and heavy fluids such as in this case air and water.

To compensate for possible backflow due to waves encountering the boundaries that could cause divergence of the solution, the damping of the waves had to be set up. Thus, waves are dampened when they are less than 0.25 m away from the outlet and the side velocity inlet boundary.

Mesh conditions

Meshes from one study to another share common meshing methods such as:

- Prism layer mesher: this meshing method creates layers of prismatic cells close to boundaries where the model is active. This allows to locally improve the mesh to obtain a more accurate flow solution. The growth, size, and number of layers can be adjusted.

- Surface remesher: this model improves the mesh of geometries present in the simulation where the model is active and that requires a fine meshing of the curvature and complex regions.

- Trimmer: This model principally uses hexahedral mesh to refine and improve alignment to obtain a surface result.

- AMR (Adaptive mesh refinement): The AMR model is a way to dynamically modify the mesh (refining/coarsening) to adapt to the solution. It is in particular adapted to moving regions of the mesh such as the water surface, and the wake behind objects or bodies in motion. This method was used to mesh the water surface in the following simulations. Another case of such a dynamic meshing method (the overset mesh) is used for the PID controller simulation and detailed in section 3.2.2.

The prism layer mesher is disabled on the boundaries to reduce the number of cells.

Local refinements of the mesh in certain regions are implemented to better capture highly dynamic flows. It is, in particular, the case for the wingtips, the wake behind the foils, the water level, and the region near the foil. The PID setup was done in a quasi 2D domain and therefore needed only refinement around the foil and the water level (see section 3.2.2).

3.2.1 Surface interaction study

The study aims to determine how are drag and lift influenced by the proximity of the foils to the free surface. Thus an optimal depth range can be estimated and will contribute to the tuning of the active control system. In addition to that, a symmetry boundary is implemented to include the two wings and observe potential interactions. The closest tip of the wing is situated 110 mm from the symmetry boundary, so virtually the two wings are 220 mm away from each other. This distance was chosen based on the size of the hull. It is the closest the wings can be when mounted on the boat and where the most interactions could occur.

The study consists of a series of simulations of varying depths and angles of attack to observe the behavior in several operating conditions. Thus the following depths and angles have been computed: [0.5c, 1c, 1.5c, 4c] and [-8, 4, 8] deg. For each

simulation, the relative speeds of air and water were set to 4 m/s as this is the target cruising speed.

Mesh and domain

The geometry used for this study was an AS5046 wing profile with a chord length of 60 mm selected during an early stage of the project. The total main wing had an AR of 6 (total span of 360 mm) and was thus divided into two 180 mm wings. As mentioned previously, one wing was modeled with a symmetry boundary was set up to include the second wing and save some computational effort.

The domain is 42c long in the flow direction, 17c wide, and 13c high, keeping reasonable distances to the boundaries so their influence wouldn't affect the simulation results. Refinements of the domain are set in highly dynamic and critical regions to better capture the flow behavior and improve results. Such regions are the free surface, the wingtips, the wing proximity, and the wake. This mesh configuration consists of about 10^6 cells.

Table 3.5: Domain size for surface interaction study

Axis	[m]	Chord length
X	2.5	42c
Y	1	17c
Z	0.8	13c

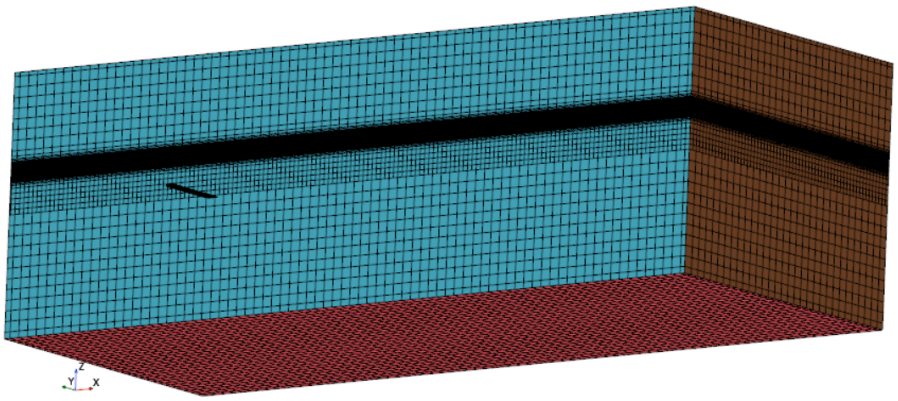

Figure 3.11: Mesh of the domain for the surface interaction study

The characteristics of the mesh used for those simulations are displayed in Table 3.6:

Table 3.6: Mesh properties for surface interaction study

Mesh values		
Regions	Parameters	Values / Properties
Mesh continua	Base size	0.04m
	Maximum cell size	100% of base size
Foil boundary	Number of prism layers	7
	Prism layer stretching	1.2
	Prism layer thickness	10% of base size
	Minimum relative surface size	0.1% of base size
	Target relative surface size	3.75% of base size
Other boundaries	Customize prism mesh	Disable
	Minimum relative surface size	100% of base size
	Target relative surface size	100% of base size
Volumetric controls		
Water level	Trimmer Anisotropic X size	15% of base size
	Trimmer Anisotropic Z size	5% of base size
Foil region	Relative size	5% of base size
Foil tips	Relative size	5% of base size
Wake	Relative size	10% of base size
Horizontal foil level	Relative size	37.5% of base size

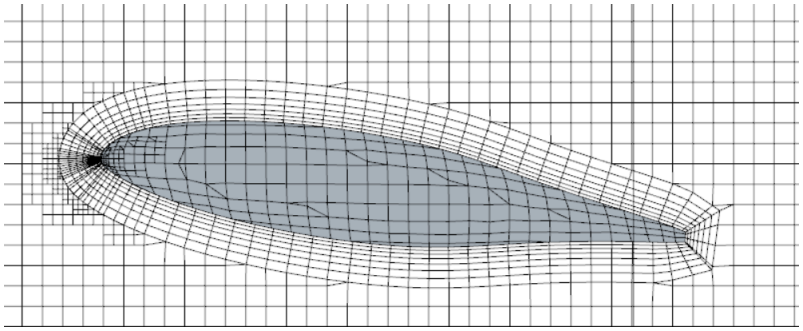

Figure 3.12: AS5046 wing mesh

Models

The models implemented for this study are detailed in section 3.2. The time-step in the implicit unsteady solver is set to 0.025 s and the number of inner iterations is 10.

Figure 3.13 shows how the setup looks like after implementing the water surface and the different mesh refinements.

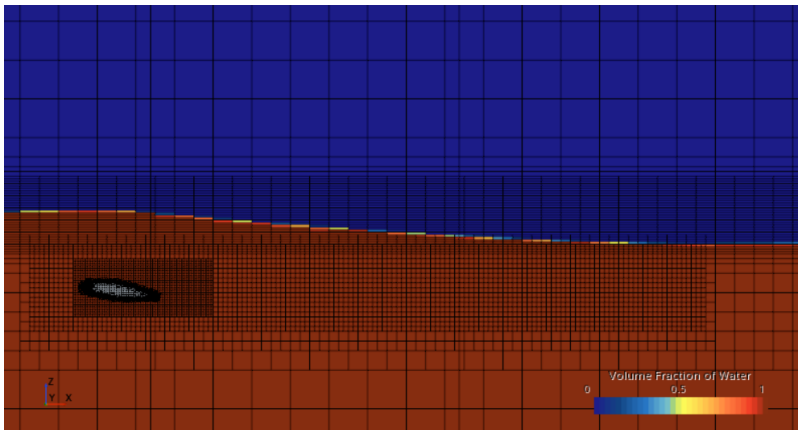

Figure 3.13: Water surface interaction study simulation setup

3.2.2 Simulation of a quasi 2D wing without strut and implementation of a PID controller

The motivation to carry out this study is to set up a procedure so that the results from the tuning of the PID controller in Star CCM+ could be transferred to the tuning of the firmware that stabilizes the model. Indeed, the Mission Planner's stabilization program makes use of PIDs that can be tuned in the software's interface.

In this study, the measured variable is the lift and the quantity varied is the AoA of the wing. By creating various reports and parameters in the simulation, the following equation can be evaluated at each time step to calculate the rotation rate of the wing necessary to attain the target lift:

$$u(t) = K_p \cdot (e(t) + \frac{1}{T_i}\int_0^t e(\tau) + T_d\frac{\mathrm{d}e(t)}{\mathrm{d}t}) \tag{3.1}$$

where:

- u is the rate of change of the AoA
- K_p, T_i , T_d are tuning parameters of the PID controller
- e is the error defined as $e(t)$ = target Lift - measured Lift

This equation is a reformulation of the more general Eq. 2.7 explained in section 2.3.1 on PID theory.

Mesh and domain

Having moving parts in a simulation requires a constant adaptation of the mesh which is time-consuming. Consequently, the number of cells is to be decreased as much as possible but the generation of waves is not possible with a 2D mesh. Hence the quasi 2D domain used is two cells wide and composed of around 300,000 cells. The dimensions of the domain are gathered in Table 3.7.

Table 3.7: Domain size for the PID simulation

Axis	[m]	Chord length
X	3.5	44c
Y	0.004	0.05c
Z	0.8	10c

The mesh is obtained by applying the following mesh conditions:

Table 3.8: Mesh values for the PID simulation

Mesh values		
Regions	Parameters	Values / Properties
Mesh continua	Base size	0.04m
	Maximum cell size	100% of base size
Background region		
Foil boundary	Number of prism layers	7
	Prism layer stretching	1.2
	Prism layer thickness	10% of base size
	Minimum relative surface size	0.1% of base size
	Target relative surface size	3.75% of base size
Other boundaries	Customize prism mesh	Disable
	Minimum relative surface size	100% of base size
	Target relative surface size	100% of base size
Overset region		
Foil boundary	Number of prism layers	7
	Prism layer stretching	1.2
	Prism layer thickness	3
Symmetry boundary	Customize prism mesh	Disable
	Minimum relative surface size	100% of base size
	Target relative surface size	100% of base size
West boundary	Customize prism mesh	Disable
	Minimum relative surface size	100% of base size
	Target relative surface size	100% of base size
Other boundaries	-	-
Volumetric controls		
Water level	Trimmer Anisotropic X size	15% of base size
	Trimmer Anisotropic X size	5% of base size
Foil region	Relative size	5% of base size
Wake	Relative size	10% of base size
Horizontal foil level	Relative size	37.5% of base size

Overset meshing method

The overset meshing method is used to reduce the computational effort required to simulate moving bodies. Instead of re-meshing the entire domain from one time-step to another, with the overset mesh technique, it is possible to select a smaller portion to re-mesh that includes the moving body. To do so, two regions are created: one for the background domain and another one attached to the object in motion. The superposition of the two regions is done by cutting a hole in the background domain and replacing it with the overset region. A group of transition cells is created around the body, finer than the background mesh, and will act as a bridge between the two regions to allow for finer data interpolation. It is particularly useful when setting up a PID controller for the simulation as the wing is constantly rotating to adjust for the target lift.

The overset mesh region is distinguished by its red color in Figure 3.14.

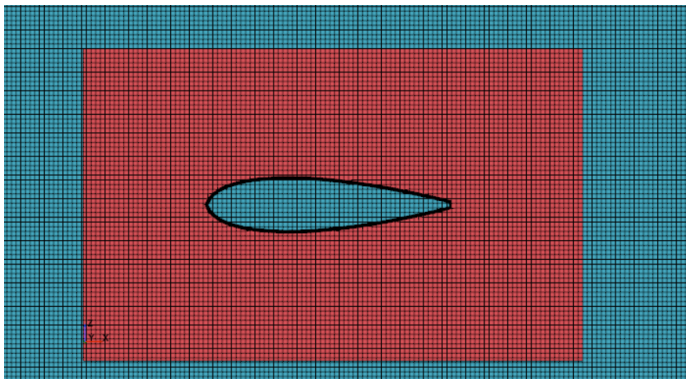

Figure 3.14: Overset mesh region

Volumetric control refinements

Refinements of the mesh are set up at the water level, around the overset mesh, and at the level of the wake of the foil as shown in Figure 3.15. This ensures a more stable simulation and interpolation between the two regions.

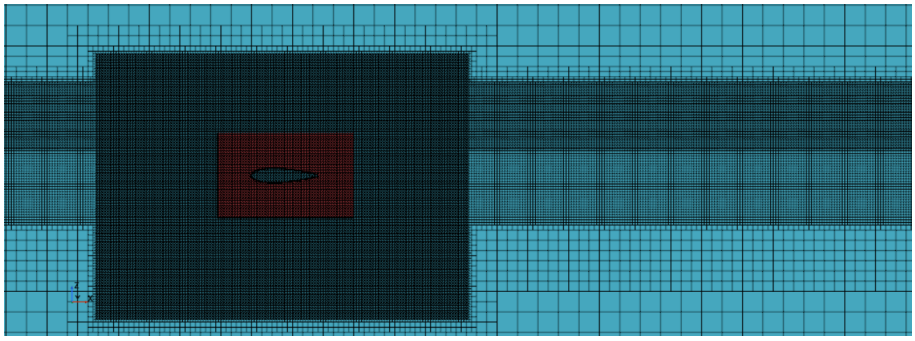

Figure 3.15: Volumetric control refinements of the computational domain

Models

The models implemented for this study are detailed in section 3.2. The time-step in the implicit unsteady solver is set to 0.025 s and the number of inner iterations is 10. The fifth-order VOF wave model is used to generate the waves.

Setup and Tuning of the PID

Setting up the PID in Star CCM+ requires a macro that can be found in Appendix G. The macro is necessary to update the various reports that represent the backbone of the PID setup.

The parameters K_p, T_i and T_d present in Eq. 3.1 need to be adapted accordingly to the system the PID is controlling. To do so, a step response test needs to be carried out. The test consists of changing abruptly the controlled variable, the AoA in this case, and recording the change in the measured variable, the lift. The behavior of the system to the step-change can then be analyzed to determine the adequate parameters. An online PID tuner[5] is used for this part.

3.2.3 Simulation of wing with strut in calm water

Part of the project consists of comparing CFD results to experiments carried out at SSPA (see section 3.3.3). The simulations ran on Star CCM+ follow the same test matrix as for the experiments except for angles. To reduce the number of simulations, the angles chosen are [2, 4, 6] deg. As for the previous study, the depth and the AoA have been changed. The geometry of the wings has also been updated with the final profile chosen: GOE 460.

Mesh and domain

To reduce the computational effort, the geometry is simpler than the actual wing. The holes present in the strut in the model and the push rod and its fixation are not modeled in the simulation. The mesh and the model wings can be observed in the picture below:

[5]https://pidtuner.com/#/

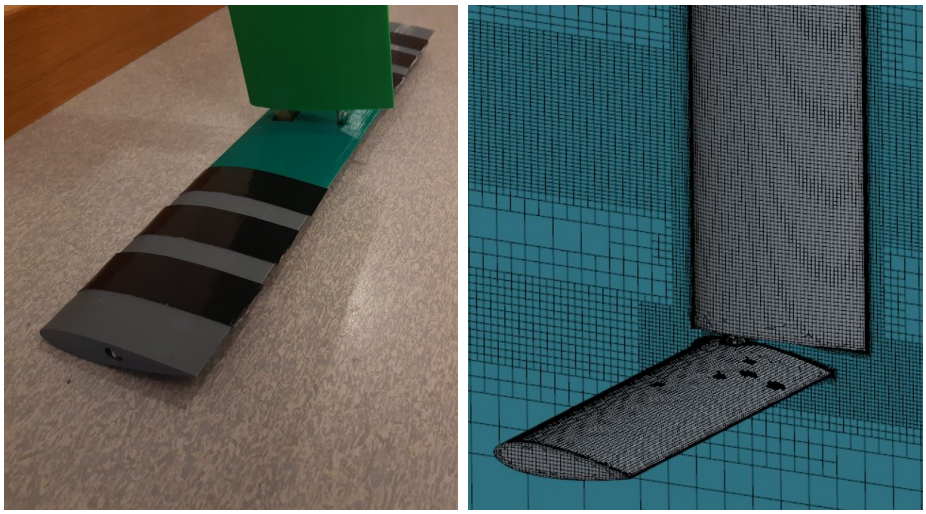

(a) Wing setup **(b)** Mesh of the wing

Figure 3.16: Comparison of the differences between model and mesh

Moreover, a symmetry boundary layer is implemented across the wing geometry in the XZ plane. The dimensions of the domain are displayed in Table 3.9 and the cell number varies between $2.2 \cdot 10^6 - 2.8 \cdot 10^6$ cells depending on the test case. Finally, the AMR method (see section 3.2 on AMR) is also activated to improve the mesh around the water level.

Table 3.9: Domain size for wing with strut comparison study

Axis	[m]	Chord length
X	3.5	44c
Y	0.9	11c
Z	0.8	10c

Figure 3.17 shows the domain size relative to the geometry implemented in the simulation:

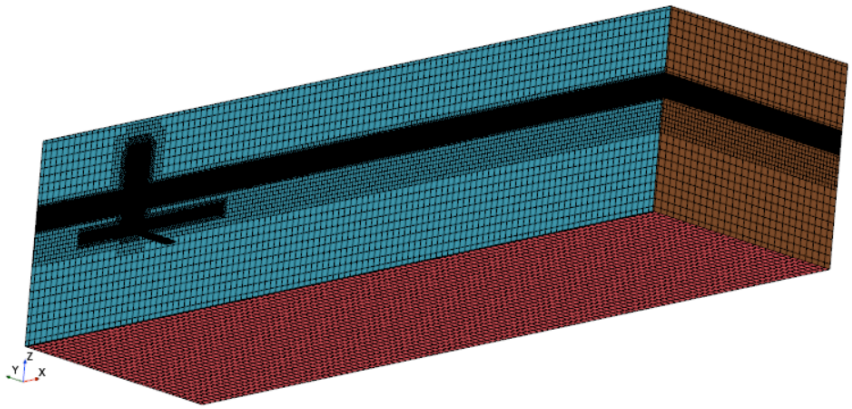

Figure 3.17: Domain of the comparison study

The different volumetric controls intended for local mesh refinement (mentioned in section 3.2) can be observed in Figure 3.18.

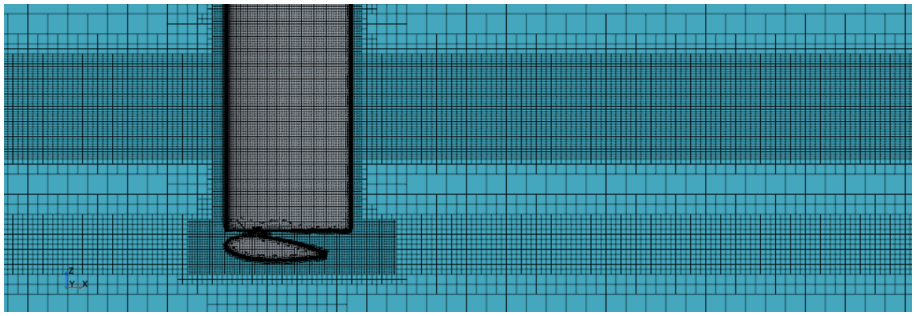

Figure 3.18: Mesh of the wing with strut

The mesh values of those simulations are very similar to those of the surface interaction study with the difference that the strut has now been added:

Table 3.10: Mesh properties for simulation of wing with strut

Mesh values		
Regions	Parameters	Values / Properties
Mesh continua	Base size	0.04m
	Maximum cell size	100% of base size
Foil boundary	Number of prism layers	7
	Prism layer stretching	1.2
	Prism layer thickness	10% of base size
	Minimum relative surface size	0.1% of base size
	Target relative surface size	3.75% of base size
Strut boundary	Number of prism layers	7
	Prism layer stretching	1.2
	Prism layer thickness	10% of base size
	Minimum relative surface size	1% of base size
	Target relative surface size	10% of base size
Other boundaries	Customize prism mesh	Disable
	Minimum relative surface size	100% of base size
	Target relative surface size	100% of base size
Volumetric controls		
Water level	Trimmer Anisotropic X size	15% of base size
	Trimmer Anisotropic X size	5% of base size
Foil region	Relative size	5% of base size
Foil tips	Relative size	5% of base size
Wake	Relative size	10% of base size
Horizontal foil level	Relative size	37.5% of base size

Models

The models implemented for this study are detailed in section 3.2. The time-step in the implicit unsteady solver is set to 0.001 s and the number of inner iterations is 1.

3.2.4 Simulation of wing with strut encountering waves

The setup for this part of the project is similar to the previous study in calm water. The difference is that waves are simulated with the same characteristics as for the towing test at SSPA using the fifth-order VOF wave model. The wave characteristics are shown in Table 3.11.

Table 3.11: Characteristics of simulated waves

Characteristic	Value
Wave length	1 m
Wave amplitude	0.025 m
Wave steepness	2.5%
Wave period	0.73 s
Wave velocity	1.37 m/s

The procedure to determine the wave period is explained in section 4.2.3.

3.3 Experimental tests

To learn all the hydro-dynamical aspects of the system, several tests have been taking place in SSPA's towing tank. The facility is a 260 m long tank with a carriage on top. Installations of any desired object can be done, making it a perfect way of learning the behavior of the different parts of this project. As the model can never be free running in SSPA's facilities, it is necessary to also do some field testing to see the maneuvering of the model as well as the response of the control system.

3.3.1 Bare hull with rudder towing tank test at SSPA

Learning the drag of the different components of the system is essential for optimization. Several towing tank tests were therefore performed. First, the bare hull is tested at velocities of $V = [2,\ 3,\ 4,\ 5]$ m/s. Next, the rudder is also attached to the hull. This setup was only tested at $V = 2$ m/s due to the moment created on the rudder as a result of towing the propulsion region of the setup. This region creates a large amount of drag when not rotating them. Since much of the rudder is manufactured from 3D printed parts, it is not certain that all the parts can withstand towing at high speeds without the use of the propellers.

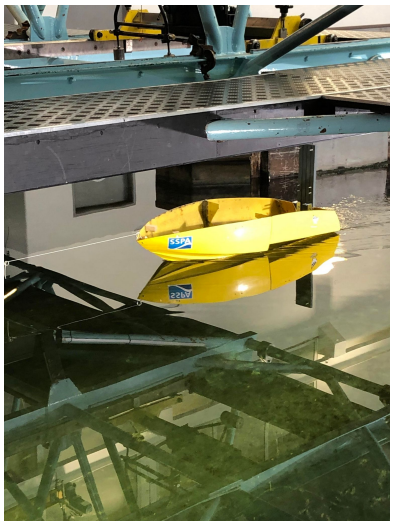

Figure 3.19: Towing tank test of bare hull at SSPA

3.3.2 Bollard pull test at SSPA

To test the thrusters and learn the exact thrust they deliver, a bollard pull test was set up at SSPA. From simple initial testing, it was evident that the single thruster setup as shown in Figure 3.8(a) was not sufficient. The bollard pull test was therefore done using the dual setup as shown in Figure 3.8(b). A string was attached between the rudder and the gauge as shown in Figure 3.20.

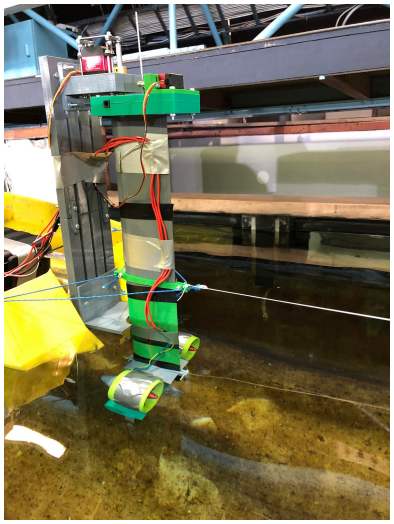

Figure 3.20: Bollard pull test at SSPA

3.3.3 Front wing towing tank test at SSPA

The study aims to measure the lift and drag produced by one wing for different angles of attack, depths, and speeds. A series of tests were carried out in calm water and two runs were done in waves.

Calm water tests

Table 3.12 shows the test case variables. The depth and the AoA are fixed for the duration of the run but the speed is varied to test the whole speed range during one run. At the end of the run, the wing is taken out of the water so that no damage occurs when resetting the position of the carriage. The depth is then changed with no change in AoA. In this manner, the same AoA is tested at different depths decreasing uncertainties.

Table 3.12: Test case variables for front wing towing tank test

Speeds	[2, 3, 4] m/s
Depths	[80, 120] mm
AoA	[0.3, 3, 6, 7.5, 9.5, 12]^o

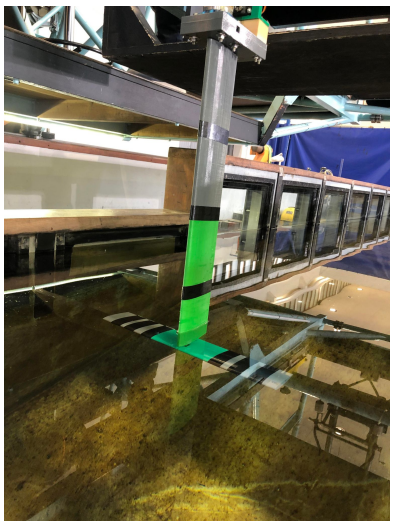

Figure 3.21: SSPA towing tank test setup of front wing with strut

Wave test

The test carried out in waves cover one single configuration consisting of a depth = 80 mm and AoA = 12^o at 3 m/s. This configuration was run twice.

The waves produced had an estimated wavelength of 1 m and amplitude of 25 mm. The wavelength and amplitude that can be reliably produced are limited by the infrastructure's precision and therefore could not be smaller.

Table 3.13: Characteristics of simulated waves at SSPA

Characteristic	Value
Wave length	1 m
Wave amplitude	0.025 m
Wave steepness	2.5%
Wave period	0.73 s
Wave velocity	1.37 m/s

The procedure of determining the wave period is explained in section 4.2.3

Measurements

A force measuring device is fixed to the top of the wing and then fixed to the carriage. The sensor measures forces in the flow direction (drag) and the z-direction (lift). The data is then collected and processed to plot the force evolution as a function of the AoA and for different speeds and depths.

Figure 3.22: Force measurement setup during front wing towing tank tests at SSPA

Sonar study

While running towing tank tests on the front strut and wing, the JSN-SR04T sonar is placed approximately 560 mm above water level to perform measurements and study its precision and responsiveness. Through this study, the objective is to refine the knowledge about the sonar and ensure that it is adapted to the intended use for this project.

During the runs, the sonar is connected to the flight controller and the data is collected via the telemetry antennas. The measurements can then be converted from

a Mission Planner log to a Matlab data file for further analysis.

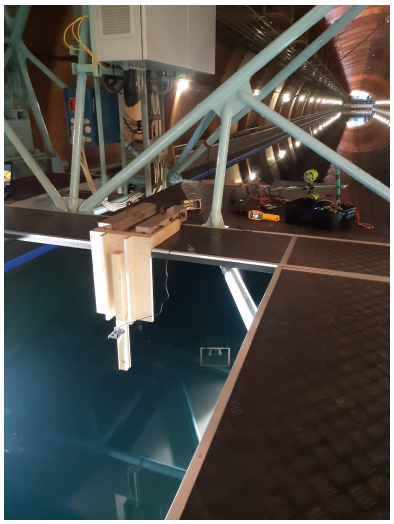

Figure 3.23: Sonar setup at SSPA's towing tank

3.3.4 Field test

The purpose of testing the model in an open field is to see the resulting behavior of the model. As all prior tests have been done in closed facilities at SSPA, the combination of using the actuators and motors meanwhile maneuvering and trying to obtain lift-off is of interest. The dual thruster setup is shown in Figure 3.8(b) is used for the field test.

It is difficult to conduct precise tests in a lake, thus the procedure of testing the model is to maneuver around for an unspecified duration to see the performance in different flight modes. Manual flight mode and stabilize flight mode were tested for several minutes each.

At this design stage of the system, the location of the wings in relation to the center of gravity (CoG) is not crucial for the system to work. As long as the water line is somewhat level, this is acceptable. In later design iterations and testing phases, this of course needs to be measured extremely carefully as the CoG will have a great impact on the performance of the model and adjustments of the actuators. For the field test, the longitudinal placement of the front wings was 420 mm from the beginning of the longitudinal aluminum tube (ID: 1.1). The vertical placement of the transversal aluminum tubes (ID: 1.2) was 195 mm (measured from center to center of the aluminum tubes). The transversal placement of the front wings was set to the maximum width possible with the installed 1000 mm transversal aluminum tube (ID: 1.2). The vertical position of the rudder was also set to the maximum height on the rail system (ID: 3.1) as was the case in the towing tank test of the bare hull and rudder. Figure 3.24 shows the setup in Rådasjön lake.

The field test was performed in sunny conditions with a slight breeze from time to time. The circumstances could not have been much better as the impact from waves and currents on the model was minimal. No traces were left on location.

Figure 3.24: Field test in Rådasjön lake

3.3.5 Workshop inclining test

For validation purposes, an inclining test is performed in the workshop. This small test is used to see how the servos respond to the constant change in pitch and roll motions. These motions are done by hand. Two tests are performed. First rolling and then pitching while the model is laying on top of two boxes to gain some elevation to perform the motions. The motions are repeated twice and each position is held for a few seconds. The flight controller is connected to Mission Planner and the flight mode is set to stabilize meanwhile the inclining is done. The data can then be extracted and analyzed.

Figure 3.25: Workshop inclining test setup

4
Results

The outcomes of the numerical and experimental investigations are described in the following chapter. They are intended to constitute the core of the comparison between theory and its implementation and will result in a discussion on discoveries made and their validity.

4.1 Results from CFD simulations

This section presents the various results obtained from CFD simulations. The end goal is not a validation study but rather a quantitative study that will refine the understanding of the flow phenomena to improve the operation of the model.

4.1.1 Surface interaction study

This study aims to determine an optimal depth of the foils regarding lift to drag optimization. Different AoA at different depths are simulated for a velocity of 4 m/s (target cruise velocity). Results from these simulations such as lift and drag are measured and then related to the development of vortical structures, pressure distribution, and wave patterns to explain the phenomena observed. As explained in section 3.2.1, the study was carried out with the wing profile AS5046 that has a chord length $c = 60$ mm.

Lift and drag

The results obtained from the simulations are displayed in Appendix F.2 and plotted as a function of the depth in Figure 4.1 and Figure 4.2. It can be observed that both drag and lift decrease the closer the foils get to the water surface. The major variations occur between $d = 0.5c - 1c$ leading to a substantial undesired decrease of lift. However, the lift and the drag applied to the wing remain relatively constant between $d = 1c - 4c$. The drag produced by the strut should also be accounted for and a major difference would be observed between $d = 1c - 4c$. Consequently, it can be concluded that the ideal depth of the wings for the operation of the model resulting in good lift and high reduction of the drag is situated between $d = 1c - 1.5c$.

It can be observed that for AoA $= 8^o$ and AoA $= -8^o$, the lift and drag obtained are not equal, that is due to the asymmetry of the wing.

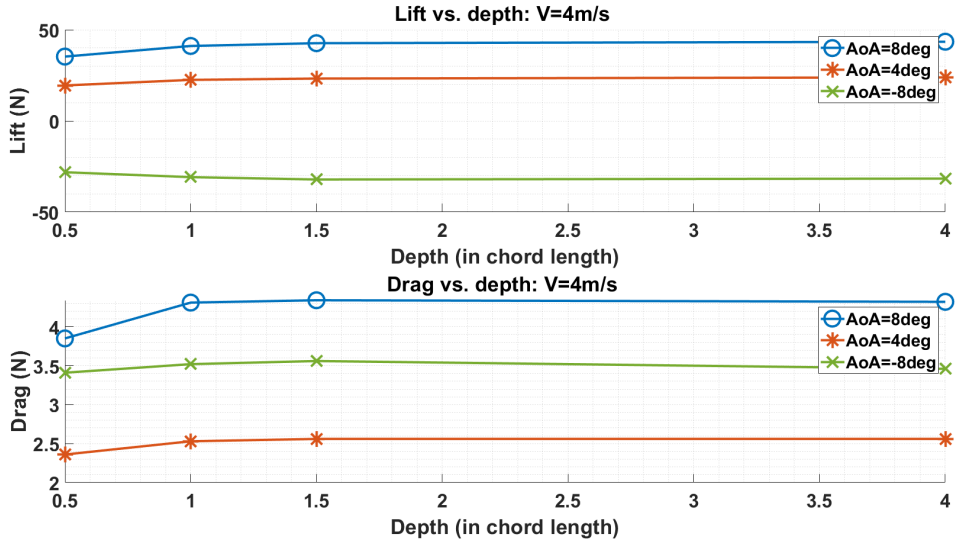

Figure 4.1: Lift and drag forces vs. depth from surface interaction study

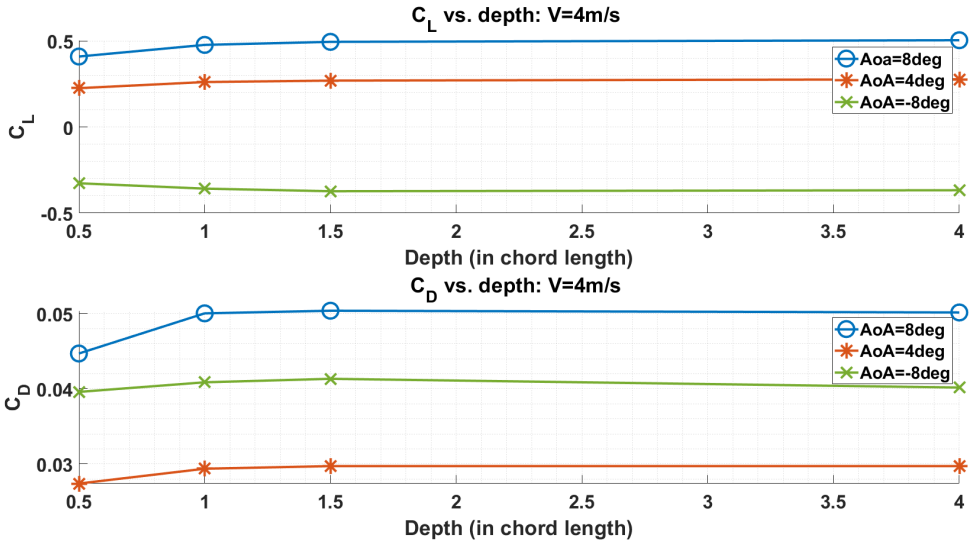

Figure 4.2: C_L and C_D vs. depth from surface interaction study

To understand the phenomena leading to the drag evolution previously shown, the pressure coefficient C_P and the skin friction coefficient C_F are plotted over the length of the foil for $[\text{AoA} = 8^o,\ d = 4c]$ and $[\text{AoA} = 8^o,\ d = 1c]$.

The pressure coefficient C_P is defined as:

$$C_P = \frac{P - P_\infty}{0.5 \cdot \rho \cdot \mathrm{V}^2}$$

Where:

- ρ is the density of the fluid

- V is the free stream velocity
- P_∞ is the static pressure in the free stream
- P is the static pressure at the point where C_P is evaluated

The skin friction coefficient C_F is defined as:

$$C_F = \frac{\tau_w}{0.5 \cdot \rho \cdot \mathrm{V}^2}$$

Where:

- ρ is the density of the fluid
- V is the free stream velocity
- $\tau_w = \mu \frac{\mathrm{du}}{\mathrm{dy}}$ is the skin shear stress
- μ is the dynamic viscosity of the fluid

The plot of C_P shows the same evolution for both cases but shifted vertically due to the difference of hydro-static pressure.

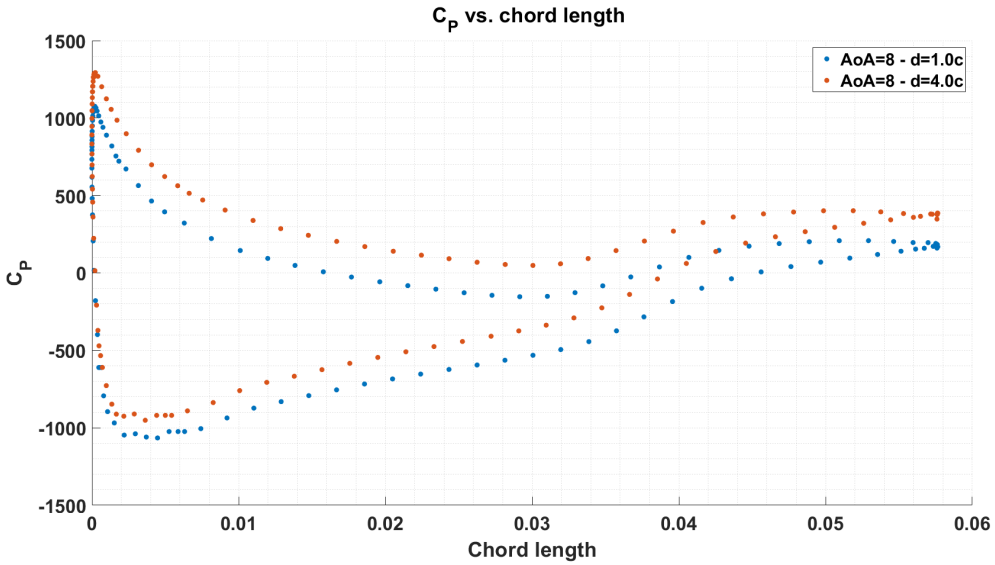

Figure 4.3: C_P comparison of [AoA $= 8^o,\ d = 1c$] and [AoA $= 8^o,\ d = 4c$]

However, differences in the C_F plot between the two cases can be noted. The effect of skin friction remains almost unchanged on the pressure side but is increased on the suction side at greater depths. Since this variation occurs only on the suction side it can be concluded that it is due to the influence of the free surface.

An increase of C_F is due in this case to an increase of skin shear stresses τ_w . The skin shear stresses being a phenomenon acting tangentially to the foil's surface and proportional to the viscosity μ it can therefore be associated with the drag and would explain the increase of resistance as the depth increases as it is shown in Figure 4.1.

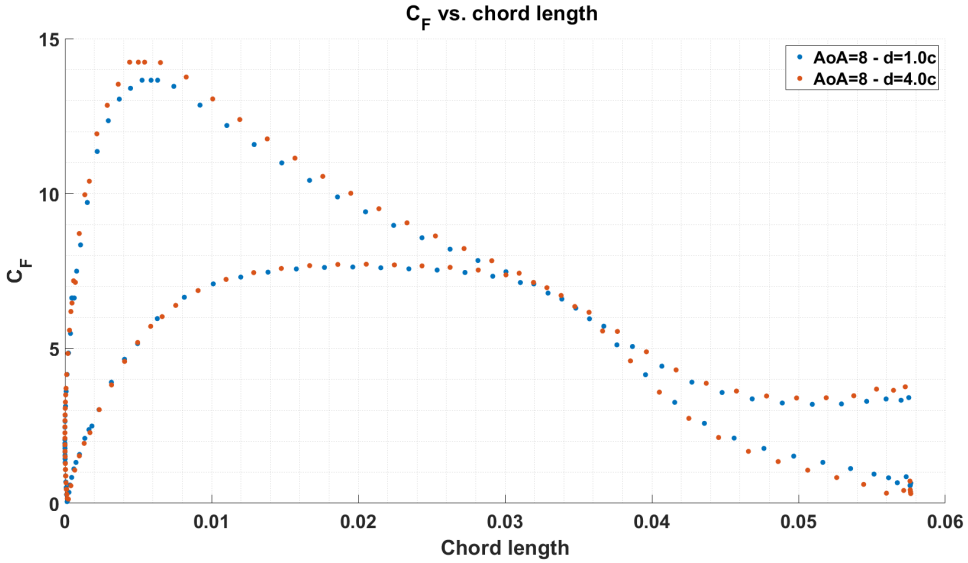

Figure 4.4: C_F comparison of [AoA $= 8^o$, $d = 1c$] and [AoA $= 8^o$, $d = 4c$]

Wave pattern created

Figure 4.5 shows the wave patterns created by the AS5046 wing at $d = 0.5c$ and $d = 1.5c$. It can be observed that the wave amplitude created by the $d = 0.5c$ is larger than at $d = 1.5c$. That is due to the displaced water on the suction side closer to the water surface resulting in a larger wave top. As a consequence of a large wave top, the valley of the wave will consequently become deeper resulting in a larger amplitude than for $d = 1.5c$.

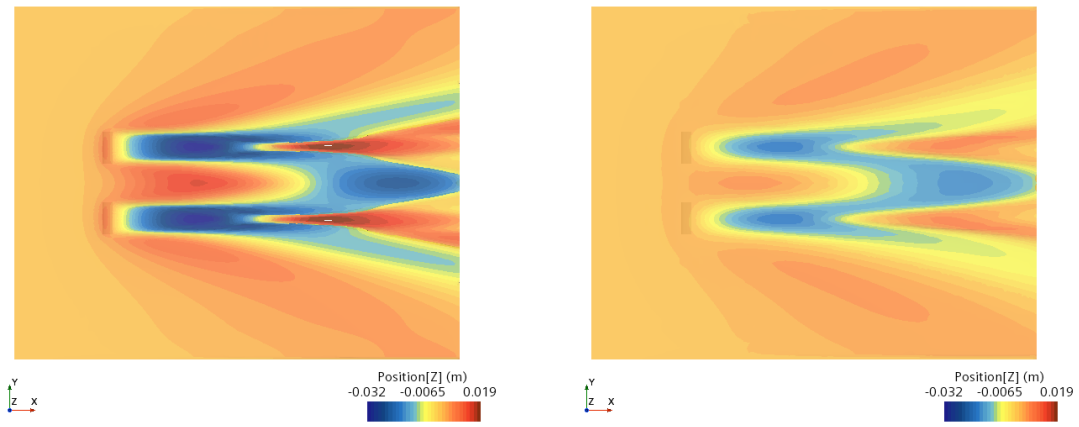

(a) $d = 0.5c$ **(b)** $d = 1.5c$

Figure 4.5: Wave pattern comparison between $d = 0.5c - 1.5c$ for AS5046 wings at AoA $= 8^o$

Pressure distribution

The differences in pressure distribution between the pressure and suction sides result in lift. The first observation that can be made is that the pressure side of the foils have a higher overall pressure than the suction side. While the whole pressure side is subject to positive pressure (orange to red regions), most regions of the suction side are subject to negative pressure (blue and yellow regions).

While the same observations can be made for both cases, the pressure difference is however more obvious for the foil positioned at $d = 1.5c$ (Figure 4.6(b) and (d)). The decrease of lift occurring on the less submerged foil is mainly due to the increase of pressure on the suction side. Hence the more important lift force measured at $d = 1.5c$ than at $d = 0.5c$.

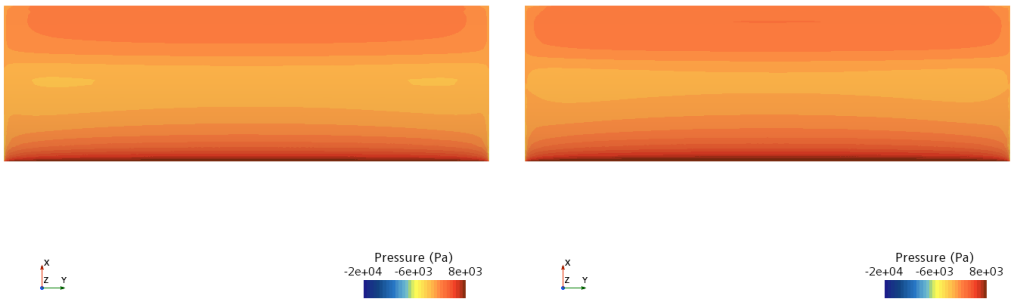

(a) Pressure side: $d = 0.5c$ **(b)** Pressure side: $d = 1.5c$

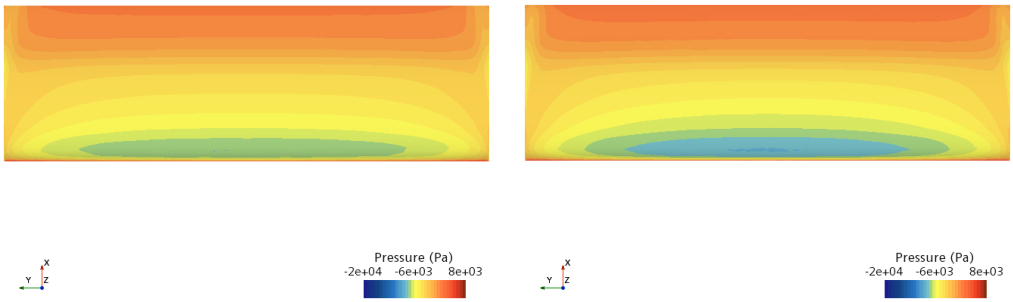

(c) Suction side: $d = 0.5c$ **(d)** Suction side: $d = 1.5c$

Figure 4.6: Pressure comparison $d = 0.5c - 1.5c$ for AS5046 wings at AoA $= 8^o$

Q-criterion

A commonly used method to visualize the creation of vortical structures in the flow is the representation of the Q-criterion. The Q-criterion definition is based on the following equation:

$$\mathrm{Q} = \frac{1}{2} \cdot (\|\Omega\|^2 - \|\mathrm{S}\|^2)$$

Where Ω is the vorticity tensor defined as:

$$\Omega = \frac{1}{2} \cdot (\frac{\partial u_i}{\partial x_j} - \frac{\partial u_j}{\partial x_i})$$

And S is the strain rate tensor defined as:

$$\mathrm{S} = \frac{1}{2} \cdot (\frac{\partial u_i}{\partial x_j} + \frac{\partial u_j}{\partial x_i})$$

Therefore, in the region where Q takes high values it translates the dominance of the vorticity tensor Ω and thus the presence of vortical structures in those regions.

Figure 4.7 show tip vortices being developed at $d = 0.5c$ and $d = 1.5c$. However, additional structures can be observed downstream and close to the wing for $d = 0.5c$ but that are not present for $d = 1.5c$ and deeper. Those structures are due to the proximity of the water surface. The Q-criterion isovalue used for the plots is $300/\mathrm{s}^2$.

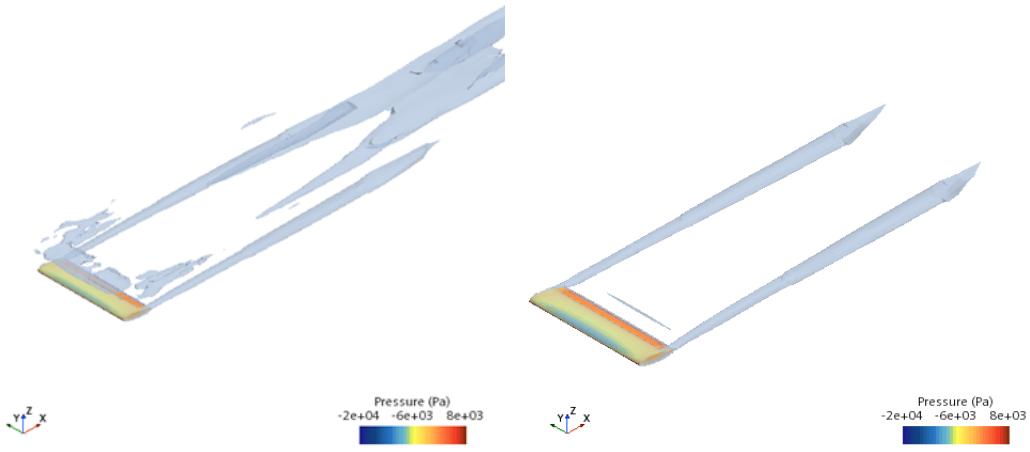

(a) $d = 0.5c$ / AoA $= 8^o$ **(b)** $d = 1.5c$ / AoA $= 8^o$

Figure 4.7: Q-criterion comparison between $d = 0.5c - 1.5c$ for AS5046 wings at AoA $= 8^o$

The tip vortices are caused by the difference in pressure between the suction and the pressure sides. This pressure gradient forces the flow at the bottom of the wing

to want to go to the top side resulting in the creation of a rotational flow at the tip of the wing. Consequently, the more important the gradient is, the more important should be the vortices. The difference in sizes in the structures can easily be observed in Figure 4.8 due to the presence of a high difference in pressure gradient since for the case in Figure 4.8(a) the lift is 22.51 N whereas in Figure 4.8(b) the lift is 42.63 N.

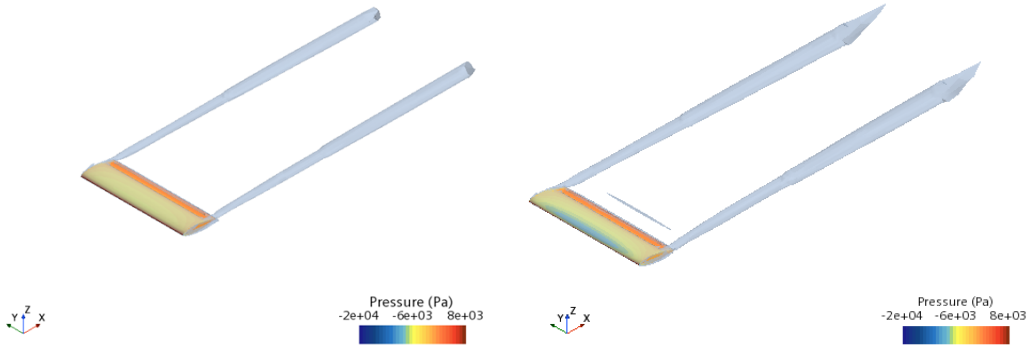

(a) $d = 1c$ / AoA $= 4^o$ **(b)** $d = 1.5c$ / AoA $= 8^o$

Figure 4.8: Q-criterion comparison between two cases with large lift difference of AS5046 wings

4.1.2 Implementation of a PID controlling the lift in Star CCM+

Successful implementation of the PID is indicated by a robust control of the lift which is translated by maintaining the error close to zero over time. This is done by fulfilling two requirements: 1) a correct setup of the various reports, parameters, and field functions in Star CCM+ that define Eq. 3.1 and 2) a correct tuning of the parameters of the aforementioned equation. The method used to set up the simulation is detailed in section 3.2.2.

Tuning of the PID

By feeding the online PID tuner[1] with the input and output data acquired by doing a step response test, the adequate parameters specific to the system can be determined. Even though the step simulated is not a perfect square signal, the changes are abrupt enough to consider it to be a step. The result of the test is visualized in Figure 4.9. Note that the channel domain and thus the wing, are very narrow

[1] https://pidtuner.com/#/

resulting in a very small measured lift.

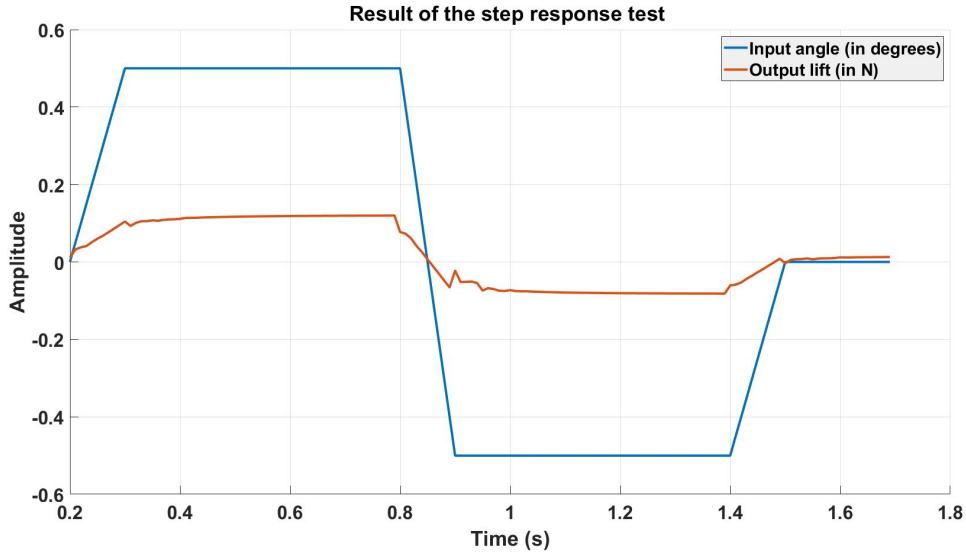

Figure 4.9: Result of the step response test carried out in the PID simulation

This result allowed to identify the system as a first order model with the corresponding defining parameters:

Parameters	Value
Proportional gain K_p	0.01539
Integral time T_i (in s)	0.00377
Derivative time T_d (in s)	0
Integral gain K_i	4.0817
Derivative gain K_d	0

Table 4.1: PID parameters defining the system

It can be observed that the derivative term is unnecessary to control the lift. It is therefore not a PID controller but a PI controller. The reason is that the system is responsive and precise enough to do without the anticipation role of the D term. Indeed, the derivative term is a prediction term that makes use of the variations at an instant t to estimate what will be the behavior of the system T_d seconds ahead. This is particularly useful to prevent overshooting for systems that respond slowly. It will come into play to dampen the response especially when inertia is an important factor.

Behavior of the wing under PID control

The following section is intended to show how the lift, the error, and the rate of change of the AoA change over time when the PID is at work. The target lift is 0.5 N in this case and was chosen as an example based on the range of lift that the narrow wing can produce.

Figure 4.10 reflect how the wing is rotated to attain the target lift despite the disturbances caused by the waves. After the initial unstable phase of the simulation, the lift approaches and then varies around the target lift of 0.5 N resulting in a progressive decrease in the rate of change of the AoA necessary to maintain its objective.

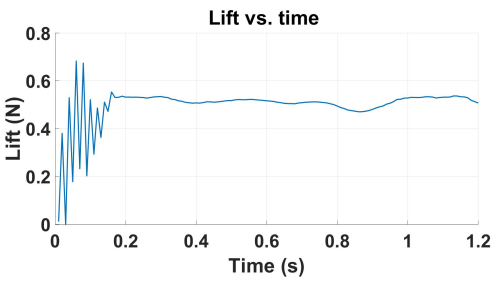

(a) Evolution of the lift

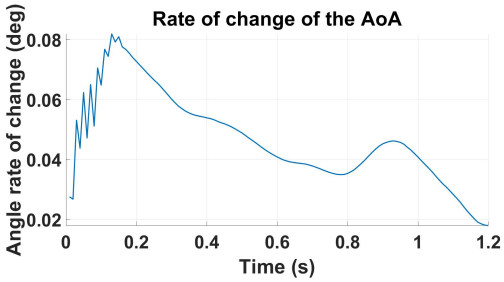

(b) Evolution of the rate of change of the AoA

Figure 4.10: Behavior of the wing under the control of the PID

The same behavior is illustrated this time with the variation of the error around zero showing that the PID controller can return to its desired position despite the wave disturbances on the lift.

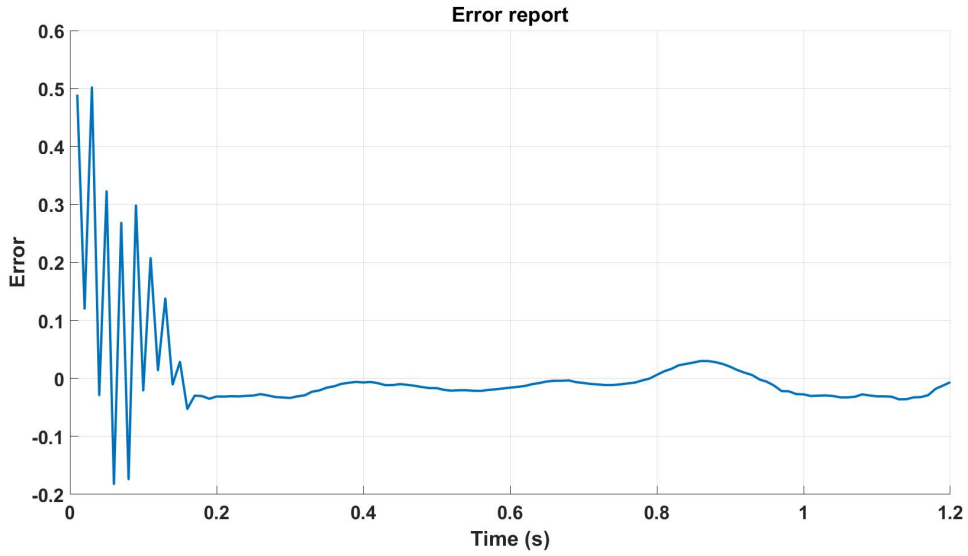

Figure 4.11: Evolution of the error under PID control

4.1.3 Simulation of wing with strut in calm water

Performing this CFD analysis provides data to be compared to experimental results. The goal is to identify the differences in the results and determine what are their origins to improve the simulation setup to some extent. Since the geometry simulated differs from the wing tested at SSPA, it is not possible to observe the exact same forces but the goal is to have a simulation as relatable as possible.

Lift and drag

Figure 4.12 shows the mean lift obtained. As the speed increases, so does the lift force. Configurations simulated at $d = 120$ mm have larger lift forces compared to the same configuration at $d = 80$ mm. That is also what is expected with respect to the results from the surface interaction study in section 4.1.1. It can observed that the lift forces created at AoA $= 2^o$ are similar for all configurations. It is expected that $V = 4$ m/s configurations yield larger lift forces. On the contrary, it can be observed that the $V = 2$ m/s configurations are resulting in more lift. Figure 4.20 shows the pressure distribution on the wing between $V = 2$ m/s and $V = 4$ m/s configurations. It can be observed that the pressure is larger for $V = 2$ m/s. Figure B.1(a) also shows how C_L is decreasing at higher Reynolds number. This can explain the small lift force observed at AoA $= 2^o$ for $V = 4$ m/s.

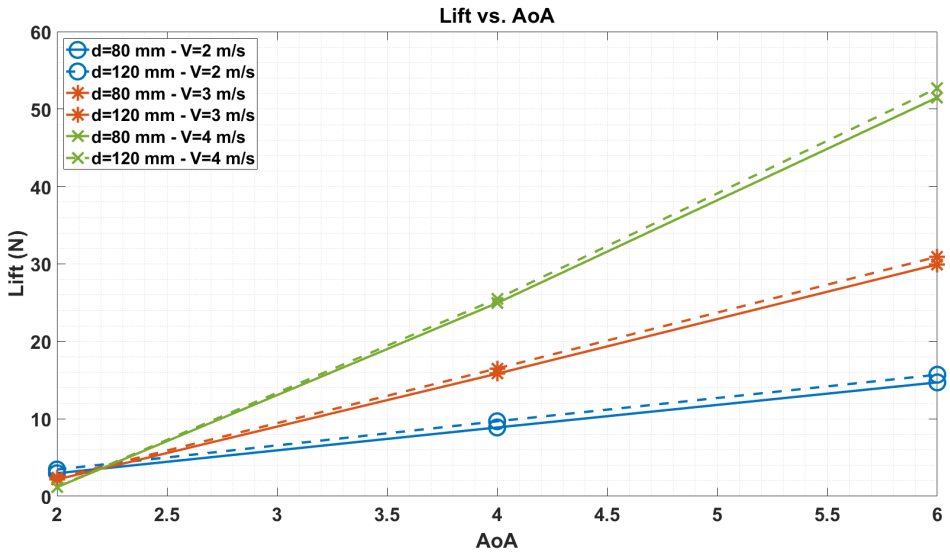

Figure 4.12: Lift vs. AoA - Calm water CFD simulations of wing with strut

Figure 4.13 shows the lift coefficient obtained. As the speed decreases, C_L increases. Furthermore, C_L is larger at $d = 120$ mm compared to $d = 80$ mm due to the water surface interaction. The same pattern can be observed for all C_L. It is noticeable that the lower velocities are resulting in larger C_L compared to the higher velocity configurations. This correlates with the foil's decreasing C_L at a higher Reynolds number as can be observed in Figure B.1(a).

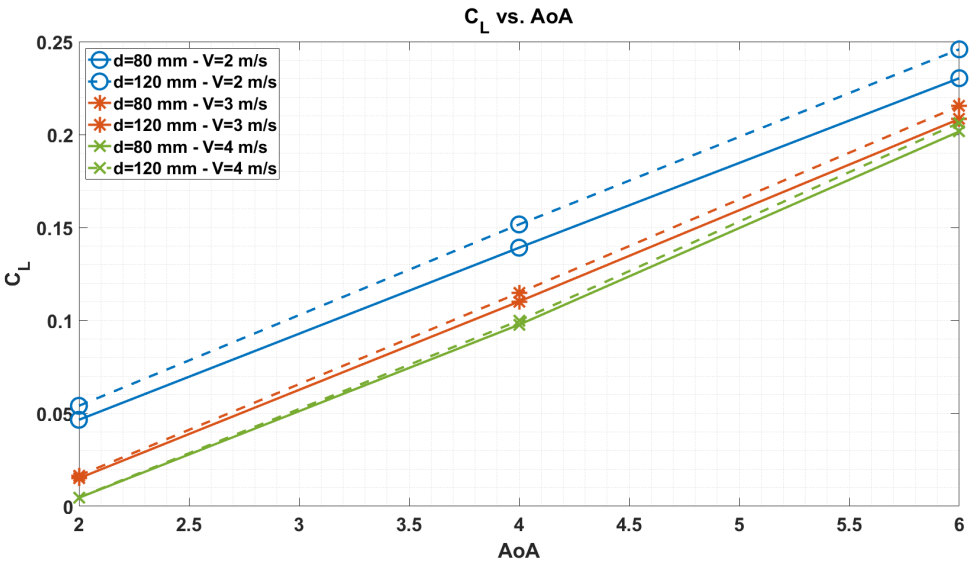

Figure 4.13: C_L vs. AoA - Calm water CFD simulations of wing with strut

As shown in Figure 4.14, the drag increases with depth. This is natural due to a larger wetted strut area in deeper configurations but also due to the increasing C_D as shown in Figure 4.2. The drag is also increasing with velocity. That is also natural as the drag is proportional to V^2.

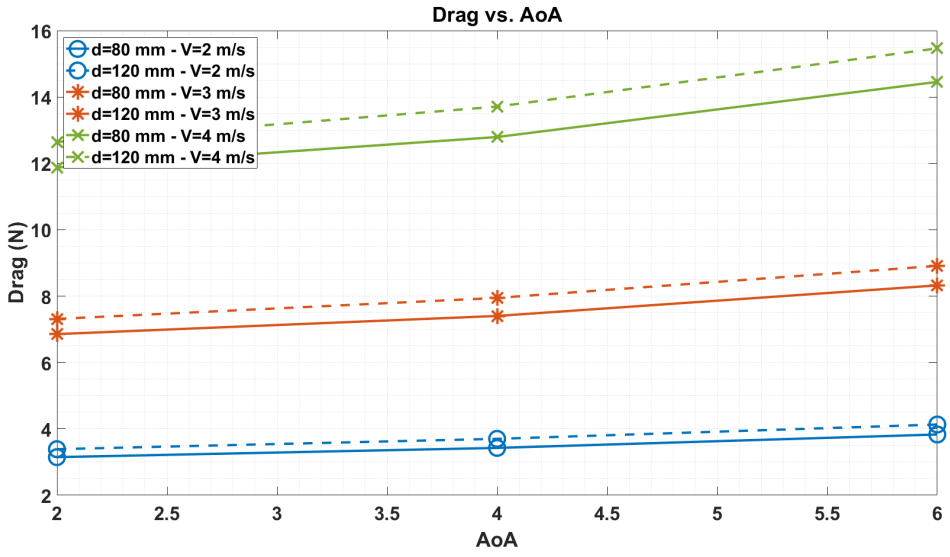

Figure 4.14: Drag vs. AoA - Calm water CFD simulations of wing with strut

Figure 4.15 shows how the largest C_D is obtained in the $V = 2$ m/s configurations compared to the $V = 3$ m/s and $V = 4$ m/s configurations. This correlates with the C_D observed in Figure B.1(b) where higher Reynolds numbers are resulting in lower C_D.

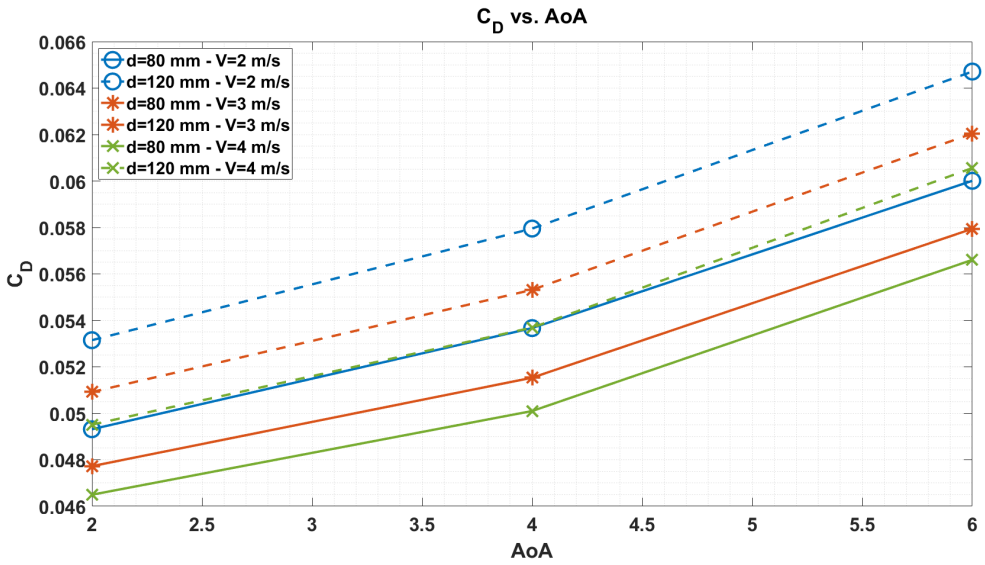

Figure 4.15: C_D vs. AoA - Calm water CFD simulations of wing with strut

Wave pattern and sprays

Two sources of energy loss can be observed by looking at the interactions between the foil and the water surface: the splashes and the waves. The following section will display how these losses vary depending on speed, depth and AoA.

- Sensitivity to speed: To better demonstrate the influence of speed on the water surface perturbations, the AoA $= 6^o$ and the foils are positioned close to the water surface. Therefore the case represented are [$d = 80$ mm, AoA $= 6^o$, $V = 2$ m/s] and [$d = 80$ mm, AoA $= 6^o$, $V = 4$ m/s].

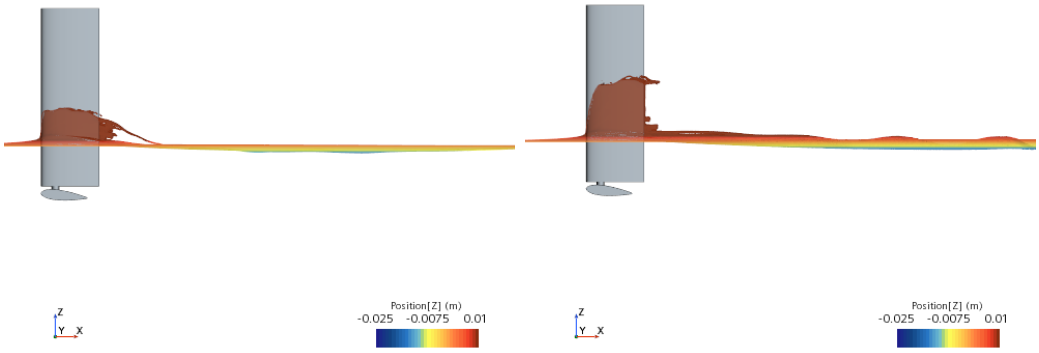

(a) $V = 2$ m/s **(b)** $V = 4$ m/s

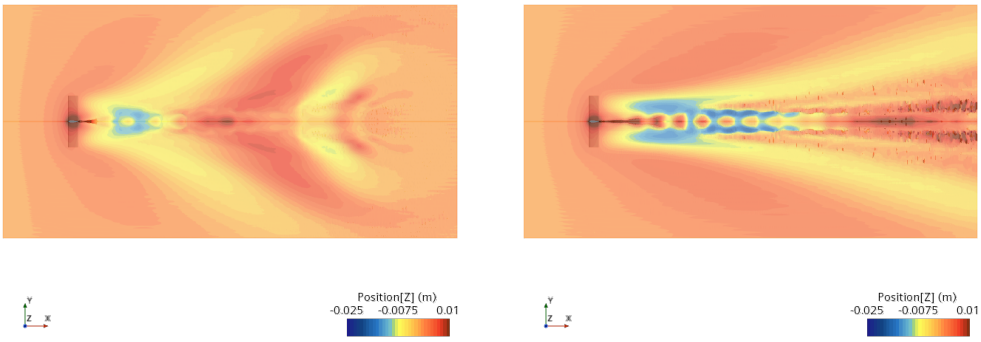

(c) $V = 2$ m/s **(d)** $V = 4$ m/s

Figure 4.16: Influence of the speed on water surface perturbations - Comparison between [$V = 2$ m/s, $V = 4$ m/s] with [$d = 80$ mm, AoA $= 6^o$]

Figure 4.16 shows a clear increase in water surface perturbations as the speed increases. The sprays and the waves created are much more important when $V = 4$ m/s and that results in a higher drag for this case than for the $V = 2$ m/s case.

- Sensitivity to depth: Varying the depth is expected to have mainly an influence on the waves generated due to the presence of the foil and not on the splashes created. To better visualize the wave generation, the AoA should take a high value and the speed should have a low value to limit the presence of splashes. Hence the cases shown below: [$d = 80$ mm, AoA $= 6^o$, $V = 2$ m/s] and [$d = 120$ mm, AoA $= 6^o$, $V = 2$ m/s].

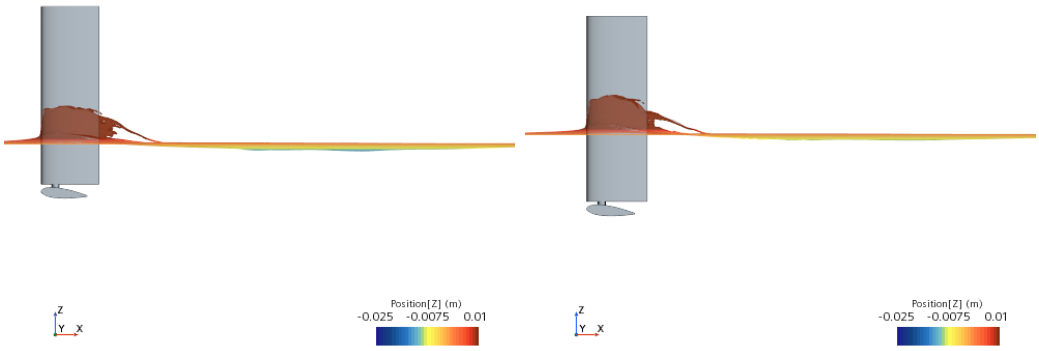

(a) $d = 80$ mm **(b)** $d = 120$ mm

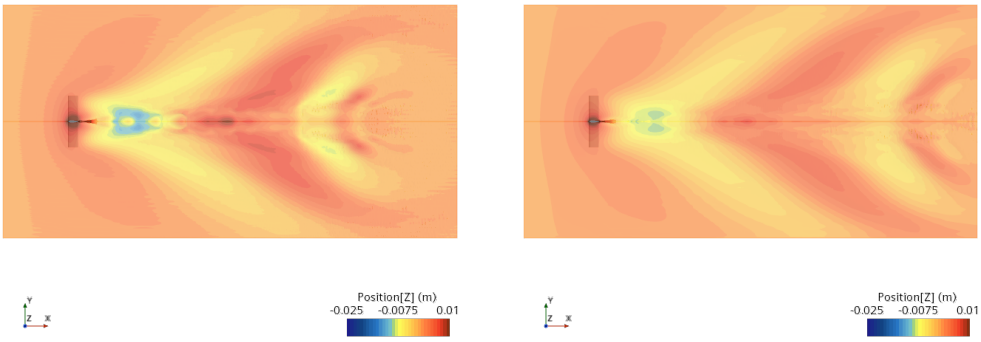

(c) $d = 80$ mm **(d)** $d = 120$ mm

Figure 4.17: Influence of the depth on water surface perturbations - Comparison between [$d = 80$ mm, $d = 120$ mm] with [AoA $= 6^o$, $V = 2$ m/s]

Figure 4.17(a) and Figure 4.17(b) show that the splashes are not affected by the change of depth. On the other hand, a difference in wave amplitude can be noticed with larger waves for $d = 80$ mm (Figure 4.17(c)) than for $d = 120$ mm (Figure 4.17(d)).

- Sensitivity to AoA: The influence of the AoA is emphasized by taking cases close to the water surface and with a low speed to limit sprays. The cases selected are therefore: [$d = 80$ mm, AoA $= 6^o$, $V = 2$ m/s] and [$d = 80$ mm, AoA $= 2^o$, $V = 2$ m/s].

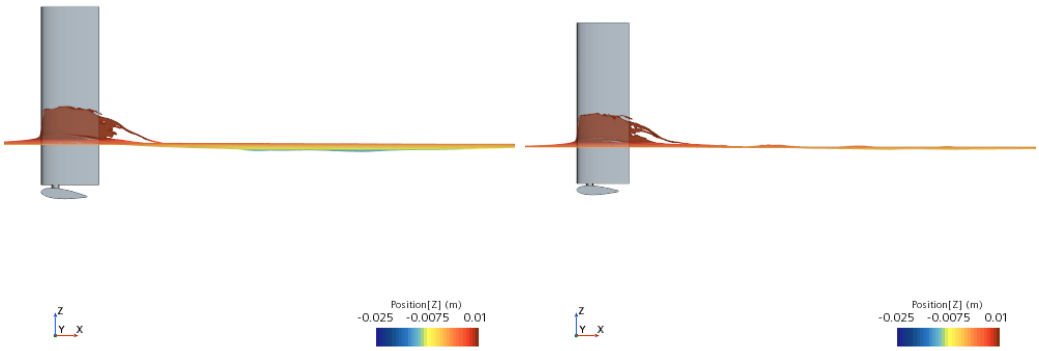

(a) AoA $= 6^o$ **(b)** AoA $= 2^o$

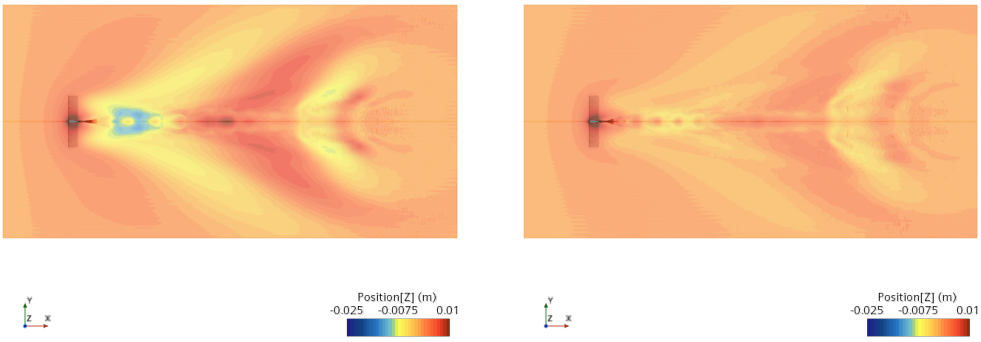

(c) AoA $= 6^o$ **(d)** AoA $= 2^o$

Figure 4.18: Influence of AoA on water surface perturbations - Comparison between [AoA $= 6^o$, AoA $= 2^o$] with [$d = 80$ mm, $V = 2$ m/s]

The change of AoA does not affect the splashes created but affects instead the waves generated with higher wave amplitude for a more important AoA.

Pressure distribution

In this section, the pressure distribution is compared between two cases that have an important lift difference. Therefore, based on the results diplayed in Figure 4.12 the following cases are chosen: [$d = 120$ mm, AoA $= 6^o$, $V = 4$ m/s] and [$d = 120$ mm, AoA $= 6^o$, $V = 2$ m/s.]

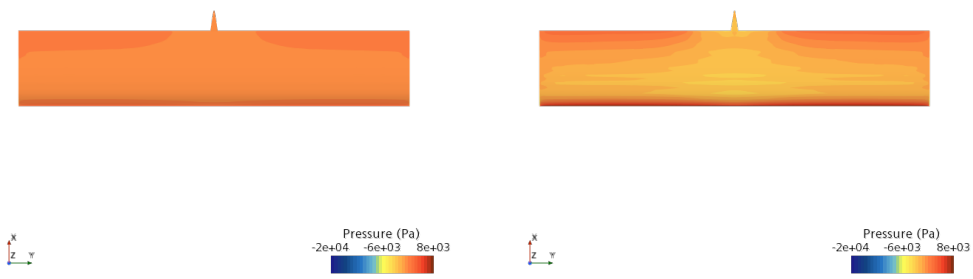

(a) Pressure side: $V = 2$ m/s **(b)** Pressure side: $V = 4$ m/s

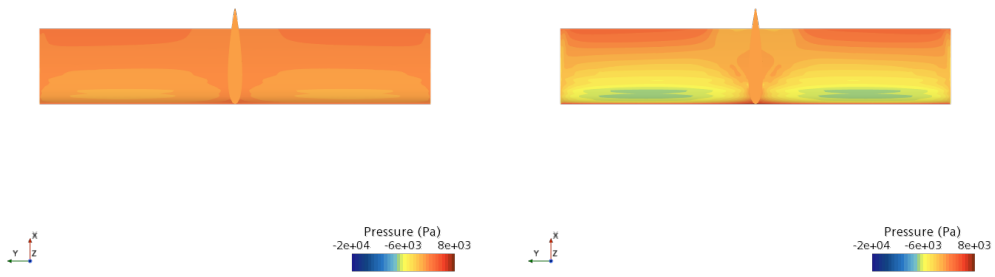

(c) Suction side: $V = 2$ m/s **(d)** Suction side: $V = 4$ m/s

Figure 4.19: Pressure comparison between [$V = 2$ m/s, $V = 4$ m/s] for [$d = 120$ mm, AoA $= 6^o$]

Figure 4.12 shows an inversion of the cases producing the most lift for AoA inferior to 2.5^o. The cases with $V = 2$ m/s produce more lift than the cases with $V = 4$ m/s which contradicts the expectations and needs some treatment in simulation setups to correct it.

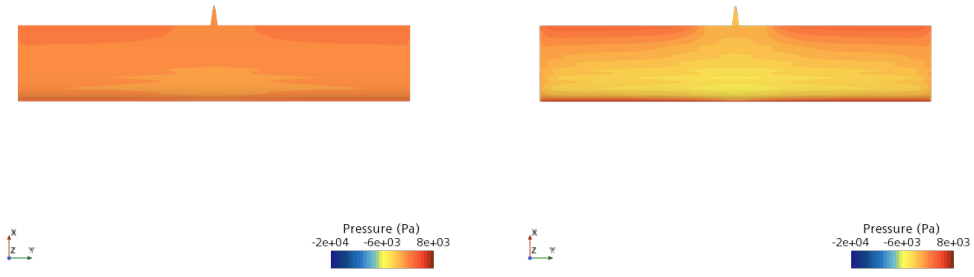

(a) Pressure side: $V = 2$ m/s **(b)** Pressure side: $V = 4$ m/s

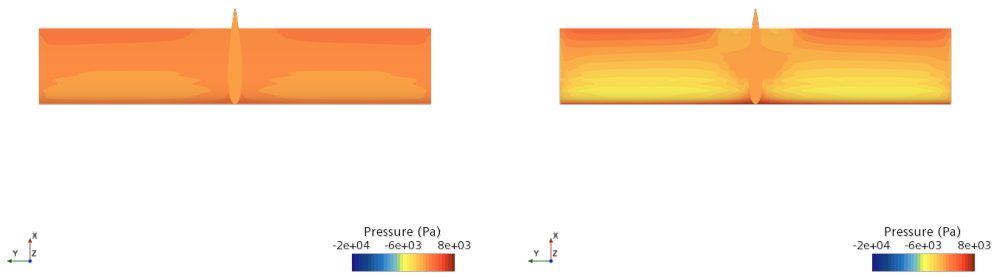

(c) Suction side: $V = 2$ m/s **(d)** Suction side: $V = 4$ m/s

Figure 4.20: Pressure comparison between [$V = 2$ m/s, $V = 4$ m/s] for [$d = 120$ mm, AoA $= 2^o$]

Q-criterion

This section is intended to show how the vortical structures represented by the Q-criterion evolve with the speed and the lift. As explained in section 4.1.1, the wing tips vortices are indeed related to the lift. The following plots are obtained by setting the Q-criterion isovalue to 300/s^2.

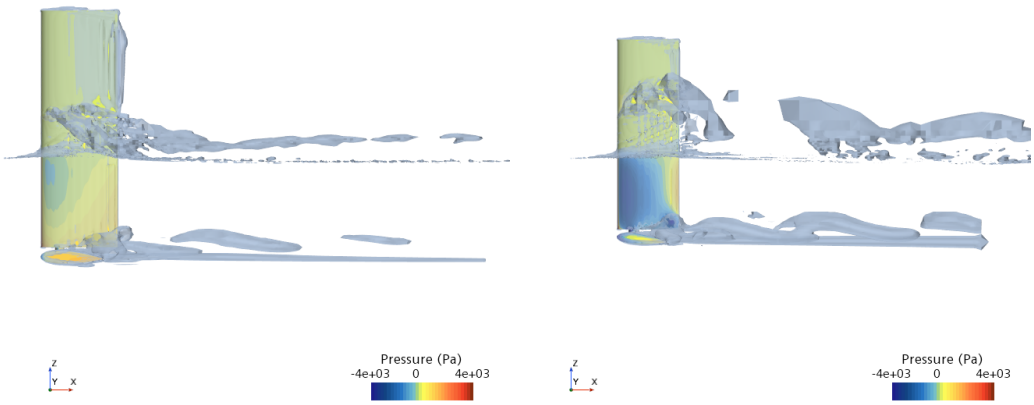

(a) AoA $= 2^o$, $V = 2$ m/s **(b)** AoA $= 6^o$, $V = 4$ m/s

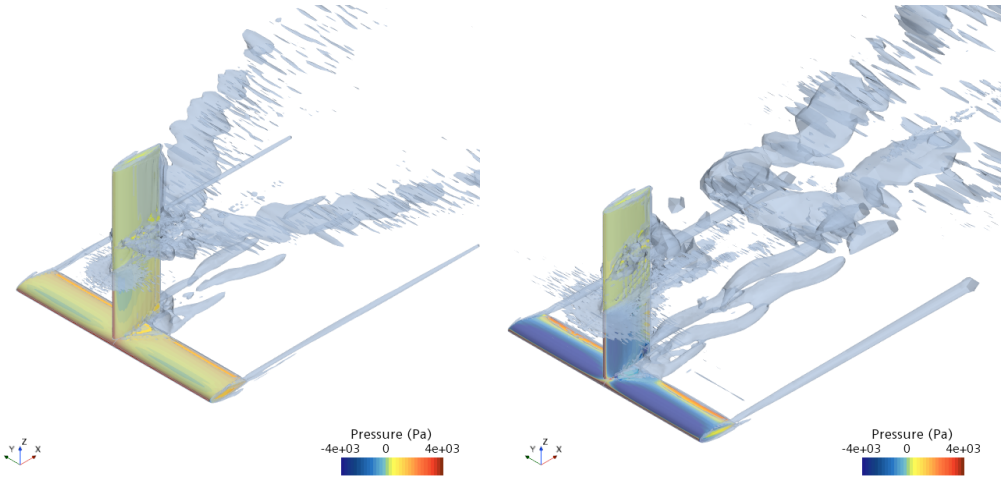

(c) AoA $= 2^o$, $V = 2$ m/s **(d)** AoA $= 6^o$, $V = 4$ m/s

Figure 4.21: Comparison of the vortical structures created for [$d = 120$ mm, AoA $= 2^o$, $V = 2$ m/s] and [$d = 120$ mm, AoA $= 6^o$, $V = 4$ m/s]

The vortical structures are more important for the higher speed case both in the wake of the strut and at the wing tips. The difference in size of the wing tips vortices is noticeable and corroborate with the fact that the high speed case produces more lift than the low speed one.

Relation between forces oscillations and vortex shedding

Solutions for lift and drag in CFD simulations show a periodic behavior rather than convergence towards specific constant force values. It can therefore be speculated that a physical flow phenomenon is at the source of such observation and especially the presence of the strut could be causing vortex shedding. To confirm or refute this hypothesis, an analysis of the force oscillation frequencies is carried out and compared to the behavior of the vortical structures created behind the strut.

First, the lift is plotted against time to extract the oscillation frequency. From the figure below, the oscillation period determined is $T_{lift} = 0.0475$ s which yields a frequency $f_{lift} = 21.05$ Hz.

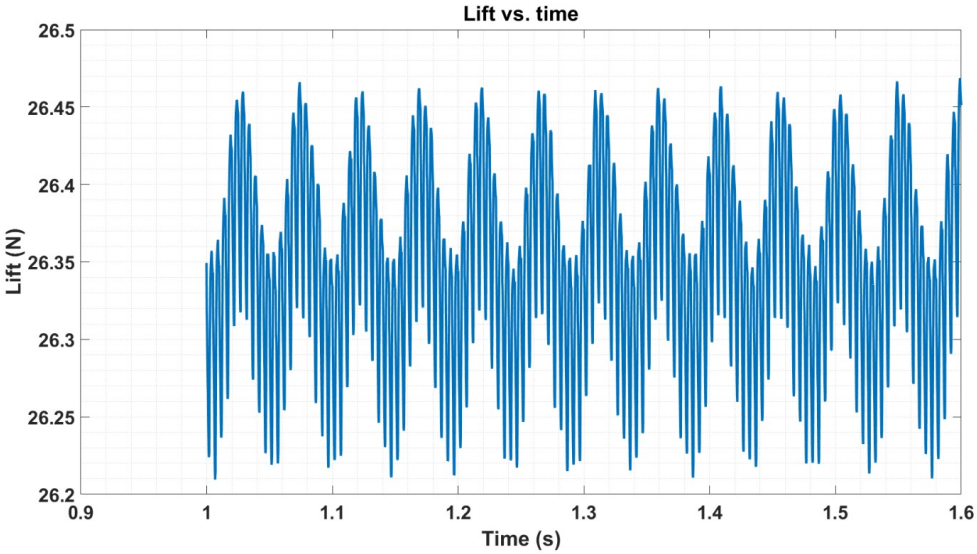

Figure 4.22: Lift vs. Time - Calm water CFD simulation for [d = 120 mm, AoA = 6^o, V = 4 m/s]

Then, the same procedure is applied for the drag which gives a period T_{drag} = 0.0478 s and thus a frequency f_{drag} = 20.92 Hz. The solution for the drag is plotted in Figure 4.23.

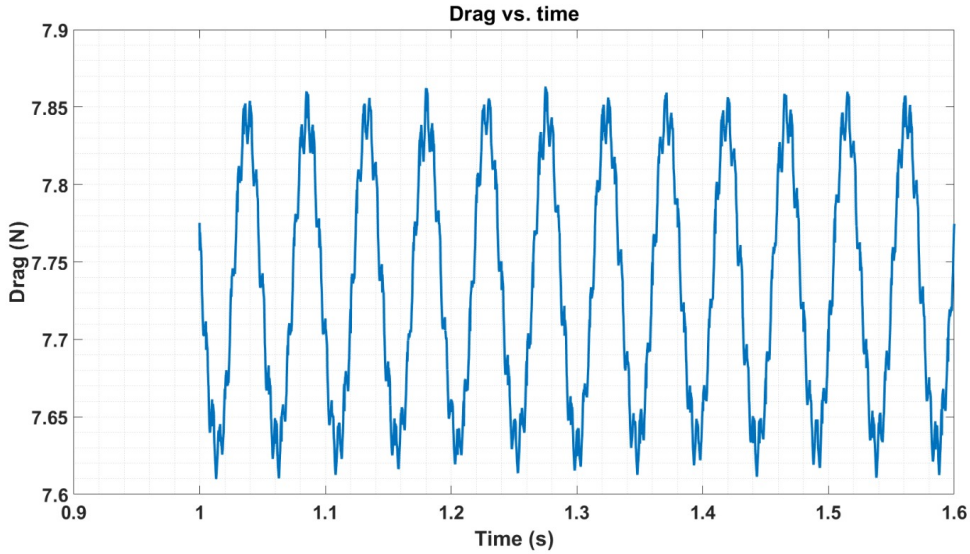

Figure 4.23: Drag vs. Time - Calm water CFD simulation for [d = 120 mm, AoA = 6^o, V = 4 m/s]

The evolution of the vortical structures are then observed over time to analyze if they behave periodically. The results have shown a repetition of the same structures every T_{Qcrit} = 0.0477 s hence a shedding frequency f_{Qcrit} = 20.96 Hz.

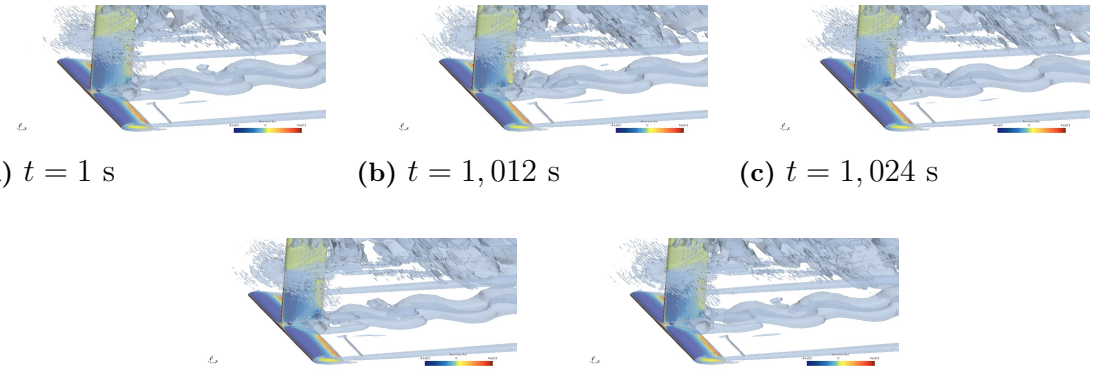

(a) $t = 1$ s **(b)** $t = 1,012$ s **(c)** $t = 1,024$ s

(d) $t = 1,036$ s **(e)** $t = 1,048$ s

Figure 4.24: Evolution of the vortical structures over a period T_{Qcrit}

The frequency analysis has put forward the relationship between the oscillation of the force solutions and the periodicity of the vortical structures. A common frequency of about 21 Hz has been demonstrated and combined to effect of the vortical structures on the pressure distribution shown by previous figures (see Figure 4.19 and Figure 4.20) the link can be established between vortex shedding and force variations.

Table 4.2: Comparison of forces and vortical structures frequencies

	Period	Frequency
CFD lift solution	$T_{lift} = 0.0475$ s	$f_{lift} = 21.05$ Hz
CFD drag solution	$T_{drag} = 0.0478$ s	$f_{drag} = 20.92$ Hz
Vortical structures development	$T_{Qcrit} = 0.0477$ s	$f_{Qcrit} = 20.96$ Hz

4.1.4 Simulation of wing with strut encountering waves

To complete the comparison study, a simulation of the foil in waves similar to the test case ran at SSPA was done. The objective here is to compare once again the lift and drag produced between CFD and EFD. The fifth-order waves simulated have a period of 0.73 s (same as the one determined from the experiments in section 4.2.3) and a wave amplitude of 25 mm.

Lift and drag

No simulation with the same AoA have been run in calm water to be compared to this test case. The comparison has thus to be made with experimental results even though geometries and structural properties (flexibility of the wings and strut for instance) that affect the lift and drag are not completely similar. This comparison

is done in section 5.1.2. The mean values from the CFD simulation with waves are shown in Table 4.3.

Table 4.3: Mean values from CFD wave simulation of [d = 80 mm, AoA = 12^o, V = 3 m/s] in waves

	Lift (N)	C_L (-)	Drag (N)	C_D (-)
Mean value from CFD	71.08	0.496	12.70	0.079

Wave pattern

The following figures show what the water surface looks like during the simulation. Compared to previous simulations in calm water, the wave height scale had to be adjusted to account for the higher amplitudes. While the water surface was previously varying between -0.025 - 0.01 m, the water surface is now varying between -0.05 - 0.03 m. The scale had to be changed of course because of the presence of waves generated but it could also be attributed to the higher AoA set in this simulation compared to calm water cases. Indeed, it was demonstrated in section 4.1.3 that the higher the AoA the higher the wave amplitudes are. Moreover, the splashes created in the present simulation with waves at V = 3 m/s are comparable to those of a simulation at V = 4 m/s such as the one shown in Figure 4.16(b).

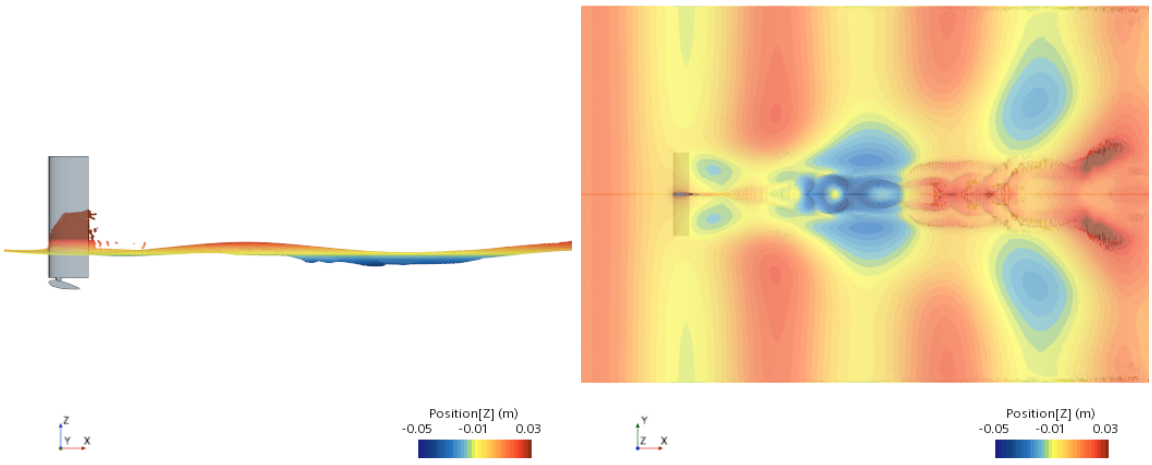

(a) Side view **(b)** Top view

Figure 4.25: Water surface disturbances in presence of waves for [d = 80 mm, AoA = 12^o, V = 3 m/s]

Pressure distribution

The effect of waves on lift and drag has been demonstrated previously. Since they are related to the pressure distribution over the wing, it is therefore of interest to relate the pressure distribution evolution to the wave pattern passing over the wings. Consequently, the pressure distribution is first shown for the pressure side and displayed next to the isosurface observed at the same instant. The figures are taken within the time frame of one encountered wave period. And then the same comparison is carried out for the suction side of the wing.

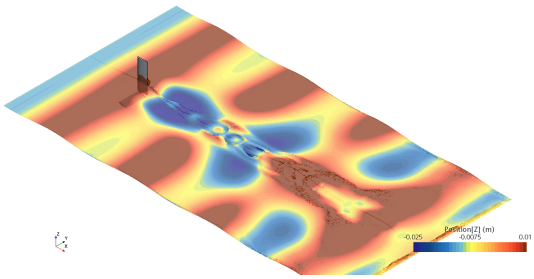

(a) t = 0.8575 s

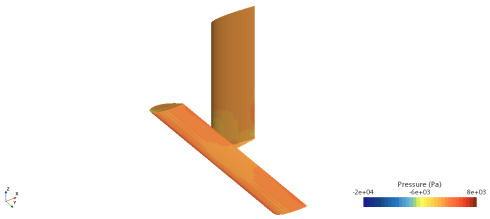

(b) t = 0.8575 s

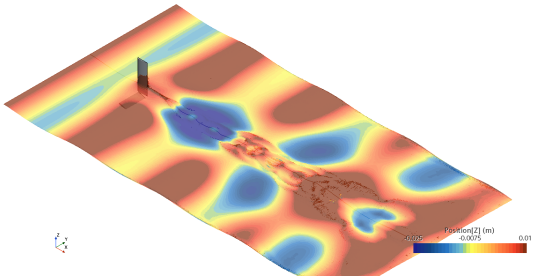

(c) t = 0.9275 s

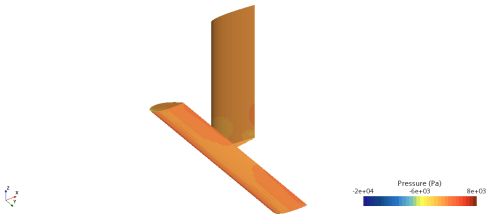

(d) t = 0.9275 s

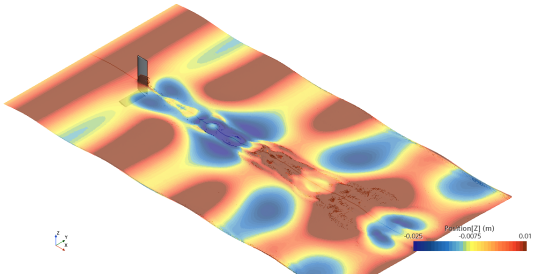

(e) t = 0.9975 s

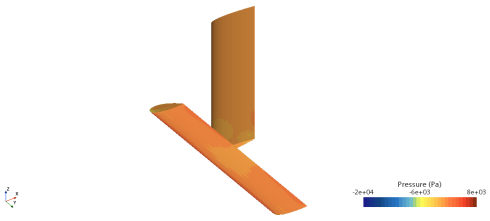

(f) t = 0.9975 s

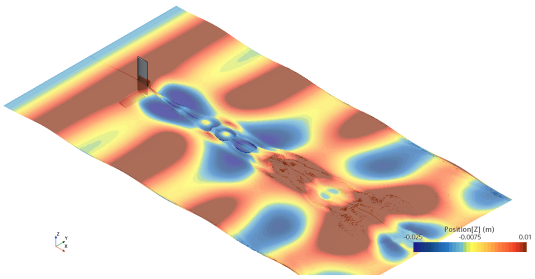

(g) t = 1.0425 s

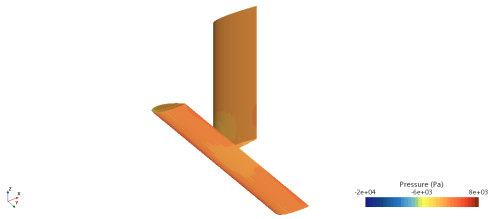

(h) t = 1.0425 s

Figure 4.26: Linking of the pressure distribution of the pressure side to the wave positions over a wave encountered period

The effect on the pressure side of the wing seems to be driven by the vortex shedding more than the hydrostatic pressure. Indeed, the center of the pressure side, below the strut, experiences a change of pressure locally and oscillates. The bursts of change in pressure happen at a higher frequency than the encountered wave frequency. Consequently, it can be speculated that the effects on the pressure side are mainly caused by the vortex shedding rather than the change in hydrostatic pressure. The same way of showing the pressure distribution is adopted for the suction side.

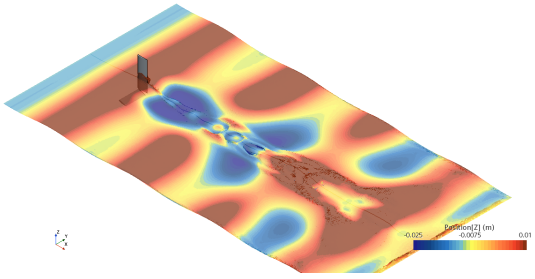

(a) t = 0.8575 s

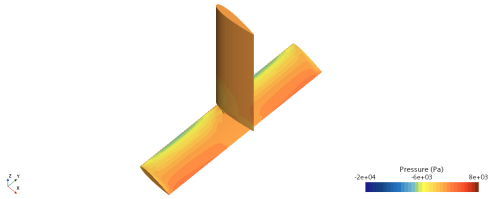

(b) t = 0.8575 s

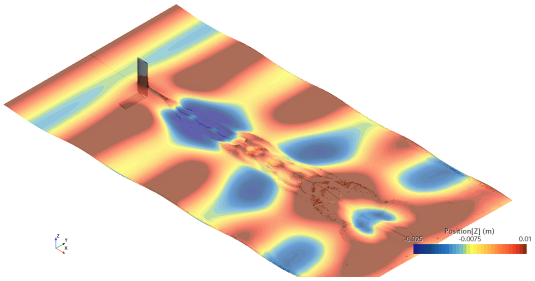

(c) t = 0.9275 s

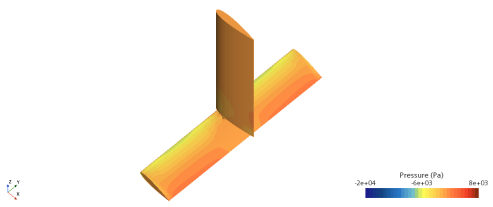

(d) t = 0.9275 s

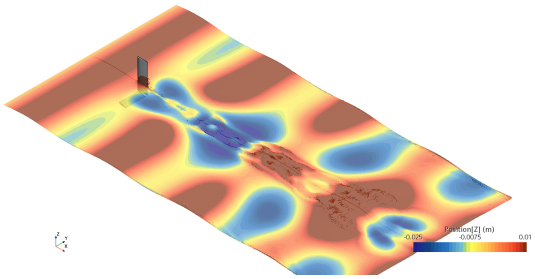

(e) t = 0.9975 s

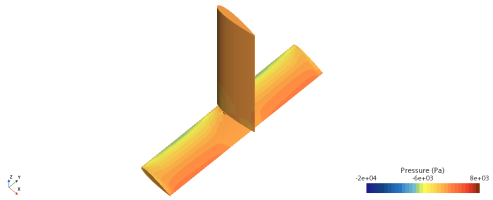

(f) t = 0.9975 s

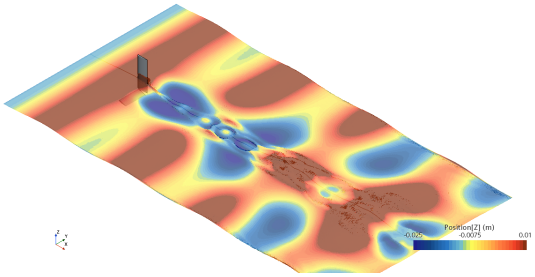

(g) t = 1.0425 s

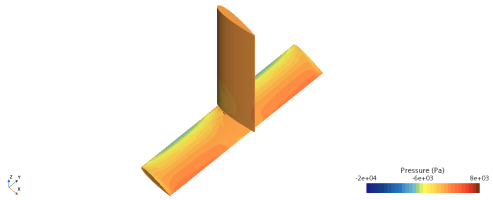

(h) t = 1.0425 s

Figure 4.27: Linking of the pressure distribution of the suction side to the wave positions over a wave encountered period

The observation of animations of the pressure distribution on the suction side of the wing reveals an effect of the waves on the entirety of the wing. No specific regions are concerned by an important drop or increase of pressure but instead the pressure of the whole suction side varies uniformly. The effect of vortex shedding can therefore be ruled out as the major factor in pressure variations on the suction side. The pressure variations does not seem to vary in accordance with the wave pattern. The bursts of change are happening more frequently than the variation of wave height over the wing. Therefore, it is hard to associate this phenomenon to hydro-static pressure variations. Some more complex flow behavior seems to be at the source of this observation. One could for instance speculate that it is a combination of the relative change of AoA induced by effect of the waves on the flow and of the effect of the free surface proximity that causes the pressure variations observed.

Analysis of the pressure distribution is therefore not very conclusive and the analysis of the evolution of the lift in relation to the waves can yield a clearer relationship between waves and their influence on performances.

Q-criterion

The presence of waves has noticeably increased the size of the vortical structures. The wingtip vortices are hardly comparable to cases previously shown since the lift produced in the wave case is significantly larger and it has been demonstrated

before that wingtip structures are closely linked to the lift. However, the vortical structures created behind the strut are substantially larger in the wave simulation as can show the comparison between Figure 4.28 and Figure 4.21(b) showing a case at $V = 4$ m/s in calm water.

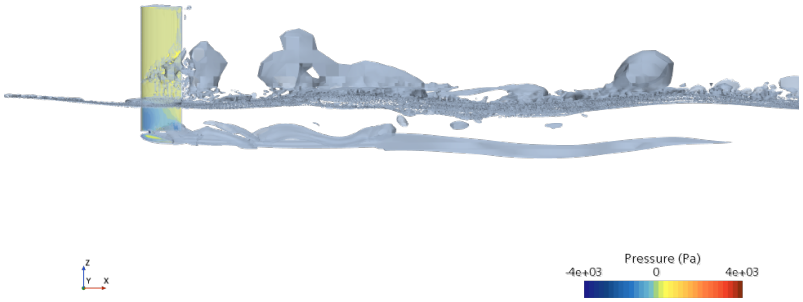

Figure 4.28: Side view of vortical structures (isovalue of $300/s^2$)

As for the pressure distribution in section 4.26, the Q-criterion isosurface is represented next to the water pattern at the same instant. The same moments have been chosen for the representation of the Q-criterion and the pressure distribution.

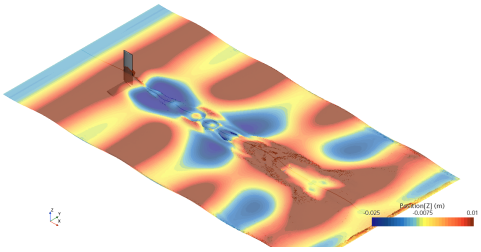

(a) t = 0.8575 s

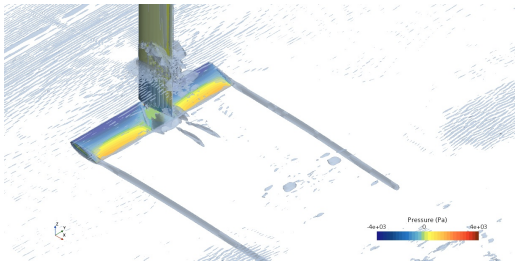

(b) t = 0.8575 s

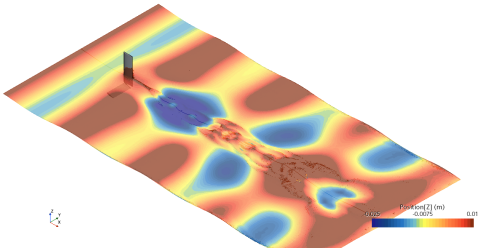

(c) t = 0.9275 s

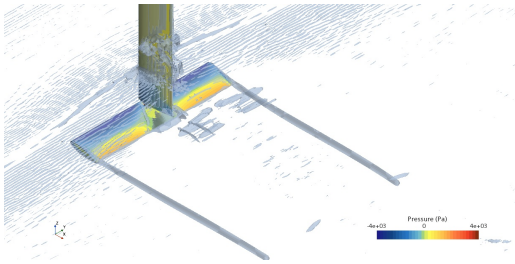

(d) t = 0.9275 s

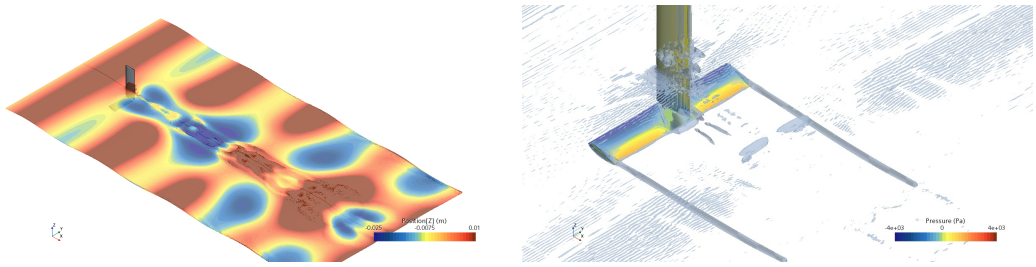

(e) t = 0.9975 s **(f)** t = 0.9975 s

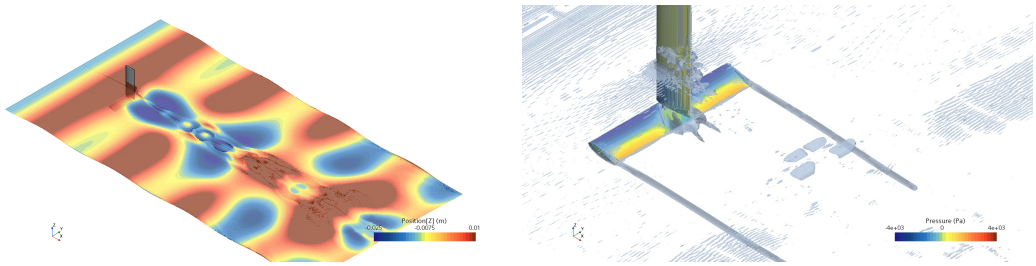

(g) t = 1.0425 s **(h)** t = 1.0425 s

Figure 4.29: Linking of the lift to the wave positions over a wave encountered period

Due to a high value set for the Q-criterion isovalue ($5000/s^2$) which is intended to get rid of the free surface structures, it is hard to distinguish the variations in the development of the vortical structures in Figure 4.29. However, by looking at animations of the Q-criterion isosurface one can observe a distinct variation of the structures near the strut and the wing certainly due to vortex shedding. The wingtip vortices remain however constant with the current representation and consequently, their evolution could not be traced back to the lift variations.

Evolution of the lift in relation to wave pattern

The analysis of the pressure distribution and the Q-criterion structures are not conclusive enough to explain lift and drag variations. Consequently, the lift is plotted over time and related to the position of the waves at the same instants as selected previously. For this analysis, the relation between lift and waves is done considering the yellow curve (wave pattern away from the wing and not in the wake of the wing (blue curve)) since the lift solution is a sinusoidal curve of the same period as the encountered waves.

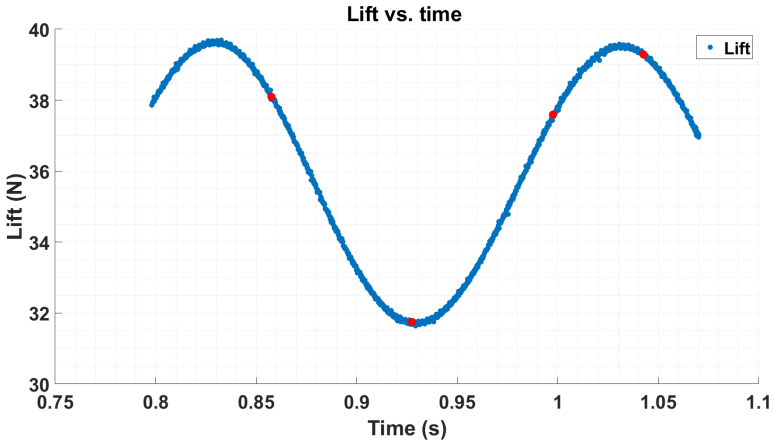

Figure 4.30: Plot of the lift against time for the simulation in waves

Figure 4.30 is then compared to the wave pattern plots from Figure 4.31. Figure 4.31(a) shows the wave crest being over the leading edge of the wing, at the same time the lift starts to decrease. Going slightly ahead in time, Figure 4.31(b) at t = 0.9275 s, the wave trough is about to reach the leading edge but the lift has already reached a minimum. The two last figures, Figures 4.31(c) and Figures 4.31(d), show a new wave crest approaching the leading edge. Again the lift variations are out phase with the encountered waves, the lift starting to increase before the water level rises.

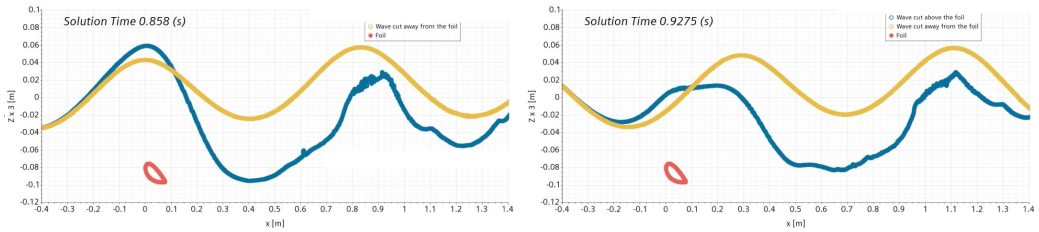

(a) t = 0.8575 s **(b)** t = 0.9275 s

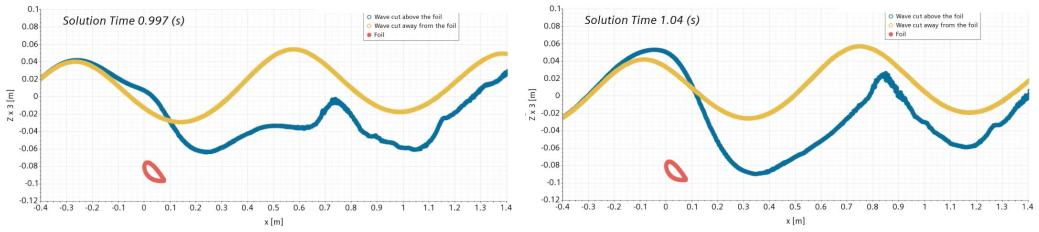

(c) t = 0.9975 s **(d)** t = 1.04 s

Figure 4.31: Position of waves at different instants within a wave encountered period

The series of figures of the wave patterns over time have demonstrated a difference in phase with the evolution of the lift. The lift reaches the maximum of its variation

before the wave crest reaches the wing and vice versa the lift attains a minimum before the wave trough reaches the leading edge of the wing. Such behavior could be explained by the way the flow behaves due to the presence of waves. Waves disturb the flow in such a way that the fluid elements adopt a circular path, an orbital trajectory. By looking at Figure 4.32, it can be observed that such circular motions introduce a component in the flow velocity that is not horizontal as the free stream is. This leads the wing to experience the encounter of the flow as if the wing had a different relative AoA to the flow since it is no longer solely moving in the x-direction. The circular trajectory extends beyond the wave crest, thus its effect is felt by the wing before the wave crest actually reaches the wing.

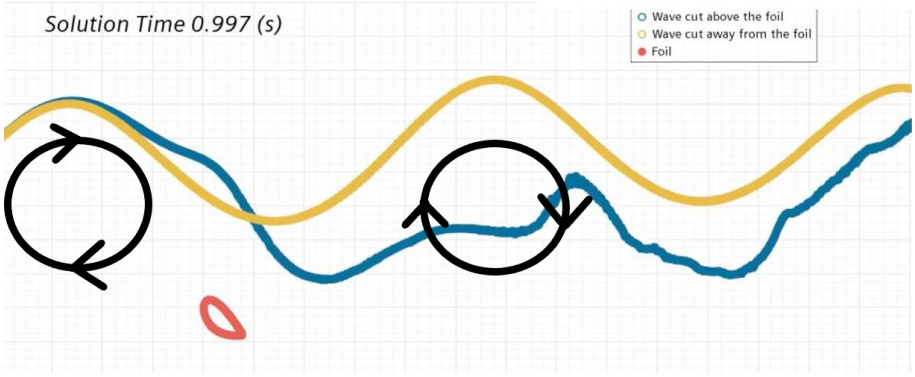

Figure 4.32: Representation of the orbital trajectory of fluid elements caused by waves

The effect of the circular motion of the fluid elements alone cannot explain the lift variations but the phase difference between wave and lift compared to the analysis of pressure distribution and vortical structures may suggest that it is a major contributor.

4.1.5 Additional simulations

The results from the calm water simulations raised some concerns. Primarily the lift observed in Figure 4.12 where lift measured for $V = 4$ m/s was lower than lift measured for $V = 2$ m/s at AoA $= 2^o$. Additional simulations have therefore been performed to investigate the impact of the strut and the t-joint (ID: 2.11).

Pressure distribution on wing without strut

The mesh and model conditions setup for these simulations are the same as in section 3.2.3 and are therefore not described here.

The motivation for computing simulations without strut is the observation of the lift produced by the wing at $V = 4$ m/s and AoA $= 2^o$ which is lower than for the same case at $V = 2$ m/s. This contradictory observation requires an explanation

as it is expected that higher velocities result in a higher lift. By looking at Figure 4.20(c) and 4.20(d), it is clear that the presence of the strut affects the pressure distribution of the suction side and deteriorates the lift. To confirm this hypothesis, the following simulations without strut have been carried out.

The comparison focuses on cases [d = 120 mm, AoA = 2^o, V = 4 m/s] with and without strut as these relates to the outstanding observation in Figure 4.41.

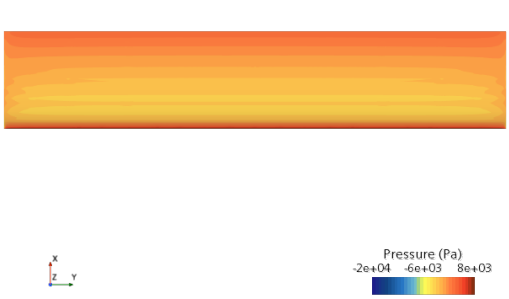

(a) Pressure side: without strut

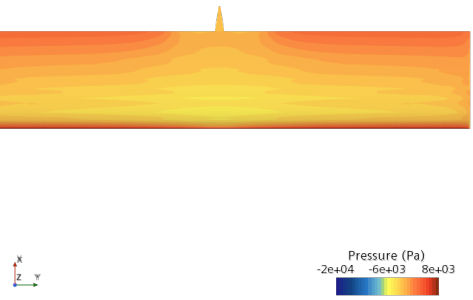

(b) Pressure side: with strut

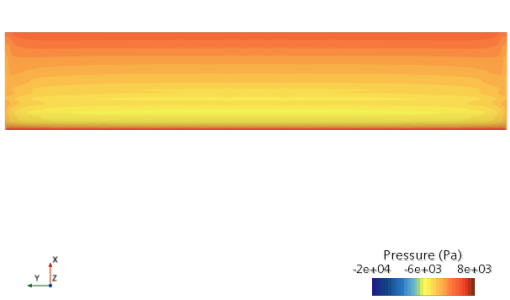

(c) Suction side: without strut

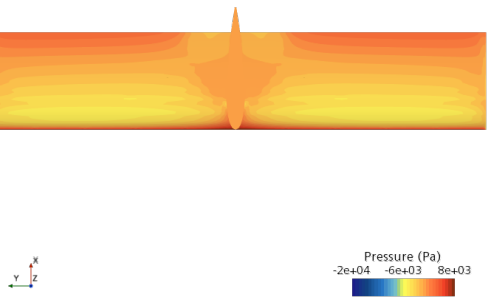

(d) Suction side: with strut

Figure 4.33: Pressure comparison between cases [d = 120 mm, AoA = 2^o, V = 4 m/s] with and without strut

The influence of the strut is put forward in Figure 4.33. The pressure distribution is affected both on the pressure and the suction side resulting in an increase of pressure

on the suction side and a decrease of pressure on the pressure side. This leads to a very important decrease in the lift as demonstrated in Figure 4.34. At $V = 4$ m/s, it is a shortfall of nearly 30 N of lift that is observed when the strut is present.

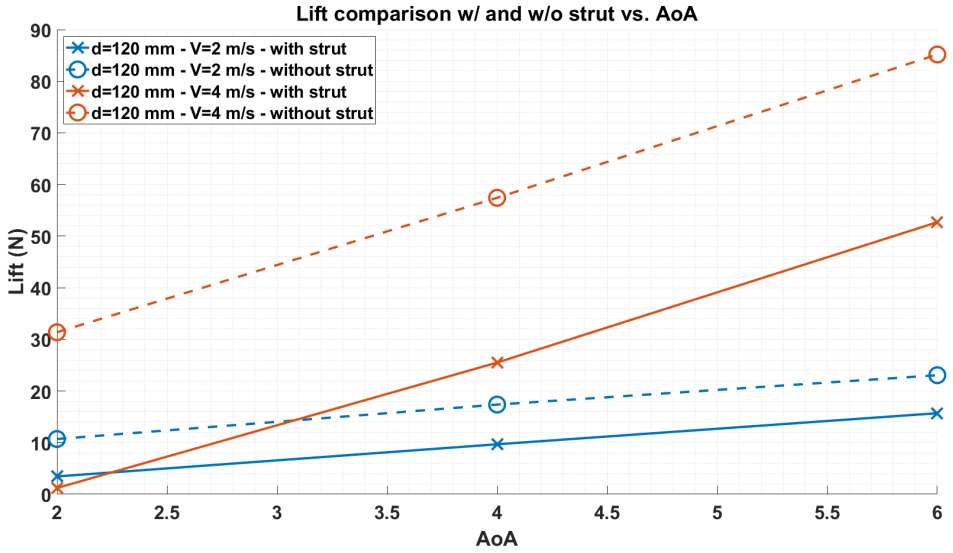

Figure 4.34: Lift vs AoA: comparison with and without strut for [$V = 4$ m/s, $d = 120$ mm]

The effect of the loss of lift is so important at $V = 4$ m/s that it makes it drop below the lift produced at $V = 2$ m/s. Due to a design flaw, the wing, therefore, becomes less efficient at higher speeds for small AoA. The investigation on the origin of lift deterioration is investigated further through the effect of the t-joint.

Effect of t-joint

It has been discussed how much the t-joint (ID: 2.11) connection influences the flow around the strut/wing area. Previously, it was observed that by removing the strut entirely, the lift was drastically improved. In this small study, the strut is kept at the same distance from the wing and only the t-joint is removed. Figure 4.35 shows how the flow is massively disturbed with the t-joint compared to without the t-joint.

Figure 4.36 shows the pressure distribution on the suction side between the same configurations with and without the t-joint. It can be observed that with the t-joint, the pressure is larger both at the contact point but also behind the t-joint. This increase in pressure is causing some decrease in lift as it is countering the lift created by the pressure on the pressure side of the wing.

Finally, the forces can be compared for the configurations with and without the t-joint. Figure 4.37 shows how almost no lift is achieved at $V = 4$ m/s with the t-joint. Without a t-joint, the lift rises to 30 N. As observed in the forces measured

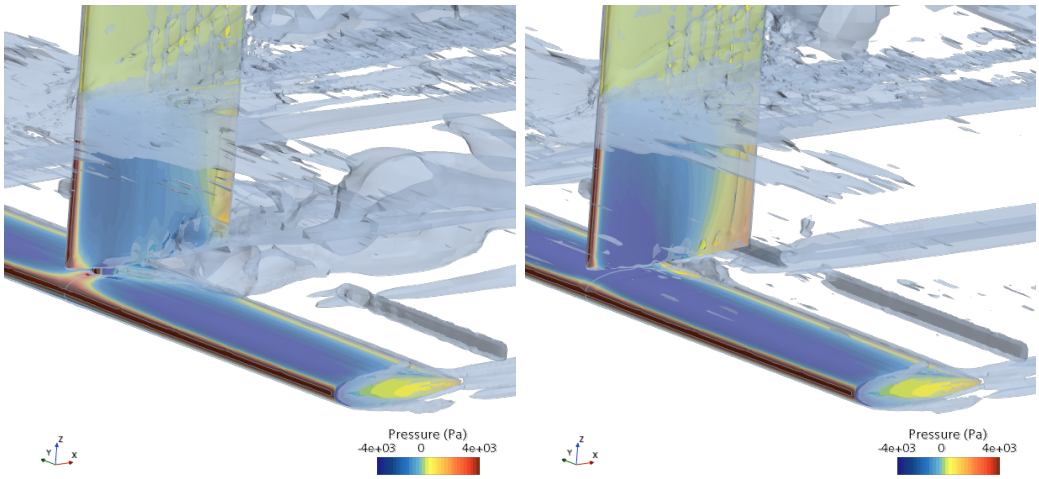

(a) With t-joint **(b)** Without t-joint

Figure 4.35: Q-criterion comparison with and without t-joint connection between strut and wing for [AoA $= 2^o$, $d = 80$ mm, $V = 4$ m/s]

without strut in Figure 4.34, the lift also rose by 30 N when removing the strut. The drag can also be observed in Figure 4.37. Naturally, the drag is increasing by having the t-joint present. This, therefore, concludes that the t-joint is massively impacting the lift performance in CFD simulations. The drag component is also influenced to some extent by the t-joint. This study reinforces the importance of small details regarding hydro-dynamic flow around all the components. To improve flow hence the forces, a more smooth joint connection can be designed.

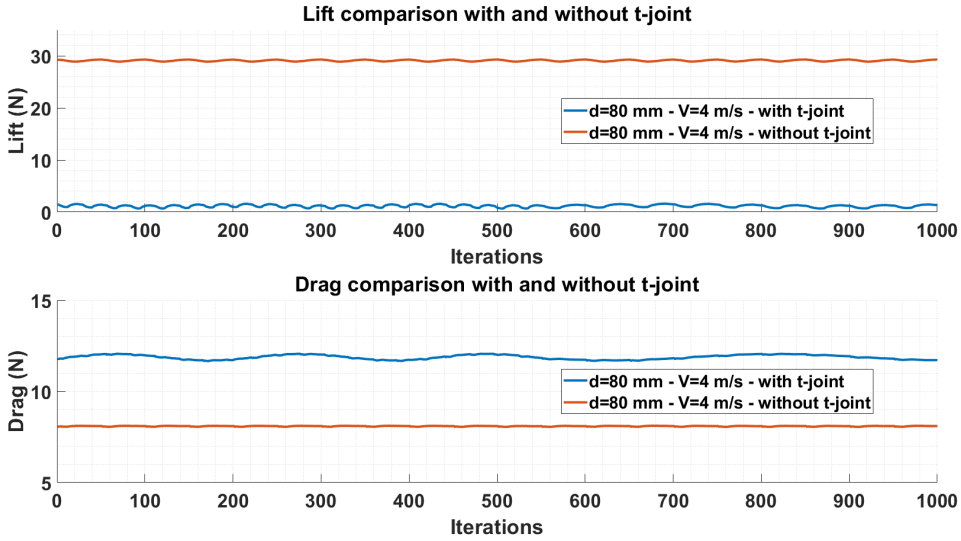

Figure 4.37: Lift and drag comparison with and without t-joint for [AoA $= 2^o$, $d = 80$ mm, $V = 4$ m/s]

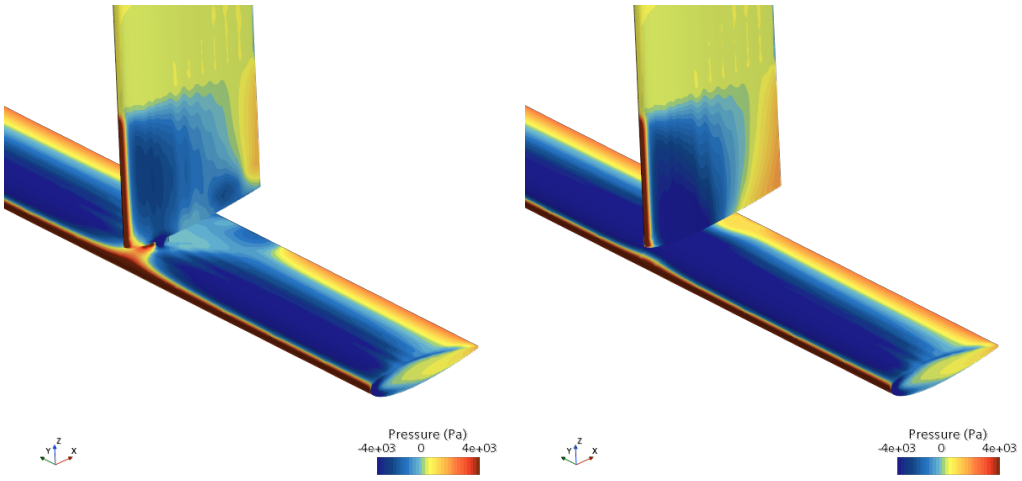

(a) With t-joint **(b)** Without t-joint

Figure 4.36: Pressure on suction side comparison with and without t-joint connection between strut and wing for [AoA $= 2^o$, $d = 80$ mm, $V = 4$ m/s]

4.2 Experimental results

As described in section 3.3, different experimental tests have been taking place. All tests have the common purpose of learning the hydro-dynamical behavior of the particular part in question. As this project is in its first iterative design phase, knowing each part's contribution is extremely valuable as it eases the process of improving the system in later design iterations.

4.2.1 Bare hull with rudder towing tank test

Figure 4.38 shows the resistance measurements of the bare hull at different speeds. The sample size is lower at higher speeds due to the run duration of the carriage. The sample size is large enough as the mean value is only used as guidance to estimate the resistance of the model itself. It can be seen that the amplitude for $V = 5$ m/s is very large compared to the other amplitudes of the other velocities. This is due to the model becoming very unstable being pulled at this velocity, thus resulting in swaying from side to side as it got pulled by the carriage. The amplitudes of the other velocities are small and are therefore good estimations of the model's resistance.

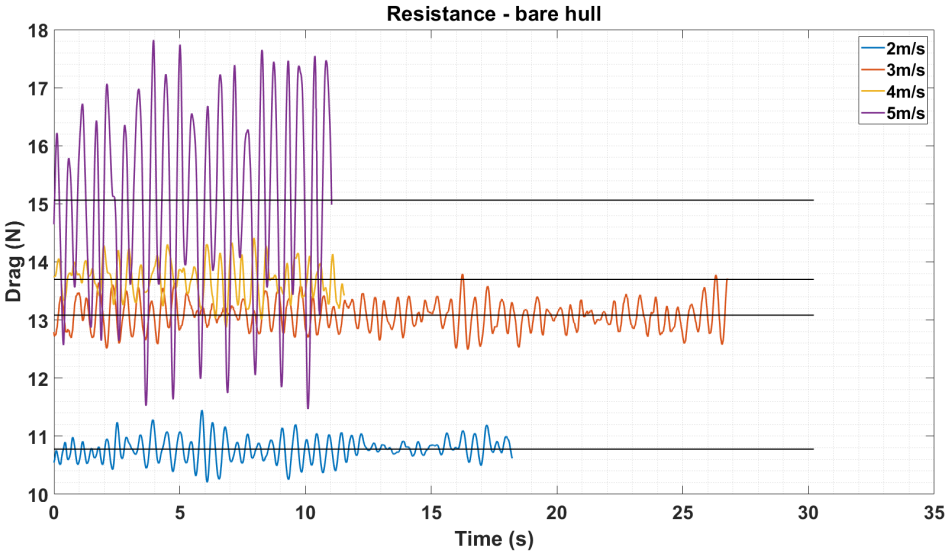

Figure 4.38: Resistance measurement and mean value of bare hull at different speeds

From the graphs in Figure 4.38, the mean resistance can be extracted for each velocity. This is summed up in Table 4.4. The difference in resistance from $V = 3$ m/s to $V = 4$ m/s is low compared to the other variations. This can be attributed to the fact that the hull was in a stable planning mode at those speeds wheres as at $V = 2$ m/s it was not yet planning and at $V = 5$ m/s had an unstable trajectory as stated above.

Table 4.4: Mean resistance from towing tank test at different velocities

Velocity (m/s)	Mean resistance (N)
2	10.77
3	13.08
4	13.70
5	15.06

Next, the rudder with the dual thruster setup from Figure 3.8(b) is attached to the bare hull. The depth of the rudder was approximately 280 mm. Figure 4.39 shows the resistance measurement at $V = 2$ m/s. As no speed increment was done, the sample size is 5062 measurements over 50 s. The mean resistance from the test is 35.73 N.

Figure 4.39: Resistance measurement and mean value of bare hull and rudder with dual thruster setup

It is possible to estimate the actual drag created by the rudder itself by subtracting the known resistance of the bare hull at $V = 2$ m/s shown in Table 4.4 from the mean resistance of the hull and the rudder.

$$R_{rudder,2m/s} = R_{hull+rudder,2m/s} - R_{hull,2m/s} = 35.73 \text{ N} - 10.77 \text{ N} = 24.96 \text{ N} \quad (4.1)$$

The drag created by the rudder and motors is therefore 24.96 N at $V = 2$ m/s. A large portion of this drag is created from the thruster themselves as the propellers were not turning, thus creating a "wall" blocking the water flow. This is of course not the case when self-propelling and this measurement can therefore be used as conservative guidance of the drag created by the rudder and thrusters.

4.2.2 Bollard pull test

Figure 4.40 shows the thrust measurements from the bollard pull test as described in section 3.3.2. The thrust curve shows inclination until the full throttle is achieved. Full throttle is held for roughly 5 s for the system to stabilize at a constant thrust which is achieved at around 45 N. The pulling is done for a very short duration to not overload the RC thrusters. Some propulsive efficiency can be lost when doing such tests due to heat, friction, and tension[2].

[2]https://www.marineinsight.com/naval-architecture/bollard-pull-everything-you-wanted-to-know/

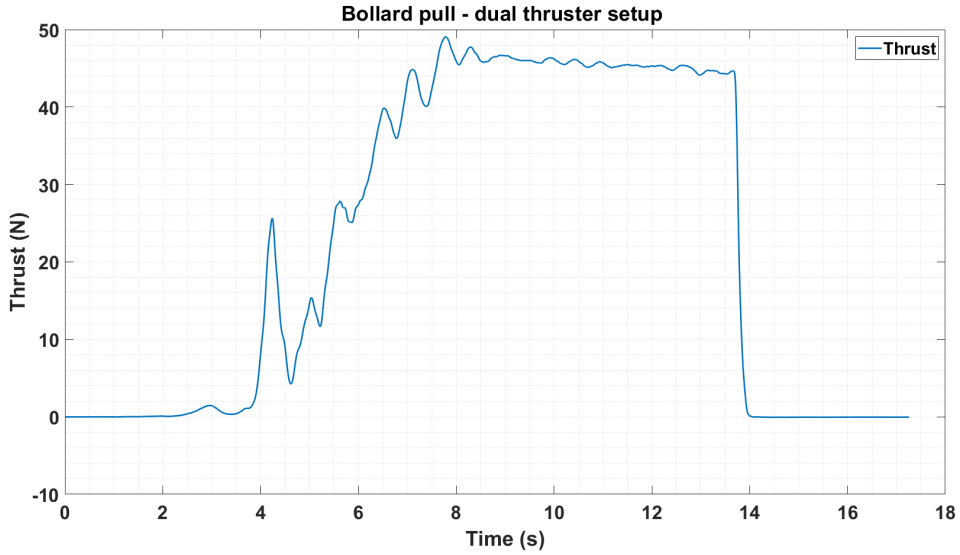

Figure 4.40: Bollard pull thrust measurement of dual thruster setup

The thrust achieved in the bollard pull test is an indicator of what resistance can be overcome. It is therefore noticeable that the thrust is converging at 45 N as the measured resistance of the hull and the rudder from section 4.2.1 resulted in a total resistance of 35.73 N meaning that by only installing the rudder system to the model, the free-running model should be able to reach a velocity just over $V = 2$ m/s. This is of course not optimal as the front wings drag is also to be added as it will be shown in section 4.2.3.

4.2.3 Front wing towing tank test

A series of 12 runs in calm water and two runs in waves were performed at SSPA's towing tank allowing for the test of 38 configurations (see section 3.3.3 about the course of the tests). The data collected from calm water tests are then processed to obtain the mean value of the forces over each test case.

Lift forces in calm water

Table I.1 shows the mean value of the lift created by a single front wing at different AoA and at two different depths. The values from Table I.1 are then plotted in Figure 4.41 for easier comparison.

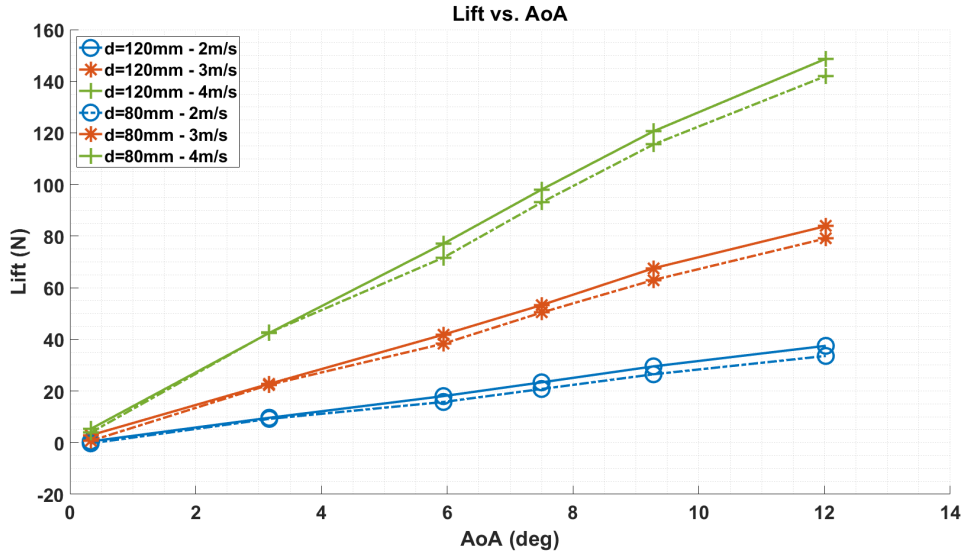

Figure 4.41: Lift from single front wing with strut

From Figure 4.41, it is observed that the wing is generating less lift closer to the water surface at every velocity. Another noticeable behavior is when comparing to the GOE460 characteristics from Figure B.1(a) where stalling occurs at 10^o for Re = 200,000. All curves change their slopes to some extent but do not seem to stall. As the speed is increased when testing, so is the Reynolds number, hence the test is run for $Re = [160,000,\ 240,000,\ 320,000]$ for $V = [2,\ 3,\ 4]$ m/s respectively. A consequence of running at different Reynolds numbers is the change in behavior of the foil which can cause the stall angle to occur sooner or later than expected. We can check the lift coefficients by using Eq. 2.1 and inserting the obtained lift. This is done in Table I.2 and plotted for better comparison in Figure 4.42.

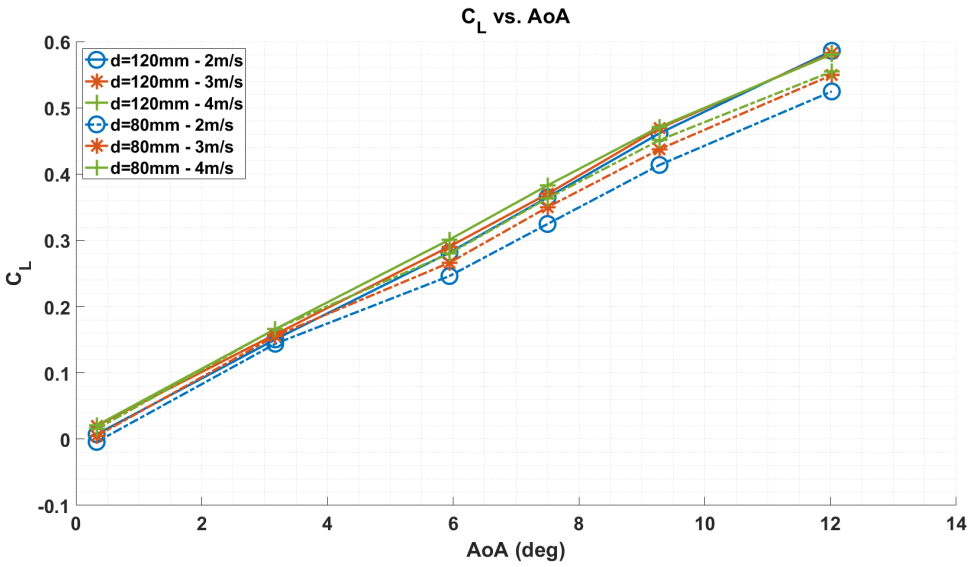

Figure 4.42: Calculated C_L based on lift from towing tank tests

Several things are noticeable when inspecting the calculated lift coefficients. First, they all follow the same pattern with very small deviations. Second, $C_L \approx 0$ at 0^o AoA as expected for symmetric profile behavior. Third, the stall angle at 10^o AoA is still not present as expected from GOE460 characteristics from Figure B.1(a). Fourth, the upper limit of the lift coefficients is between $0.55 - 0.59$ which deviates from the theoretical 2D value of $C_L \approx 1.1$ as shown in Figure B.1(a).

Drag forces in calm water

Next, the same analysis as for the lift forces can be done for the drag forces measured on the wing. Table I.3 summarizes the drag forces measured during the towing tests of the front wing. For better comparison, the values are plotted in Figure 4.43.

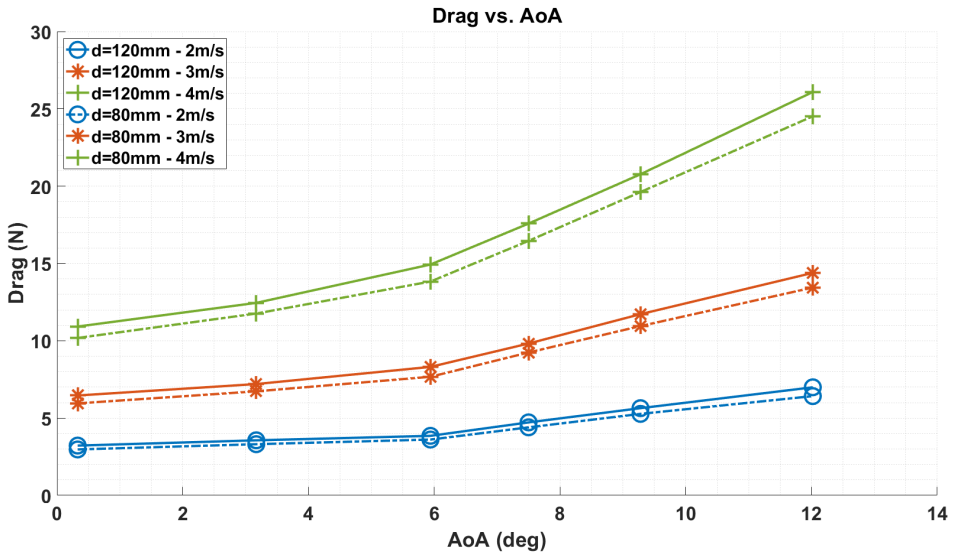

Figure 4.43: Drag from single front wing with strut

Figure 4.43 shows several interesting behaviors. First, the drag forces are grouped by velocities as expected. The deeper test setup results in larger drag forces in all three groupings meaning that there is a water surface effect on the drag. Second, the drag forces seem to make a slope change at 6^o AoA. According to the drag coefficient from Figure B.1(b), the drag coefficient should increase linearly up until 10^o for Re = 200,000. the behavior is likely to be different at different Reynolds numbers as it was noticed for the lift forces. Using Eq. 2.2, the actual drag coefficients can be estimated by inserting the measured drag and isolating it for C_D. This is summarized in Table I.4 and plotted in Figure 4.44.

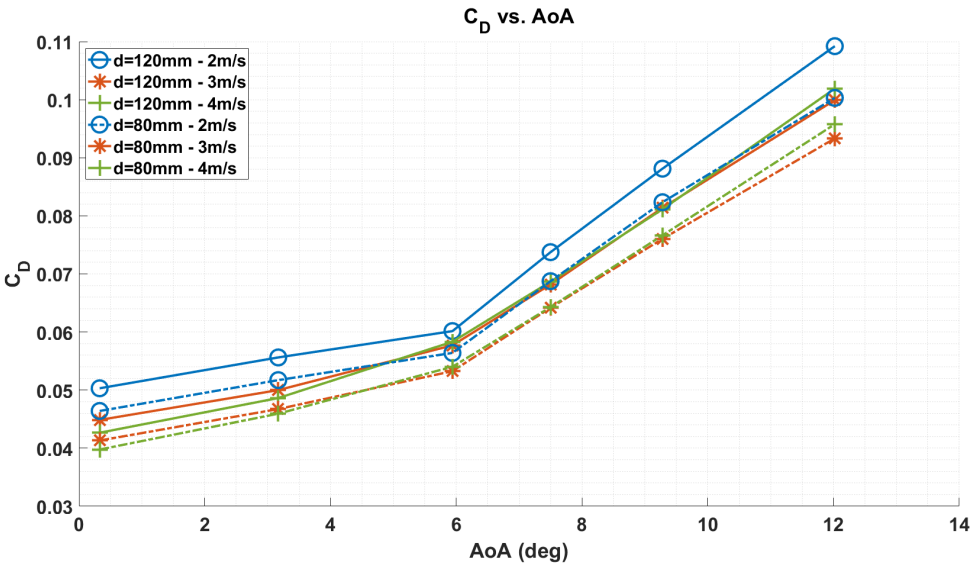

Figure 4.44: Calculated C_D based on drag from towing tank tests

Looking at the curves in Figure 4.44, several noticeable behaviors are observed. First, as for the measured drag at 6^o, the slope change is even more evident. Second, comparing the coefficients to the ones in Figure B.1(b), the drag coefficients should vary between $0.013 - 0.025$ whereas the calculated drag coefficients vary between $0.04 - 0.1$, thus four times as high drag coefficient. An obvious difference between the calculated drag coefficients and the theoretical drag coefficients is the presence of the entire strut, the steel connection between strut and wing (ID: 2.11 in Figure 3.5), and the pushrod connection. All of these parts induce drag resulting in larger measured drag forces and hence larger drag coefficients.

Lift and drag forces in waves

As described in section 3.3.3, the front wing was tested in waves with a single configuration consisting of $d = 80$ mm, AoA $= 12.02^o$ and $V = 3$ m/s. This configuration was run twice. The data should match each other but this is unfortunately not the case.

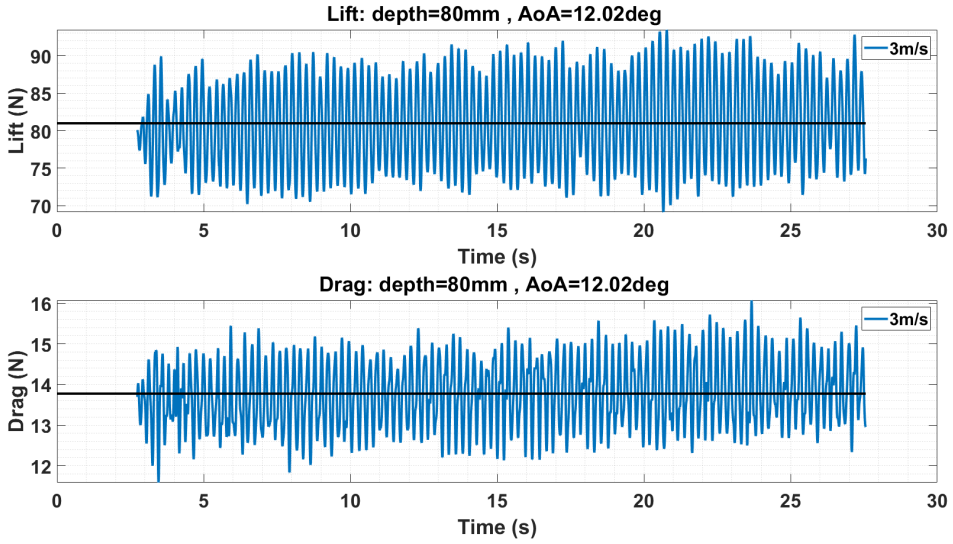

Figure 4.45: Towing tank test measurements of front wing and strut in waves - First run

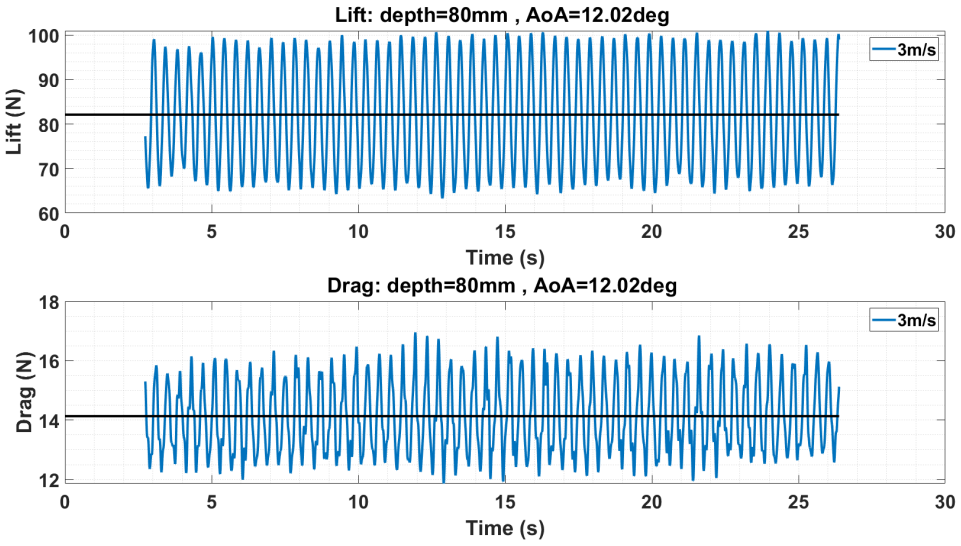

Figure 4.46: Towing tank test measurements of front wing and strut in waves - Second run

Figure 4.45 shows inconsistency in the measurements as the amplitude is constantly varying. For the second run, Figure 4.46 shows a more clear and constant amplitude. It is not clear what caused the different results between the two test runs but one can postulate that the harmonics observed in the first run are due to pollution caused by the first waves generated during calibration. It is interesting to analyze the sensitivity to the waves i.e. comparing the second run with the same configuration as in calm water. This is done in section 5.1.2.

Wave period determination

No sensors were available during the tests to measure the period of the waves generated and therefore it needed to be determined by post-processing the data acquired. This is done by analyzing the second run in waves as it is the most regular one (see Figure 4.46).

The speed of the carriage ($V = 3$ m/s for the wave run) and the wavelength of the waves are known (1000 mm). Thus, by measuring the period of the lift and drag oscillations one can determine the period of the encountered waves. This is done by employing wave and seakeeping theory that provides the following equation (Janson, 2015) valid in deep water:

$$\omega_e = \omega - \frac{\omega^2 U}{g} cos(\mu) \tag{4.2}$$

Where:

- ω_e is the measured pulsation of the encountered waves
- ω is the wave pulsation
- U is the foil velocity
- g is the gravitational acceleration
- μ is the heading angle relative to wave direction+

The measured pulsation is determined from the period of the forces oscillation. The inputs to solve Eq. 4.2 are summed up in Table 4.5.

Table 4.5: Inputs for determining encountered wave period

Variable	Value
ω_e	15.71 rad/s
U	3 m/s
μ	180^o
g	9.81 m/s^2

The result is a wave frequency $f_{wave} = 1.37$ Hz.

Dynamic effects

The effect of waves gives rise to important variations of the loads around the mean that are called dynamic loads. These are important components to consider when designing the structure but are unfortunately difficult to estimate before tests. For this reason, a safety factor of three was applied when dimensioning the structure to make up for this lack of knowledge. The data acquired during the tests can now be used to estimate the dynamic effects more accurately. The data from the second run is used as it is more regular than for the first run as it can be observed from

Figures 4.45 and 4.46.

To do so, an average of the maximums and the minimums for both lift and drag is calculated. The results obtained are shown in Table 4.6 and Table 4.7.

Table 4.6: Dynamic effects on lift due to waves and comparison to calm water lift

	Value (in N)	Percentage of the mean lift in waves	Percentage of the mean lift in calm water
Average lift in calm water	79.11	96.3%	-
Average lift in waves	82.11	-	104.8%
Average of the minimums in waves	65.95	80.3%	83.4%
Average of the maximums in waves	99	120.6%	125.13%

The results show a higher mean lift force in waves than in calm water. The lift force in waves varies about 20 % around the mean and can vary as high as 25 % above the mean lift in calm water. The safety factor of three applied was therefore much more than required to account for dynamic loads.

Table 4.7: Dynamic effects on drag due to waves and comparison to calm water drag

	Value (in N)	Percentage of the mean drag in waves	Percentage of the mean drag in calm water
Average drag in calm water	13.44	95.1%	-
Average drag in waves	14.13	-	105.1%
Average of the minimums in waves	12.47	88.25%	92.8%
Average of the maximums in waves	16	113.3%	119.1%

Similar to the lift, the mean drag measured in waves was slightly higher than for calm water (5 %). On the other hand, the variations represented about 13 % of the mean drag in waves and were about 20 % higher than the mean drag in calm water.

Sonar study

The measurements realized with the sonar revealed a relatively low precision (precision to the centimeter). The graph in Figure 4.47 shows a recording of heights measured by the sonar in calm water.

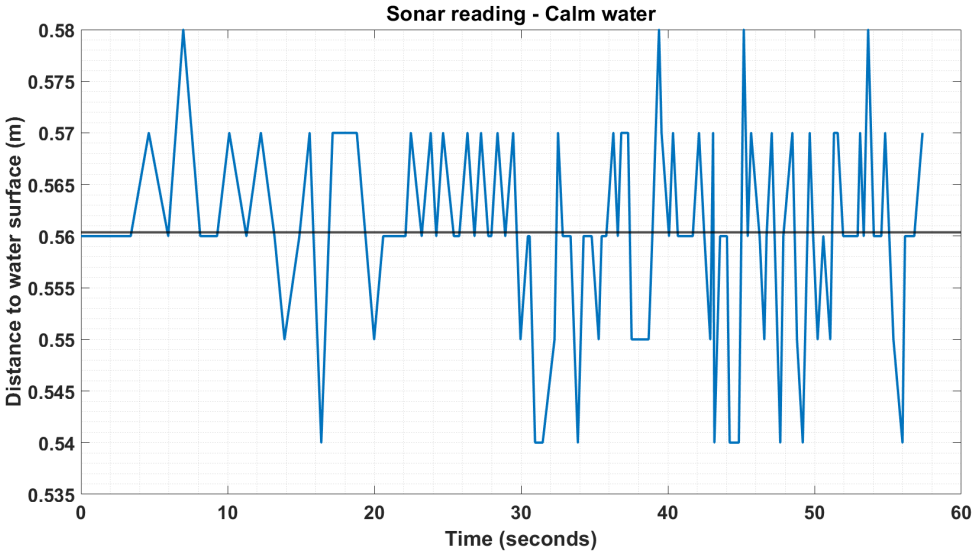

Figure 4.47: Sonar study in calm water : Height vs Time

Even though the average height measured does correspond to the distance between the sonar and the water surface, it can be observed that some measurements are 20 mm off at times, even if the surface is supposed to be flat. The variance is between $0.54 - 0.58$ m. The calm water reading of the sonar, therefore, indicates that there is a big uncertainty with the JSN-SR04T sonar sensor.

Next, the JSN-SR04T sonar was tested with wave conditions. As described in section 3.3.3, the amplitude of the waves was 25 mm, meaning that this should be recorded by the sonar. Figure 4.48 shows the measurements done by the sonar sensor in two different wave runs. The first one ran for 375 s and the other run for 85 s.

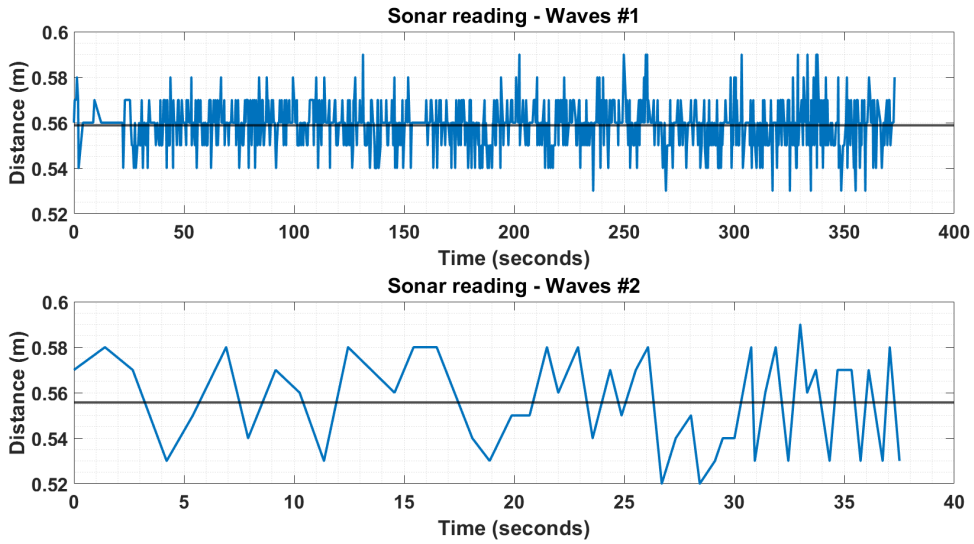

Figure 4.48: Sonar study in waves : Height vs Time

From Figure 4.48, we see that the sonar does read a variance between $0.52 - 0.59$ m, thus it is observing more movement than the calm water reading. It is indecisive that the sonar is a useful sensor tool for this purpose as no clear data is showing that the sonar reads the waves well enough. This can be due to the frequency that the trigger pulses are sent out or the sampling frequency to make the log. As the waves are incoming at somewhat high speeds, the sonar cannot keep up with reading the constant change in water level height. Another issue with sonar sensors is that they send out trigger pulses in a cone form meaning that the sound waves received back are likely to be an average of different positions of the wave thus different vertical positions of the wave are being read by the echo part of the sonar. A solution to this could be a sonar sweeping a much more precise area of the water surface.

4.2.4 Field test

The field test of the model is described in section 3.3.4. Maneuvering tests of the manual flight mode and the stabilize flight mode were performed.

Manual flight mode

First, the manual flight mode is tested. In this mode, the model is fully controlled by the operator. The velocity as a function of the throttle pulsations is plotted in Figure 4.49.

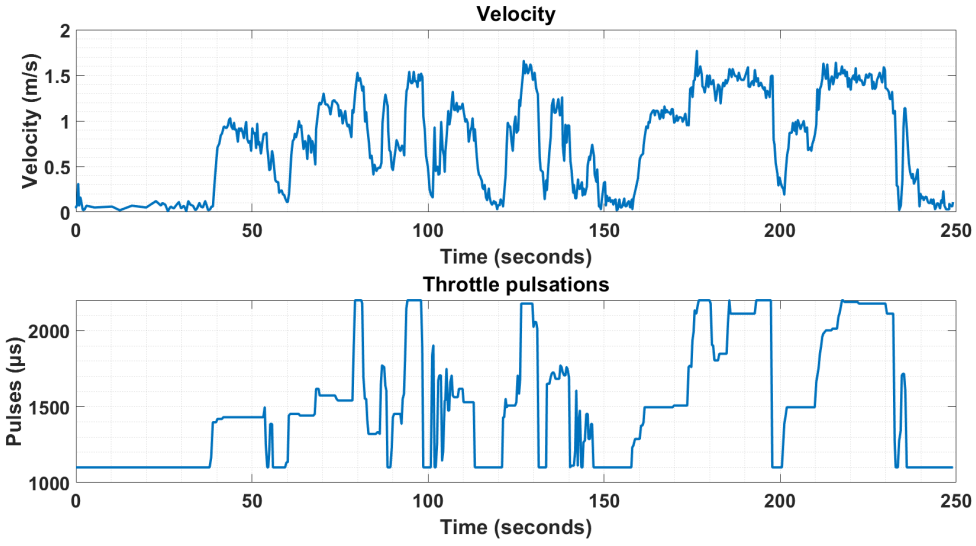

Figure 4.49: Velocity vs. throttle pulsations - Manual flight mode

There is a clear correlation between giving more throttle and obtaining higher speeds. From the test, it is clear that the maximum reached speed is just over 1.6 m/s when applying maximum throttle. This speed does not allow the model to have lift-off as the planned take-off speed is around 2.5 m/s. The planned recordings of the model's

behavior included heave, roll, and pitch as these are the motions controlled by the wings. Due to not reaching the desired speed, heave is therefore not measurable. The focus will therefore be on pitch and roll. This is plotted in Figure 4.50.

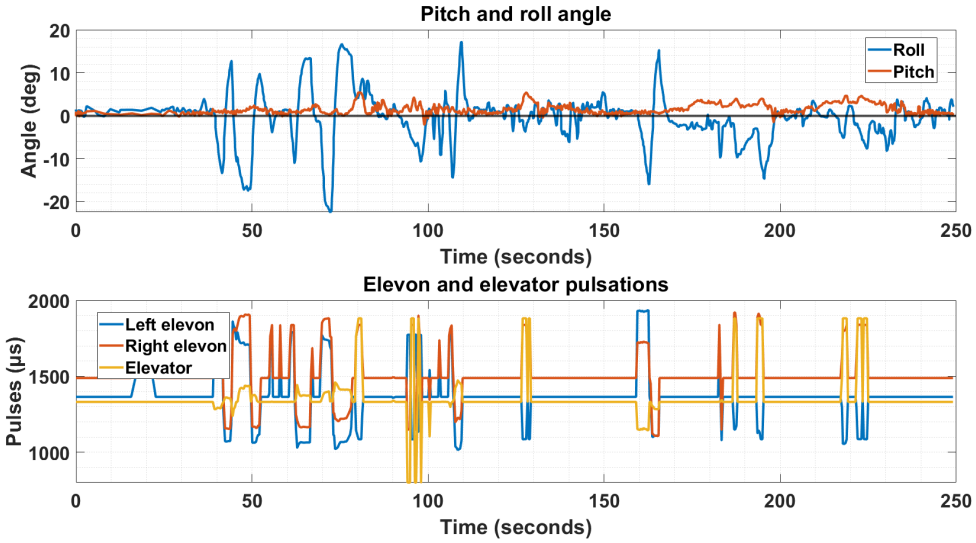

Figure 4.50: Pitch and roll motions vs. elevons and elevator pulsations - Manual flight mode

The parameters servo02_reversed = 1 and servo06_reversed = 1 while servo05 _reversed = 0. This is due to the orientation in the servos being installed. The result of these parameters is that the servo will move the wings down when the joystick is pitching down. When plotting the pulsations of the elevons and the elevator, it can be observed that sometimes, the pulses are inverted to each other e.g. 80 s mark where there is a big positive spike for the elevator and right elevon whereas the left elevon is moving opposite. At this moment in time, the GPS senses an up-going pitch moment as it can be seen in the top plot. So even though the pulses seem very different, the movement of the wings is identical. When the elevator curve is not changing but the elevon curves are, this means that the model is rolling. This can for example be observed in the interval $50 - 70$ s where the elevon pulsations are changing several times meanwhile the roll motion of the model is doing the same. The motions of the model are therefore correlated to the control system.

Stabilize flight mode

As for the manual flight mode, the obtained speed of the model is recorded and visualized vs. the throttle pulsations.

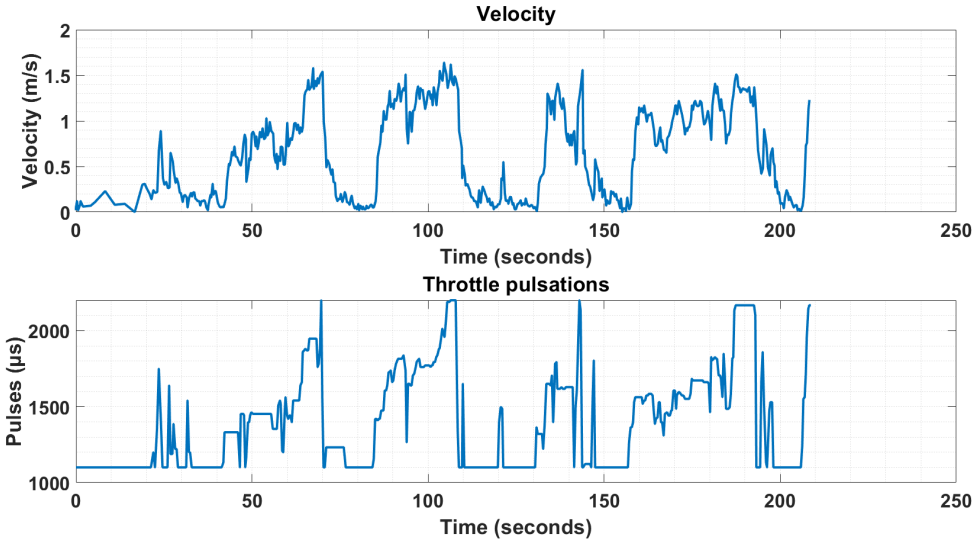

Figure 4.51: Velocity vs. throttle pulsations - Stabilize flight mode

Somewhat the same velocities are observed in the stabilize flight mode compared to the manual flight mode. This is also what is expected as the stabilize flight mode does not temper with the throttle input. The roll and pitch motions are tempered when operating in stabilize flight mode. This is visualized in Figure 4.52.

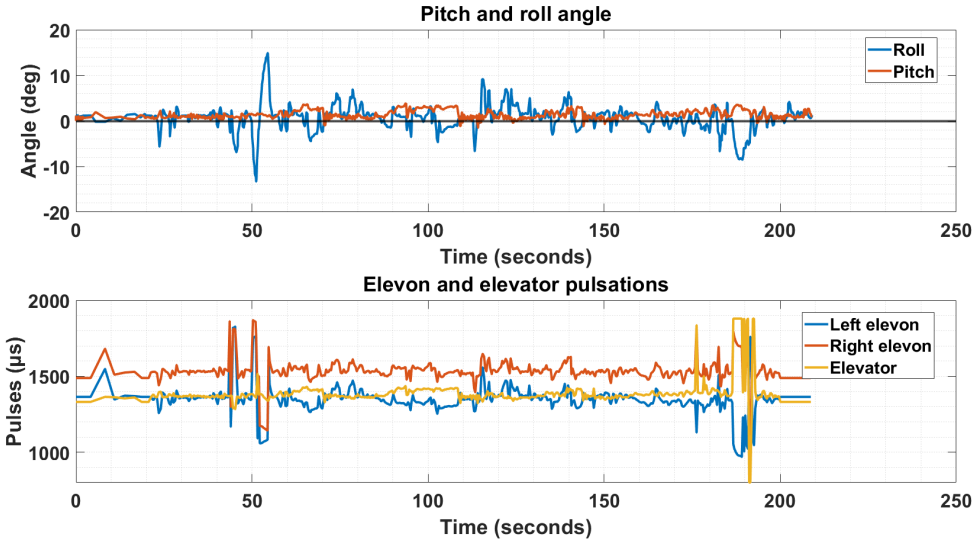

Figure 4.52: Pitch and roll motions vs. elevons and elevator pulsations - Stabilize flight mode

When in stabilize flight mode, it is possible to give input on the roll and pitch stick. This can be observed around the 50 s and 180 s marks. In the interval between these spikes, the model is purely maneuvered with the throttle and yaw joystick. When turning the model, the actuators constantly tries to self stabilize. This can be seen by the micro-adjustments visualized by the many small spikes in the pulsation plot.

As a result of this, the motions are much more close to the 0^o mark at all times. The test is of course only conducted in displacement mode as the model did not obtain lift-off but the concept will be the same in foilborne mode. It should be noted that the offset of the right and left elevons is due to the transmitter signals. The transmitter needs further re-calibration to send out the same amount of pulses on each channel hence the elevons will match each other. This can be done in Mission Planner.

4.2.5 Workshop inclining test

As mentioned in section 3.3.5, an inclining test was performed in the workshop. The purpose of this test is to validate the results from the field test with the stabilize flight mode on. The measurement of the roll and pitch is plotted against the pulsations of the elevons and wings in Figure 4.53 and Figure 4.54 for roll test and pitch test respectively.

Figure 4.53 shows how the elevator only makes a small adjustment to the pitch which varies between $0 - 3^o$. The reason for this small deviation is that the GPS is calibrated on the workbench and by placing it in the model, the natural pitch of the model is causing this deviation. It is possible in Mission Planner to zero out the new position of the GPS to avoid such a small deviation. The elevons make the appropriate changes as the roll angle is done manually in the workshop, hence they are fully responsive to the roll motion occurring.

Figure 4.54 shows the pitch inclining test. Here it can be observed that when pitching, the elevator and right elevon sends pulse signals inverted compared to the left elevon. As mentioned in section 4.2.4, this is due to the orientation of the servo installation. The servo pulsations are reversed to obtain the same physical handling of the actuator. It can then be seen that the servos once again are fully responsive to the manual pitch inclination.

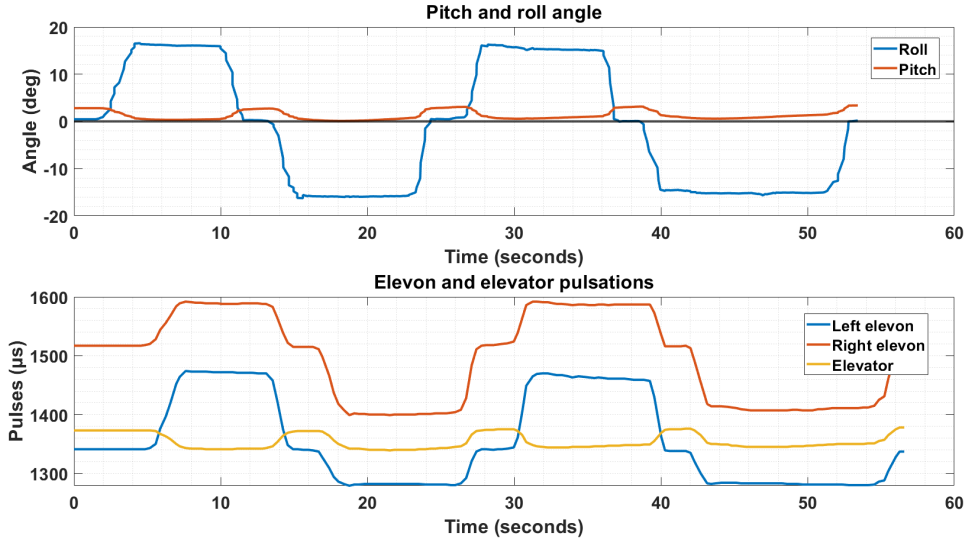

Figure 4.53: Pitch and roll motions vs. elevons and elevator pulsations - Workshop roll inclining test using the stabilize flight mode

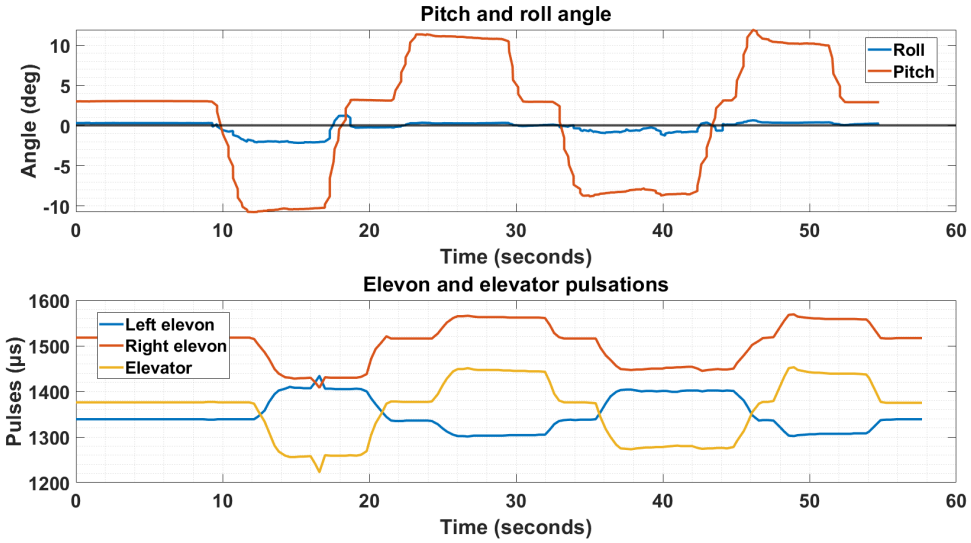

Figure 4.54: Pitch and roll motions vs. elevons and elevator pulsations - Workshop pitch inclining test using the stabilize flight mode

5
Discussion

The results gathered throughout the project give rise to questioning and analysis of subjects that require connecting several parts of the thesis to make the most of it. Thus, a broader vision has to be adopted upon which will be built a global discussion concerning the validity of the results, unexpected observations, and suggestions on improvements to make.

5.1 Comparison of CFD and experimental results

Section 4.1.3 and section 4.2.3 presented the results of the CFD simulations and the results of the front wing towing tank test respectively. The geometries of the wing and strut in the CFD simulations are not identical to the manufactured modules due to imperfections in the 3D printing of the modules and due to simplification made to the geometry in CFD simulations to reduce the computational effort. Therefore the simulations try to represent the tests but a compromise had to be made on the complexity of the geometries modeled in Star CCM+.

5.1.1 Calm water

The CFD simulations and the towing tank tests are performed with different AoA ranges. A common AoA for both methods is AoA = 6^o. It is therefore natural to compare the results from both methods at this AoA. The forces and the coefficients compared between the methods are shown in Figures 5.1 - 5.4.

Significant differences in the results between experiments and CFD can be observed. In the following paragraphs, the percentages of deviation between the two investigations will be compared taking EFD's real experimental results as a reference. The lift curves in Figure 5.1 show a large deviation of 28.16 and 31.62 % for $d = 80$ mm and $d = 120$ mm respectively at $V = 4$ m/s. The deviation is 6.67 and 12.88 % for $V = 2$ m/s for $d = 80$ mm and $d = 120$ mm respectively. The same deviations can be observed when comparing for C_D as done in Figure 5.2. Here, it can be observed that the tendency of the CFD results is a decrease in C_L with increasing velocity. For the experimental results, this tendency is inverse. Figure B.1(a) shows how C_L is decreasing at higher Reynolds numbers thus the CFD results correlate with the theoretical tendency.

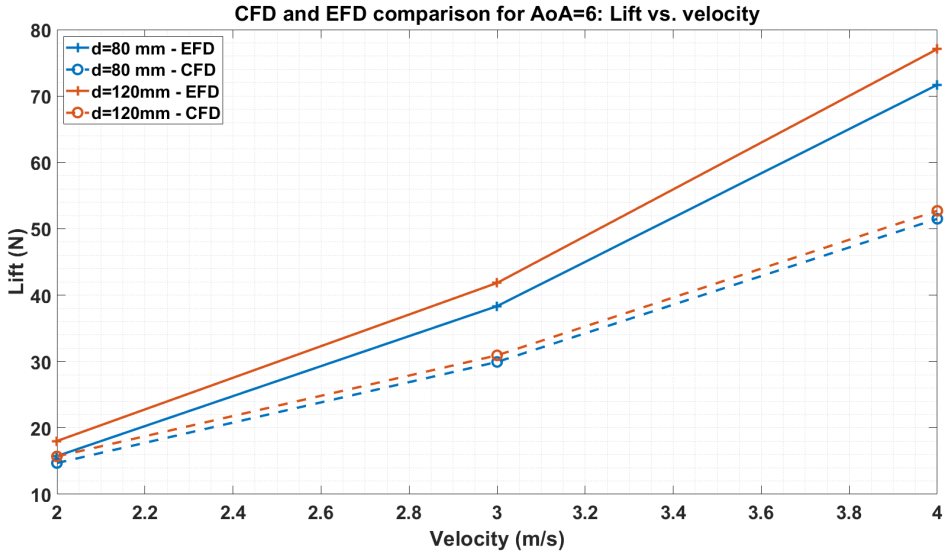

Figure 5.1: Lift comparison between CFD and towing tank test results for AoA = 6^o, $d = [80, 120]$ mm and $V = [2, 3, 4]$ m/s

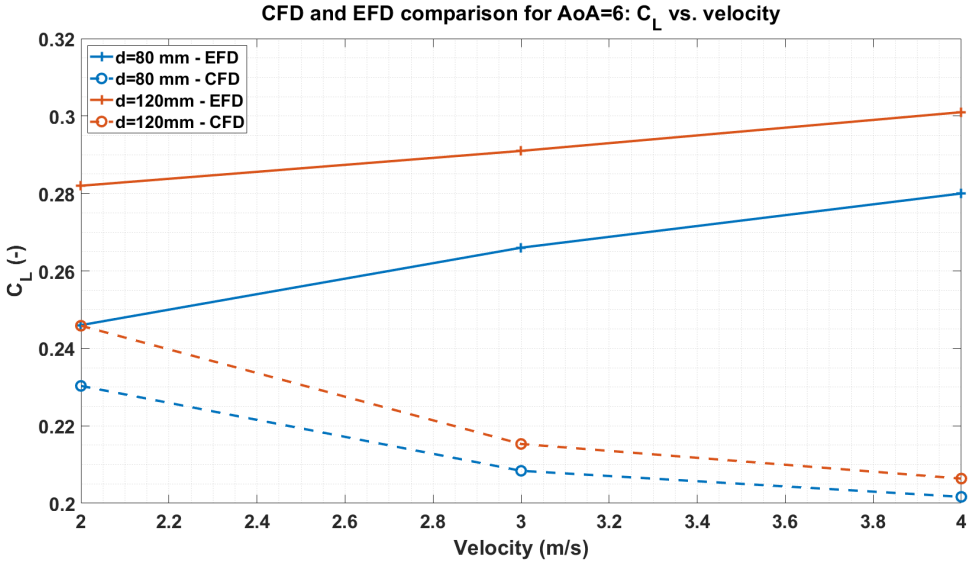

Figure 5.2: C_L comparison between CFD and towing tank test results for AoA = 6^o, $d = [80, 120]$ mm and $V = [2, 3, 4]$ m/s

Looking at the drag forces in Figure 5.3, both methods result in a natural increasing drag as a function of velocity. The deviations between the methods are 6.1 - 7.3 % (from EFD to CFD) at $V = 2$ m/s for $d = 80$ mm and $d = 120$ mm respectively. At $V = 4$ m/s, the deviations are 3.6 - 4.6 % for $d = 120$ mm and $d = 80$ mm respectively. The drag forces are therefore much more comparable than the lift forces between the two methods. The same deviations can be seen for C_D in Figure 5.4. Here, the tendency for C_D is decreasing as the velocity increases for both methods. Comparing with the theoretical tendency in Figure B.1(b), C_D is decreasing at

higher Reynolds number.

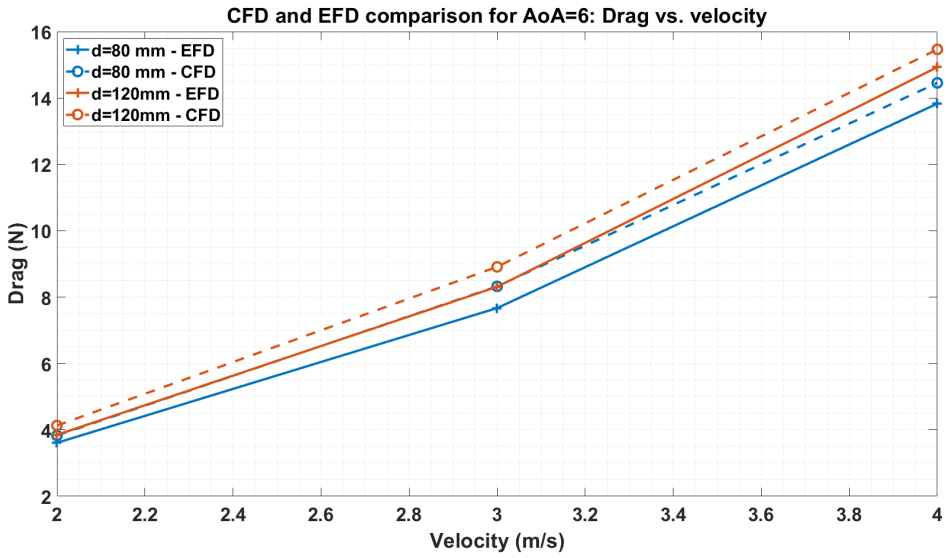

Figure 5.3: Drag comparison between CFD and towing tank test results for AoA = 6^o, $d = [80, 120]$ mm and $V = [2, 3, 4]$ m/s

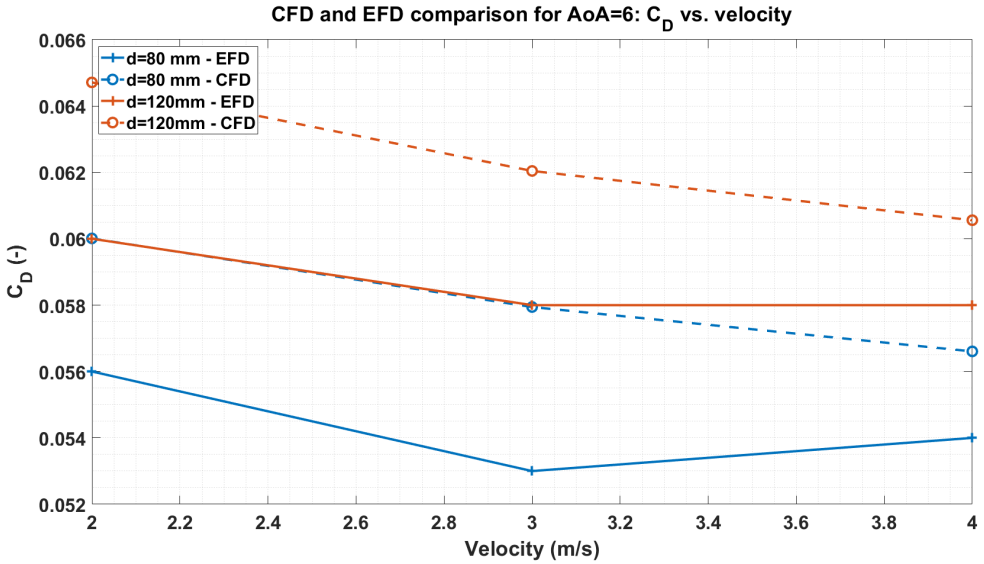

Figure 5.4: C_D comparison between CFD and towing tank test results for AoA = 6^o, $d = [80, 120]$ mm and $V = [2, 3, 4]$ m/s

Since the deviations at times can be large (e.g. 31.6 % for the lift at 120 mm at 4 m/s) and there is no constant correlation between the results and the theoretical tendencies in Figure B.1. It is clear that errors are located in the methods (either one or both). As both methods require advanced setup procedures, it is unclear where the errors have been made. The major uncertainty lies in the conversion

method to obtain the AoA measured during testing at SSPA. One of the main arguments that can be put forward is the behavior of the lift observed in CFD studies that showed an enormous deterioration of the lift due to the presence of the t-joint (see section 4.1.5 and Figure 4.12). This questions the validity of the hypothesis on which is based the conversion which is that for AoA = 0^o the lift should be 0 N. Other sources of uncertainties are touched on in section 5.1.3.

5.1.2 Sensitivity to waves

Figure 5.5 compares the lift and drag forces measured during experimental testing at SSPA on the wing for an identical configuration with waves and in calm water. As expected, the amplitude of the forces is much larger for wave operation than in calm water. The lift variance in waves is roughly 35 N whereas, in calm water, it is 5 N. The drag variance in waves is 5 N and in calm water it is 2 N. This can be partially explained by the effect of the surface on the wing. As it gets closer to the water surface, the lift and drag diminish. When the wing is far away from the water surface, the lift and drag increase. Then the motion of the fluid particles caused by the waves have also to be accounted for. The orbital trajectory of the fluid particles result in a change of AoA relatively to the flow which contributes to make the lift and drag vary. The resulting mean lift is 4.8 % larger in waves compared to calm water and the mean drag is 5.1 % larger in waves compared to calm water (see the comparison of the results between calm water and waves tests in Table 4.6 and Table 4.7). It is therefore interesting to compare the lift to drag ratio as it shows the efficiency of the wing in the different conditions. In wave condition, the lift/drag ratio is 5.89 and in calm water condition, it is 5.81. One cannot assess with certainty that efficiency is better in calm water as this result shows a very small difference while the uncertainties are considerable and the data set is too small to be conclusive.

Table 5.1 compares the mean forces and the variations for EFD and CFD. For EFD, the lift variations are $\pm 20 - 21$ % while for CFD, it is $\pm 11 - 12$ %. For drag, the methods have similar variations ($\pm 6 - 8$ %) from their respective means. The forces themselves have large deviations in between the methods (13.4 % for lift and 10.1 % for drag). The geometrical differences between the simulations and the manufactured wing are major concerns when comparing the obtained forces. The differences between the simulated and experimental waves are also debatable as the characteristics of the experimental waves were estimated and not precisely configured.

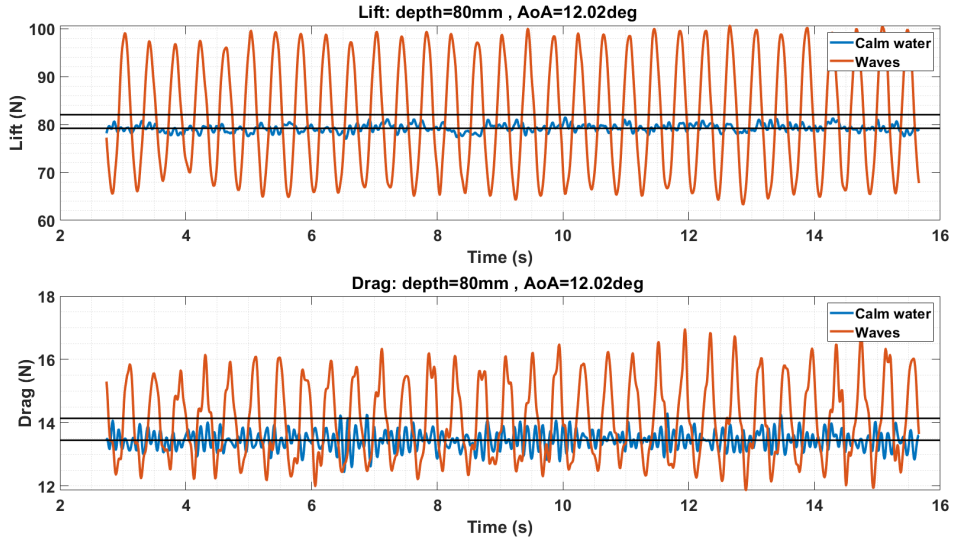

Figure 5.5: Wave sensitivity - Comparison on forces measured at SSPA between calm water and waves for identical configuration of [d = 80 mm, AoA = 12.02^o, V = 3 m/s]

Table 5.1: Mean from CFD and EFD for [d = 80 mm, AoA = 12^o, V = 3 m/s] in waves

		Lift (N)	Drag (N)
Mean CFD		71.07	12.70
Mean EFD		82.11	14.13
Variation CFD	Minimum (% of the mean)	112.1	107.7
	Maximum (% of the mean)	89.1	93.4
Variation EFD	Minimum (% of the mean)	120.9	106.2
	Maximum (% of the mean)	80.2	93.1

5.1.3 Uncertainties related to tests at SSPA

Several uncertainties are related to the experimental testing done at SSPA. The uncertainties are:

- Measures of the angle and the depth: Measuring the depth and the AoA were important sources of uncertainties. The depth is defined as the distance from the axis of rotation of the wing to the water level. The depth was adjusted by manually sliding the wing in its support and that couldn't be done with a precision higher than a couple of millimeters. In addition to that, the water surface wasn't completely flat and introduced more uncertainties.

  Despite using angle measuring devices and levels, it was not possible to precisely measure the AoA. To have a more reliable way to measure the rate of

change between different angles, the displacement of the pushrod was measured as a reference. Those measurements were then related to the AoA after the tests when it was possible to identify the pushrod height corresponding to zero lift i.e an angle of 0 degrees. Therefore, taking the pushrod as a reference and converting the measurements to angles were additional sources of uncertainties.

- Force measuring device: To measure the forces (lift and drag) applied to the wing, a force sensor was fixed to the top of the wing. The imprecision of the sensor represents another source of uncertainties.

- Uncertainties related to construction defaults of the towing tank: Imperfections in the construction of the towing tank can influence the results of the experiments. The angle of inclination of the rails on which sits the carriage can make the depth of the wing vary along the towing length. The speed control of the carriage can also be different from the target speed. Other sources of uncertainties may arise from such other parameters.

- Wave quality: The regularity of the waves may not be maintained along the whole towing length. The waves may contain harmonics when produced that dampen down while traveling or that would travel at different speeds than the waves wanted. The sides of the towing tank and the previous tests may also influence the water surface.

5.1.4 Ventilation phenomenon observed during testing at SSPA

An unexpected phenomenon was observed during testing of the wing at SSPA. For speeds higher than $V = 2$ m/s, a bubble was created at the base of the strut close to the wing. Figure 5.6 illustrates this.

(a) Strut without ventilation at low speed **(b)** Strut with ventilation occurring at $V = 3$ m/s or higher

Figure 5.6: Ventilation phenomenon occurring at the bottom of the strut

The reason that can be attributed to this phenomenon is that the strut being hollow and its end being close to the wing, lower pressure on the suction side of the wing may have caused an in-draft of air. A gap between the strut and the top fixation part of the strut may be at the origin of the infiltration of air inside the strut.

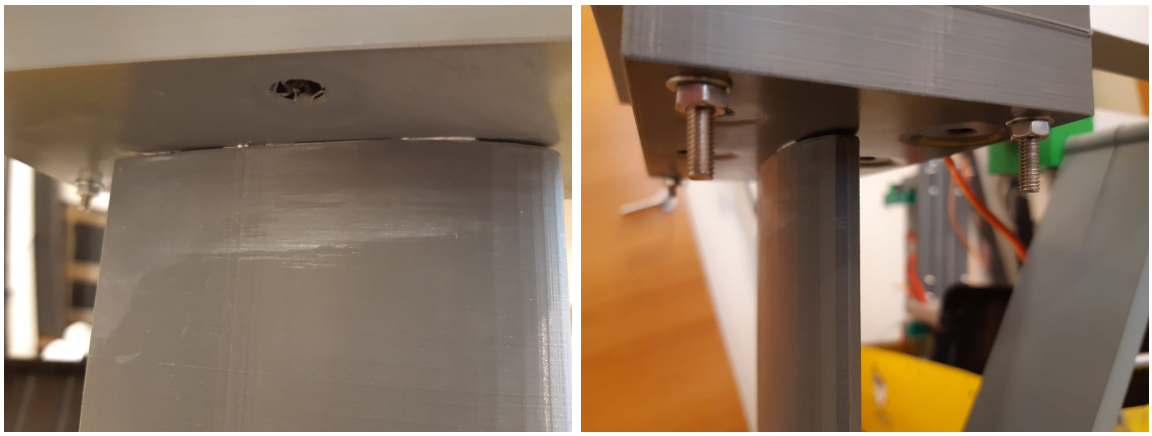

(a) Side view **(b)** Front view

Figure 5.7: Gap between the strut and the top piece possibly at the origin of the in-draft

The ventilation may have started by sucking air from the gap at the top of the strut that is shown above. The air has then circulated inside the hollow modules of the strut (see Figure 5.8) before coming out right above the wing creating a ventilation bubble.

Figure 5.8: Hollow section of the bottom strut ending close to the wing

This phenomenon may be one of the causes for lift reduction between experiment and estimations based on 2D theory. The presence of the bubble causes irregularities in the flow that disturb the expected operation of the wing. Moreover, since the air is being sucked at the bottom of the strut, under the water, that means that the pressure reduction created on the suction side of the wing is initially low enough to compensate for the hydro-static pressure. But the creation of the bubble leads the suction side of the wing to be in contact with the atmosphere, this region is then at atmospheric pressure. This shows a shortfall in low pressure region on the suction side and thus a shortfall in lift.

5.2 General behavior of the system and future work improvements

The designed system has been assembled and disassembled several times. It is very easy to take everything apart and together again. There are some things to consider. First, many of the parts are printed with PETG and then held together with nuts and bolts. When tightening the bolts, one has to be careful not to cause fractures on the printed parts. This has occurred several times during the manufacturing process of the parts and creates even longer production times. This problem can be avoided as some of these parts can be produced in other materials. During this project, no different constellations of setup have been done. Changing the setup e.g. moving the location of the transversal aluminum tubes (ID: 1.2) can be done by loosening very few nuts. The same is true for the transversal and vertical location of the front struts and elevons as for the vertical position of the rudder.

The results obtained during wings testing at SSPA have shown that the true lift produced is half the theoretical lift initially estimated from 2D theory. Since the wings have been designed based on the theoretical lift it follows that not all aspect ratios intended to be tested will produce the necessary lift for the cruise speed of 4 m/s. Consequently, other design iterations of the wings should be carried out to better implement this test feature. This can be done in different ways, 1) the dimensions of the wings such as chord length and span should be reviewed or 2) other foil profiles should be tested.

A parameter that could be made adjustable is the position of the motors on the rudder. This was not initially planned out but the position of the propulsion unit has been modified throughout the project as witnessed in Figure 3.8. This can be developed more thoroughly to study the influence of the position of the motors on maneuverability, propulsion performance, and stability. Especially to study the interaction of the motors with the elevator, control the pitching moment created by the thrust or even observe the influence of the water surface proximity on propulsion efficiency.

From the field test, it is possible to evaluate the behavioral performance of the

model. The general maneuvering is excellent as it is possible to make very sharp and fast turns. This is due to the installation of the thrusters on the rudder. When yaw pulses are sent to the flight controller, the change in direction is also affecting the direction of the wake of the thrusters. The downside to this is that the forces acting on the rudder can make the connection between the cross joint (ID: 3.11) and the servo arm slide (see Figure 5.9). This problem was originally discussed internally and also with the prototype laboratory at Chalmers University of Technology. For future improvement, this is a major topic to investigate as the connection either needs to be reinforced or the solution needs to be re-iterated.

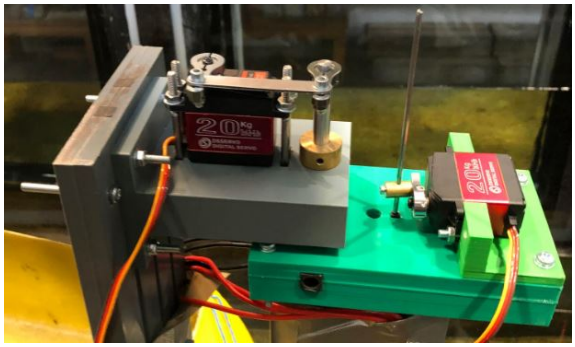

Figure 5.9: Servo connection to top cross joint (ID: 3.11)

Lift-off was never reached during field tests. As observed in Figure 4.49 and Figure 4.51, the maximum reached speed was 1.6 m/s. From the preliminary calculations, it was estimated that the required speed for take-off would be 2.5 m/s. This is due to the amount of thrust the thrusters were able to deliver. As the procurement of the thrusters was based on empirical estimations, the installed power is insufficient to reach lift-off speeds. The procurement of any thruster or motor should have been based on the towing tank tests as the resistance measured are giving a more clear picture of the required power than a Maxsurf model. The current thrusters will only yield lift-off if 1) the weight of the entire system is drastically diminished or 2) the wings are enlarged to unrealistic proportions compared to the model size. Even if the second option was applied, more drag would be created by enlarged wings thus this solution might not even work.

Regarding the behavior of the electrical components, there were some issues during tests. First, it was observed that from time to time there can be some servo jittering. This problem is fixed with several steps such as 1) making sure the cable extensions are fully connected and 2) turning any electronic component that has an interfering signal with the flight controller off. Second, the installed ESCs can get extremely hot inside the waterproof box installed on the model. They have a safety mechanism to stop working when reaching a specific temperature but this will stop all connections to the transmitter. Third, connection to the flight controller is lost for very brief moments from time to time. It is very rare but happened a few times during testing. It has not been possible to solve this issue. One proposition could be to 1) position the antennas away from the other electrical components and/or

2) outside the box. Overall, the electrical system is working very well and is very responsive to the commands done on the transmitter.

The PID setup in Star CCM+ and the results it yielded could not be tested and represent another interesting path to explore. This could be taken further by modeling the control of more motions and making the wings movable in the simulation. This would allow for potentially better tuning of the system and even simulate the behavior of the model in waves which is hard to set up and capture in reality.

An important design flaw has been highlighted during the CFD simulation of the wing and the strut. The detrimental effect of the t-joint on the wings is much worse than expected. It is shown in section 4.1.5 that this small component induces a major lift decrease and is the cause for half the drag of the wing at $V = 4$ m/s. It is a central point of improvement to make the transition between the wing and the strut as smooth as possible to prevent vortex shedding and a stagnation point.

If the model is to be used in saltwater, some pieces should be changed to stainless steel to prevent the problem arising from rusting.

5.3 Comparison of flight modes and state of the control system

As the model was tested in the Rådasjön, the manual flight mode and the stabilize flight mode were tested. It is, therefore, possible to compare the responsiveness between them.

As the manual flight mode name suggests, all inputs to the actuators are given by the operator. The responsiveness of the model is excellent as very large roll angles can be obtained (see Figure 4.50) and be re-adjusted very quickly again. The range of the servo movements can be adjusted by changing the pulses for the specific servo in question. This is a topic to investigate further as no maximum roll angle is accounted for with the current setup. Regarding the stabilization responsiveness, Figure 4.52 shows how the actuators are constantly readjusting their positions to stabilize. The test was done without any re-iteration process regarding the pulsation inputs to any of the servos meaning that the responsiveness can be even more effective with more learning of the motions as a function of the actuator positioning.

This project have been consisting of many different aspects of the model. It has therefore been very limited how the control system is set up. No scripts have been written to create the most effective and personal control system since everything is set up via Mission Planner. This control system method is easy to work with since it is a common method for RC enthusiasts to work as well. The system is working perfectly while the model is staying in displacement mode i.e. not gaining lift-off. The control system can therefore stabilize the model with ease. In later design iter-

ations of this project, the model will lift off, and the stabilizing effect of the control system will work in the same fashion as in displacement mode but due to physics, the responsiveness of the system might come short. At this stage, the tuning of the control system is crucial. For a fully personal control system, it is, therefore, more feasible with a custom script that can be loaded onto the flight controller.

As a validation of the results observed in the field test, the inclining test performed in the workshop shows that the actuators are fully responsive to the manual motion handling while in stabilize mode. This is also what can be observed in the stabilization handling from the field test. Here, the actuators are making many small micro-adjustments due to the open field factors (waves, wind, current, etc.) having much more impact on the model than in the workshop.

5.4 Incorporation of JSN-SR04T sonar sensor

The sonar study performed while running the towing tank tests at SSPA's facilities gives insight into what is achievable with such a sensor.

As the precision of the JSN-SR04T is ≈ 10 mm, it is not precise enough to capture the wave patterns in front of the model. This can be seen by evaluating the curves from Figure 4.47 and Figure 4.48 where the variance is similar between the measurements. The curves should show a clear difference between calm water and wave patterns. This can be due to how the echo sound waves are transmitted in a cone form. The sound waves will be sent back to the sensor from various locations on the wave, hence the sonar sensor will receive data from various points on the wave. This problem should be avoided in calm water as the water level during the test was as stable as it can get. But as shown in Figure 4.47, the sonar sensor reads values between $0.54 - 0.58$ m. Even though it is resulting in the correct mean value of 0.56 m, the variance is essential if installed on a hydrofoil boat as the heave of the boat is dependent on correct sonar sensor readings, thus the boat will not operate correctly due to wrong sonar sensor readings. Moreover, the actual position of the sonar on the boat places it too close to the water surface. The sonar needs to be at least 250 mm above the water surface which is currently not the case.

This project only touched briefly upon the sonar sensor and further studies need to be done with the JSN-SR04T sonar sensor to fully understand its capabilities. Alternatively, more precise and expensive sonar sensors can be tested as the Ardupilot firmware can be used with many different sonar sensors.

6
Conclusion

A model-scale foiling boat has been manufactured and tested during the time frame of this thesis. With the yielded results, this thesis should be seen as the first iteration as upgrades and adjustments can be implemented in later stages. One objective of the model-scale foiling boat is for future students to implement new ideas. The model is therefore ready for such ideas.

6.1 Hydro-dynamical design

A surface interaction study was performed through CFD analysis. It was found that both lift- and drag forces increase as the wing is deployed deeper underneath the water surface. The effect of the water surface can be seen until $d = 1.5c$ where the forces stagnate. This study was performed with an AS5046 wing with $c = 60$ mm and without any strut attachment. The efficiency of the wing is 7.2 % higher for $d = 1.5c$ compared to $d = 0.5c$ with AoA $= 8^o$ and 10.1 % higher for $d = 1.5c$ compared to $d = 0.5c$ with AoA $= 4^o$. This study yielded the determination of a sweet spot for the operation of the wings situated between $d = 1c$ and $d = 1.5c$ where drag was minimized while maintaining desired lift properties.

GOE460 foil was selected for the wing profile and NACA0015 foil was selected for the strut profile. CFD and EFD testing methods have been applied to gain knowledge of the hydro-dynamical behavior of the designed parts. Different sets of configurations (varying AoA, depth and velocity) have been tested in the two methods, thus for configuration comparison, the AoA $= 6^o$ at $V = [2, 4]$ m/s configurations were used. The lift force deviations between the two methods are $6.8 - 31.6$ % whereas the drag force deviations between the two methods are $3.6 - 7.3$ %. The drag forces are much more comparable between the two methods than the lift forces. The root of the problem can be caused by many unknown factors regarding the setup in both methods. But the main source of deviation between results from CFD to EFD could be attributed to the way the conversion from pushrod displacement (quantity measured as a reference during testing at SSPA to then evaluate the angles) to angles was done. Indeed, lift measured was post-processed and used as a reference for the conversion. The conversion is based on the hypothesis that lift of 0 N corresponded to AoA $= 0^o$. However, this postulate might have been misleading since it is possible that due to the interaction between the strut and the wing, 0 N of lift was obtained for a small positive angle. Consequently, the conversion to angle might need to be reviewed and would in this case yield a better match to CFD results. In addition

to that, the wings were 3D-printed and thus the symmetry of the wings cannot be fully guaranteed to result in another source of uncertainty.

A small study on the interaction between wing and strut was performed. This study was not initially intended but due to lift drastically decreasing for $V = 4$ m/s at AoA $= 2^o$ in calm water CFD simulations, this had to be investigated. From this study, it can be seen that the wing on its own is creating lift up to 30 N more compared to the same configuration with the strut. This study leads to further investigation of the impact of the designed t-joint (ID: 2.11). Results from a simulation without the t-joint show that such a small piece (Ø12mm) massively disturbs the flow and creates larger pressure on the suction side while losing pressure on the pressure side of the foil. The effect of this is an almost complete loss of lift in CFD. As the EFD results show, this is not completely true as lift is obtained at small AoA. But this study does show the importance of every little detail when designing components with good hydro-dynamical characteristics.

Several additional experimental tests were performed as a supplement to data gathering of the different parts. A towing tank test of the bare hull was performed with $V = [2, 3, 4, 5]$ m/s. The resistance of the bare hull was measured to $R = [10.77, 13.08, 13.7, 15.06]$ N. The model starts swaying at 5 m/s hence the resistance may be higher than measured at this speed. A towing tank test of the hull with rudder and thrusters was performed. This test was only done at $V = 2$ m/s. The propellers were not turning while towing hence the total resistance may be overestimated from this test. The measured resistance was 35.73 N. A bollard pull test of the model with the dual thruster setup was also performed. The measured thrust was 45 N.

During testing at SSPA's facilities, a towing tank test of the front wing with strut was done. The configuration of the wing during this test was $d = 80$ mm, AoA $= 12.02^o$ and $V = 3$ m/s. The forces from this test were compared to the forces from the identical configuration test in calm water, showing 5.1 % more lift in waves but also 4.8 % more drag. The efficiencies between calm water and waves are therefore very close.

6.2 System design

The objective of the system is to be able to easily set up different configurations for the foils. A three-dimensional position system has been manufactured with the help of different materials such as aluminum (tubes), steel (bolts), and PETG (3D printed components). The reason for the use of different materials is the weight/strength relation as some components are subject to high loads which call for high tensile strength whereas other components are not. Thus they have to be as light as possible. The weight is kept to a minimum as obtaining lift-off occurs more swiftly.

Another objective of the system is to easily replace components. This is handled by designing all strut- and wing components in modules. A strut, therefore, consists

of four modules and a front wing is consisting of two center modules, four regular wing modules, and two wing end modules. The aspect ratio can be modified by manufacturing and adding additional regular wing modules. The carbon fiber tubes are used to strengthen the connections between the pieces since the PETG is not supposed to carry any major load.

During field testing, lift-off was not obtained. This is due to the propulsive power being insufficient hence not overcoming the drag created by the different parts (hull, wings, struts, and thrusters). All parts of the model were tested at SSPA's facilities to learn the total drag. A bollard pull test was also performed in SSPA's towing tank. From these tests, it was clear that a velocity of 2 m/s could be reachable. In Rådasjön, the obtained velocity was 1.6 m/s. For future lift-off and foiling, it is therefore essential to install a more powerful propulsive unit.

6.3 Control system

ArduPlane has been used as the control system firmware for this thesis. The responsiveness of the system is working very well. This was tested through the inclination of the model and monitoring of the roll and pitch angles and the actuator's responsiveness. It was intended to monitor the heave motion as well but due to lift-off not being obtained, this is for later design iterations of the project.

Through the software Mission Planner, it is easy to change parameters and set up flight modes. In this thesis, the manual flight mode and the stabilize flight mode have been tested. The manual flight mode lets the operator control all motions of the model. In the stabilize flight mode, the GPS sends signals to the actuators to gain the correct up-right moment. Many different flight modes are available thus there might be a more appropriate flight mode relevant for the model. The stabilize flight mode worked very well when the model was in displacement operation as the actuators constantly tried to keep the model level when maneuvering. In later iterations of the project, the stabilize flight mode will need fine-tuning as foilborne operations require optimal responsiveness.

The JSN-SR04T sonar sensor was tested during the towing tank tests at SSPA. The intended use of it is to read the water level and the waves in front of the model. The main issue with the sonar is that the precision is ≈10 mm. This is not suitable for a model-scale boat as this is a large percentage of the elevation. As the actuators are supposed to respond to the incoming waves, the precision of the sonar sensor is of great importance. The comparison between the calm water and waves shows that the sonar does sense more disturbance in wave conditions but is no way near as detailed as desired. Some disturbance is also noticed when operating in calm water whereas the reading of the sonar should be constant.

Bibliography

O. Faltinsen. *Hydrodynamics of high-speed marine vehicles*. Cambridge University Press, 2005.

G. Franklin, D. Powell, and E.-N. Abbas. *Feedback control of dynamic systems*. 2009.

C.-E. Janson. Waves, Motions and Manoeuvring lecture notes, 3 2015.

C. R. J. Johnston. Naval Engineers Journal Vol. 97 No. 2. 1985. ISSN 0028-1425.

J. Liu and R. Hekkenberg. Impacts of rudder profiles on ship manoeuvrability MoVe IT! (Modernisation of vessels for inland waterway freight transport) View project CGT determination for ships View project. Technical report, 2015. URL `https://www.researchgate.net/publication/281715555`.

M. Moonesun, K. Y. Mikhailovich, D. Tahvildarzade, and M. Javadi. Practical scaling method for underwater hydrodynamic model test of submarine. *Journal of the Korean Society of Marine Engineering*, 38(10):1217–1224, 12 2014. ISSN 2234-7925. doi: 10.5916/jkosme.2014.38.10.1217.

P. Ploé. *Surrogate-based optimization of hydrofoil shapes using RANS simulations*. PhD thesis, 2018.

S. Steen. Lecture notes in Experimental Methods in Marine Hydrodynamics. Technical report, Norges Teknisk-Naturvitenskapelige Universitet, 2014.

Y. Tanaka. Active vibration compensator on moving vessel by hydraulic parallel mechanism. *International Journal of Hydromechatronics*, 1(3):350, 2018. ISSN 2515-0464. doi: 10.1504/ijhm.2018.094887.

F. M. White. *Fluid Dynamics*. 2011.

A

Lift estimation script

```
clc
clear all
close all
%% Data
% General
g = 9.81;                       % Gravity [m/s2]
nu = 1.000 * 10^(-6);           % Kinematic viscosity [m2/s]
rho = 1000;                     % Density [kg/m3]
C_L = linspace(0.1,1.4,10);     % Lift coefficient range [-]

% Inputs
M = 13.5;                       % Mass [kg]
c = (8)/100;                    % Chord length [m] - 6 or 8
AR = [6,8,10];                  % Aspect Ratio [-] - 6, 8 & 10
V = (2:9)*0.5144;               % Velocity [m/s] - 2-4

b = c * AR;                     % Width of foil  [m]
A = b .* c;                     % Area [m2]

%% Preallocating matrices for faster computational time
L = zeros(length(V),length(C_L),length(c));
int_m = zeros(1,length(C_L),length(c));

%% Lift
for i = 1:length(V)
    for j = 1:length(C_L)
        for k = 1: length(b)
            L(i,j,k) = 1/2 * rho * V(i)^2 * C_L(j) * A(k);
        end
    end
end

% Interpolating points achieving lift
for j = 1:length(C_L)
    for k =1:length(b)
        int_m(:,j,k) = interp1(L(:,j,k),V,M*g);
    end
end

%% Plot
figure
sgtitle(sprintf('Chord Length = %0.3f m',c),'Fontsize',24)
```

```
for k = 1:length(b)
    subplot(size(AR,1),size(AR,2),k)
    plot(V,L(:,:,k),'Linewidth',2)
    hold on
    plot(int_m(:,:,k),M*g,'*k')
    grid minor
    ylabel('Lift (N)')
    xlabel('Speed (m/s)')
    title(sprintf('b=%0.3f m',b(k)))
    %set(gca,'FontSize',18)
    for j = 1:length(C_L)
        ccm{j} = ['C_L=', num2str(C_L(j))];
        legend(ccm,'Location','Northwest')
    end
end
```

B

Foil characteristics

B.1 GOE460

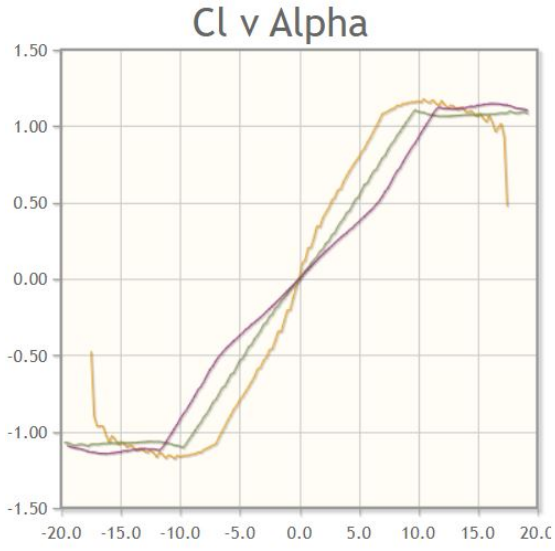

(a) Lift coefficient vs. AoA

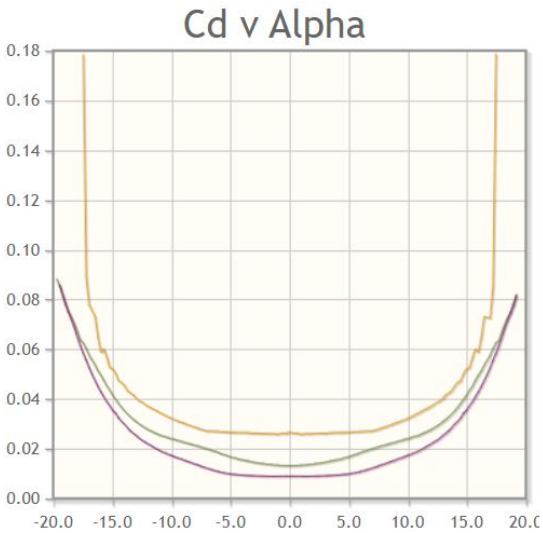

(b) Drag coefficient vs. AoA

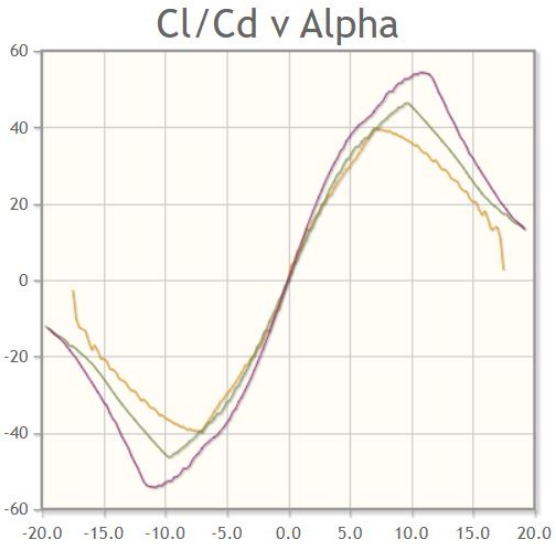

(c) Lift/drag coefficient ratio vs. AoA

Figure B.1: Characteristics of GOE460 foil[1]at Re = 100,000 (orange), Re = 200,000 (green) and Re = 500,000 (purple)

B.2 NACA0015

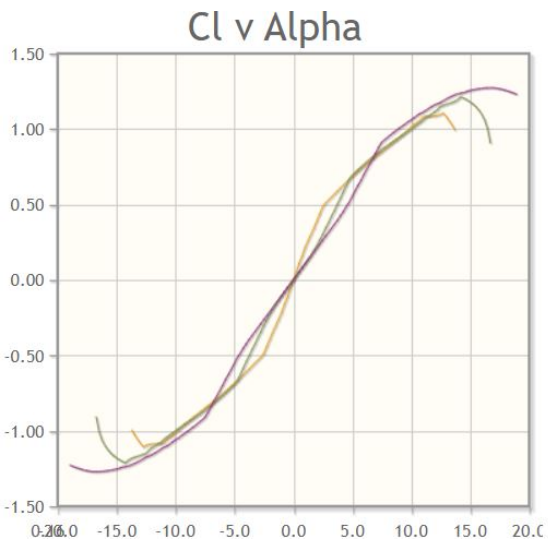

(a) Lift coefficient vs. AoA

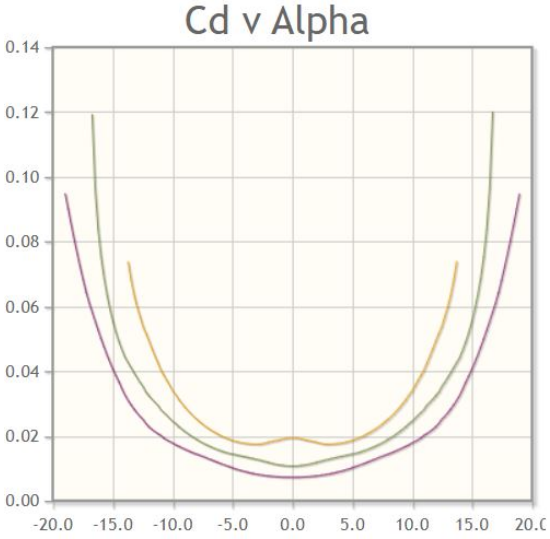

(b) Drag coefficient vs. AoA

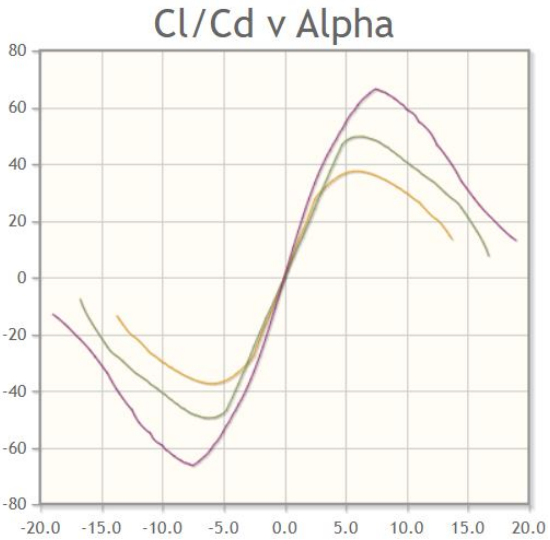

(c) Lift/drag coefficient ratio vs. AoA

Figure B.2: Characteristics of NACA0015 foil[2]at Re = 100,000 (orange), Re = 200,000 (green) and Re = 500,000 (purple)

[1]http://airfoiltools.com/airfoil/details?airfoil=goe460-il
[2]http://airfoiltools.com/airfoil/details?airfoil=naca0015-il

C
System design

C.1 Basic design

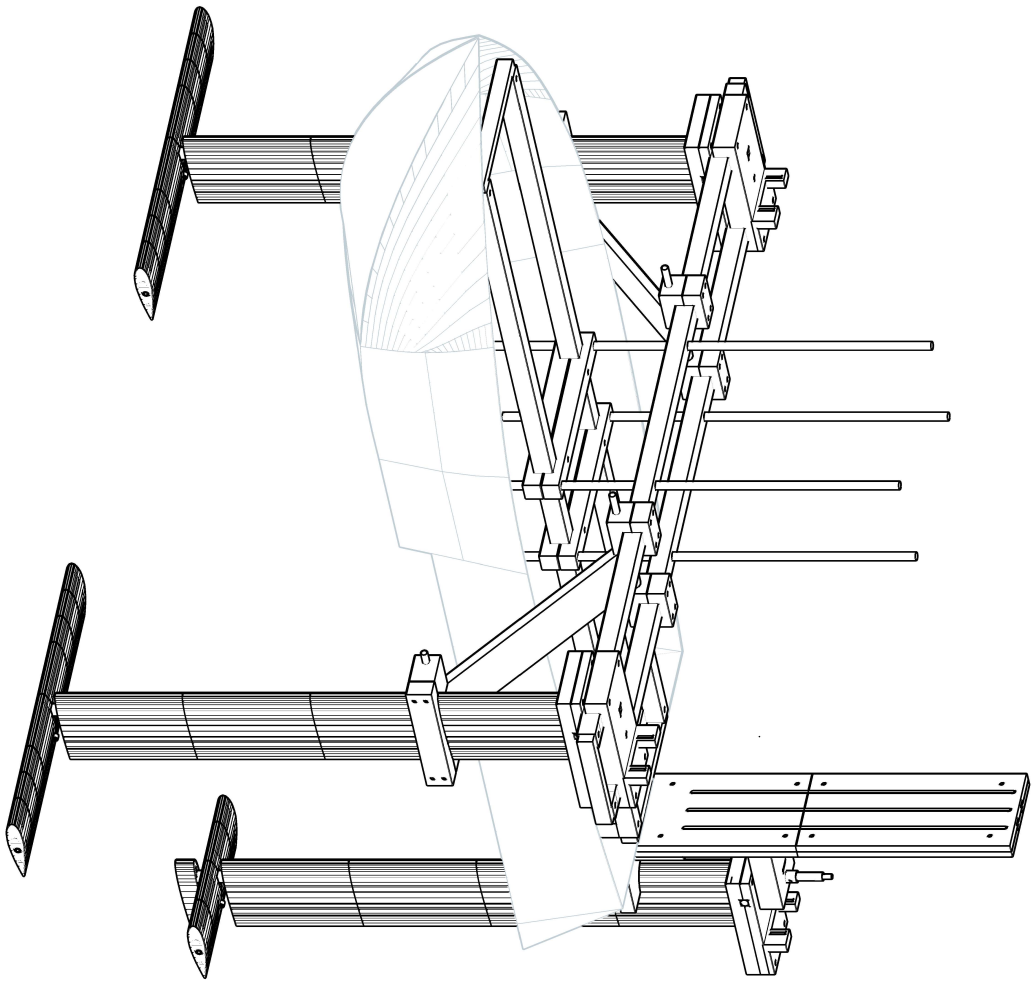

C.2 Frame system

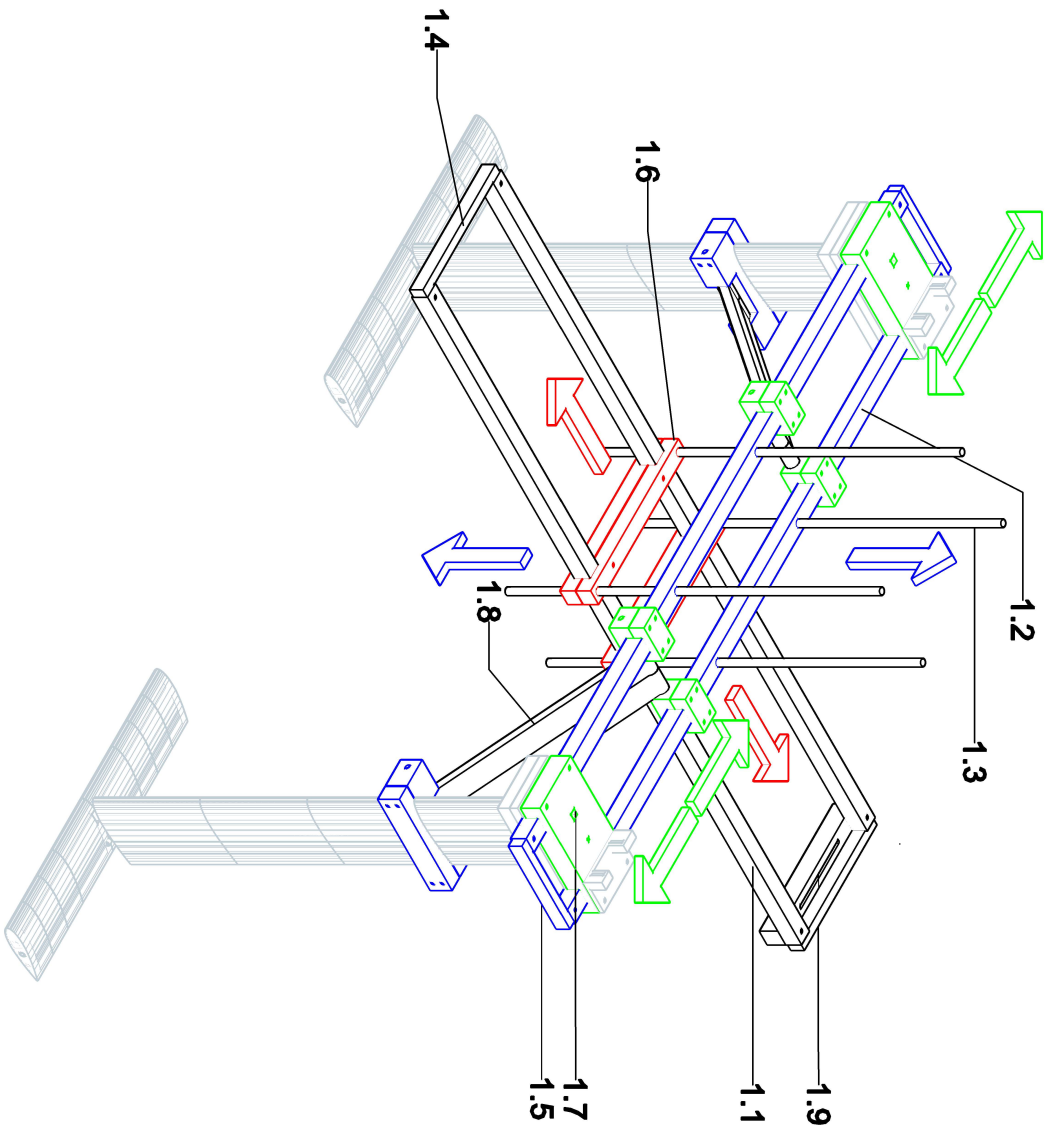

C.3 Front strut and elevons

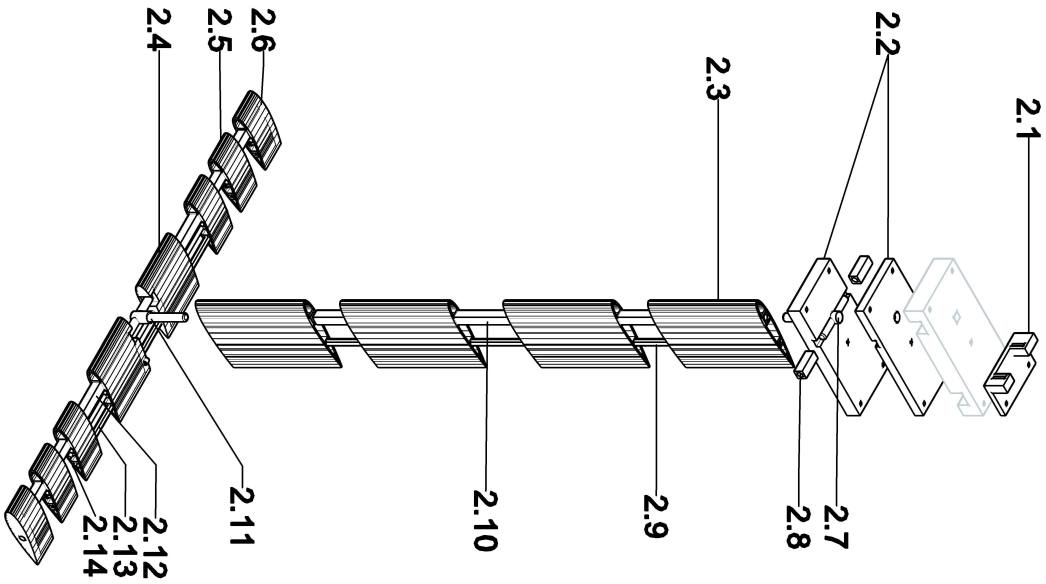

C.4 Rudder and elevator

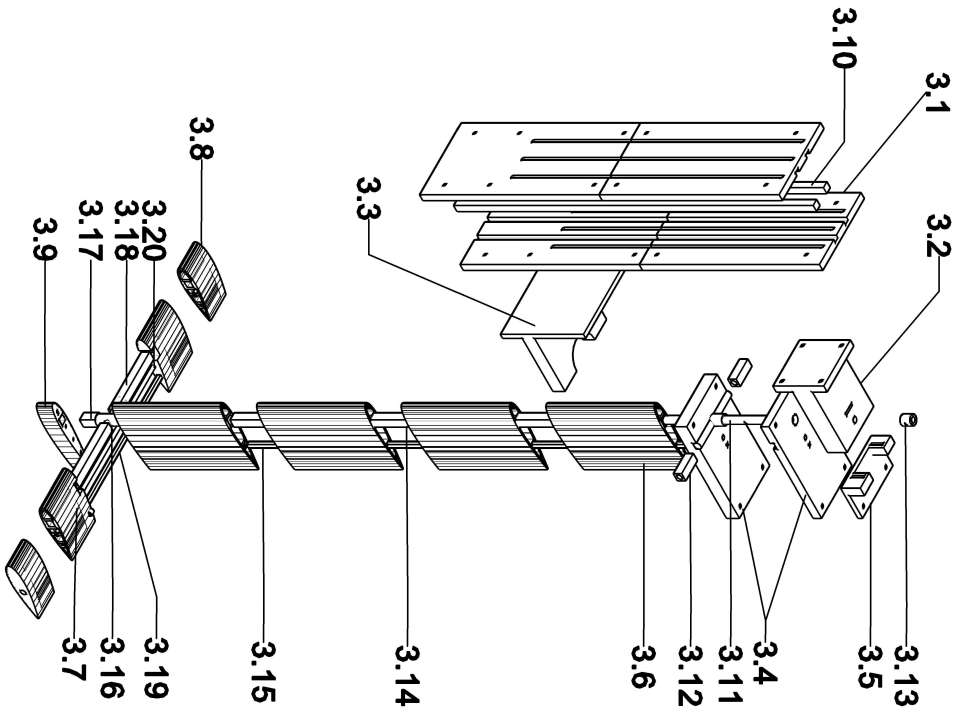

C.5 Pictures of the system

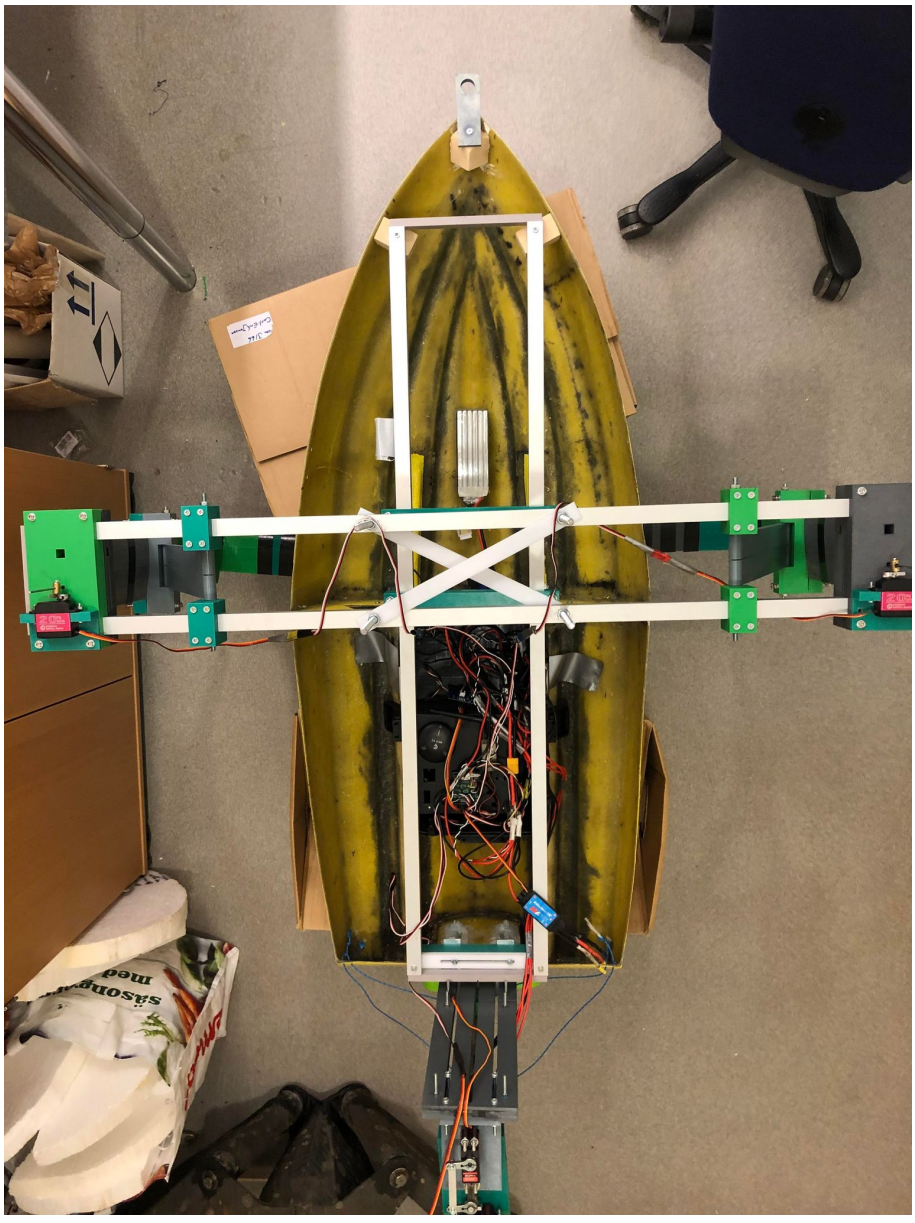

Figure C.1: Top view - Rail system

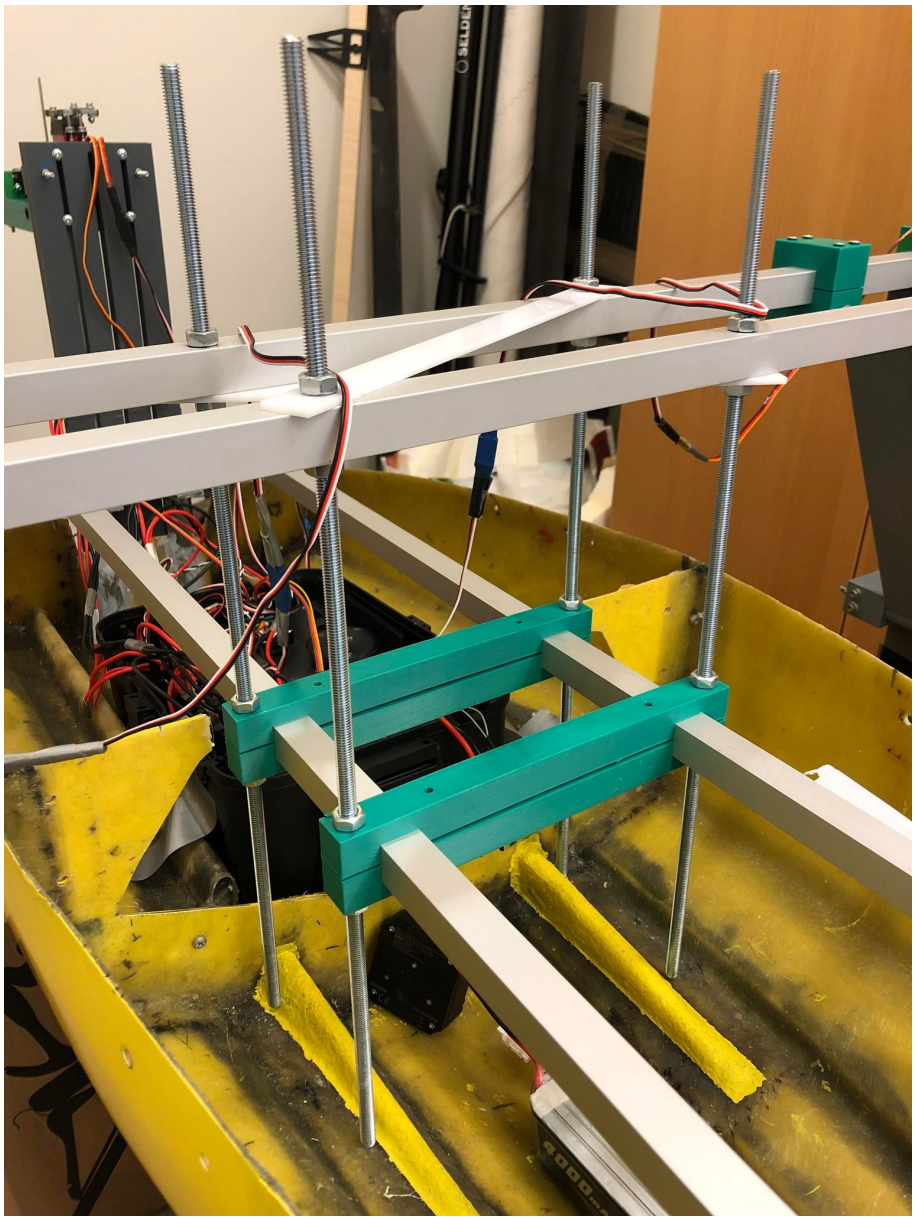

Figure C.2: Vertical rail system

Figure C.3: Front wing with strut

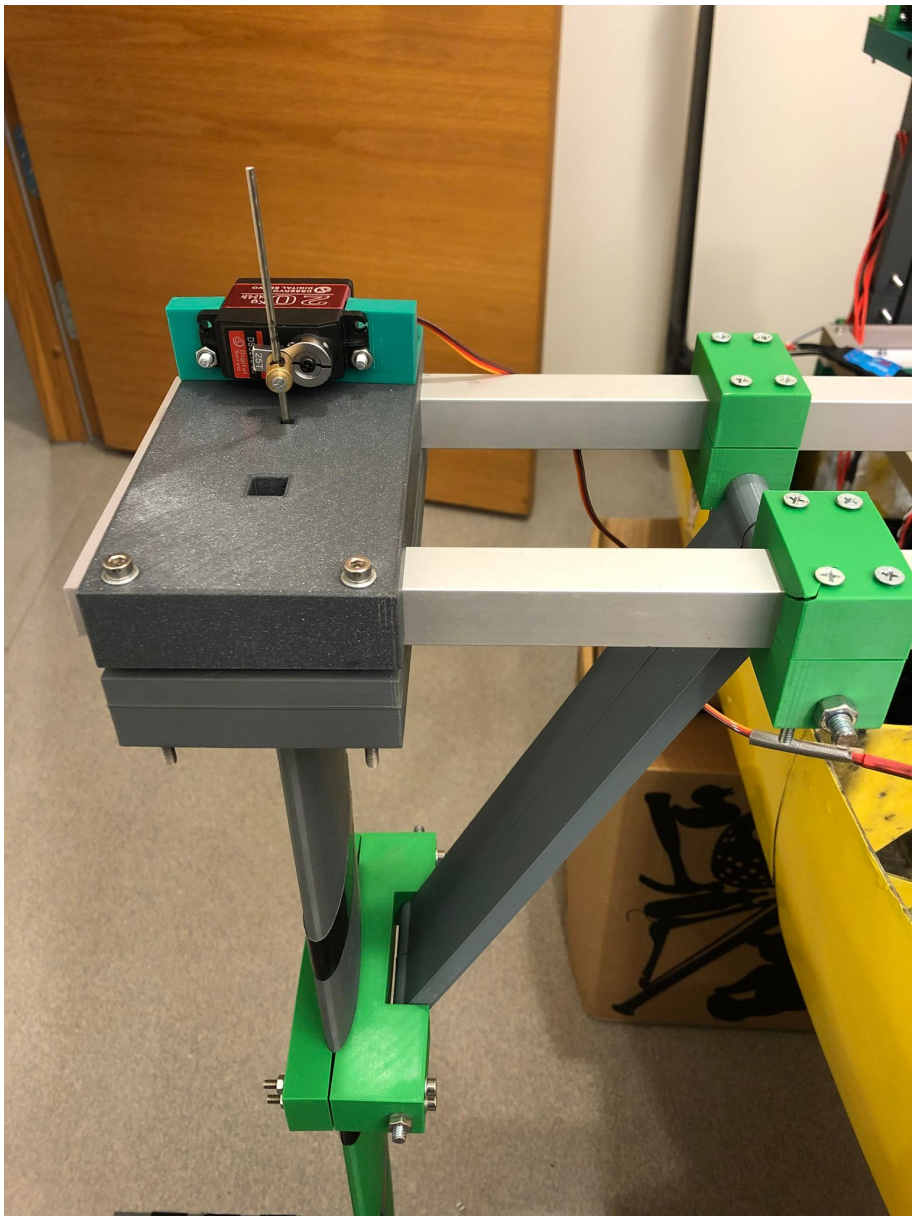

Figure C.4: Top of front strut

Figure C.5: Rudder

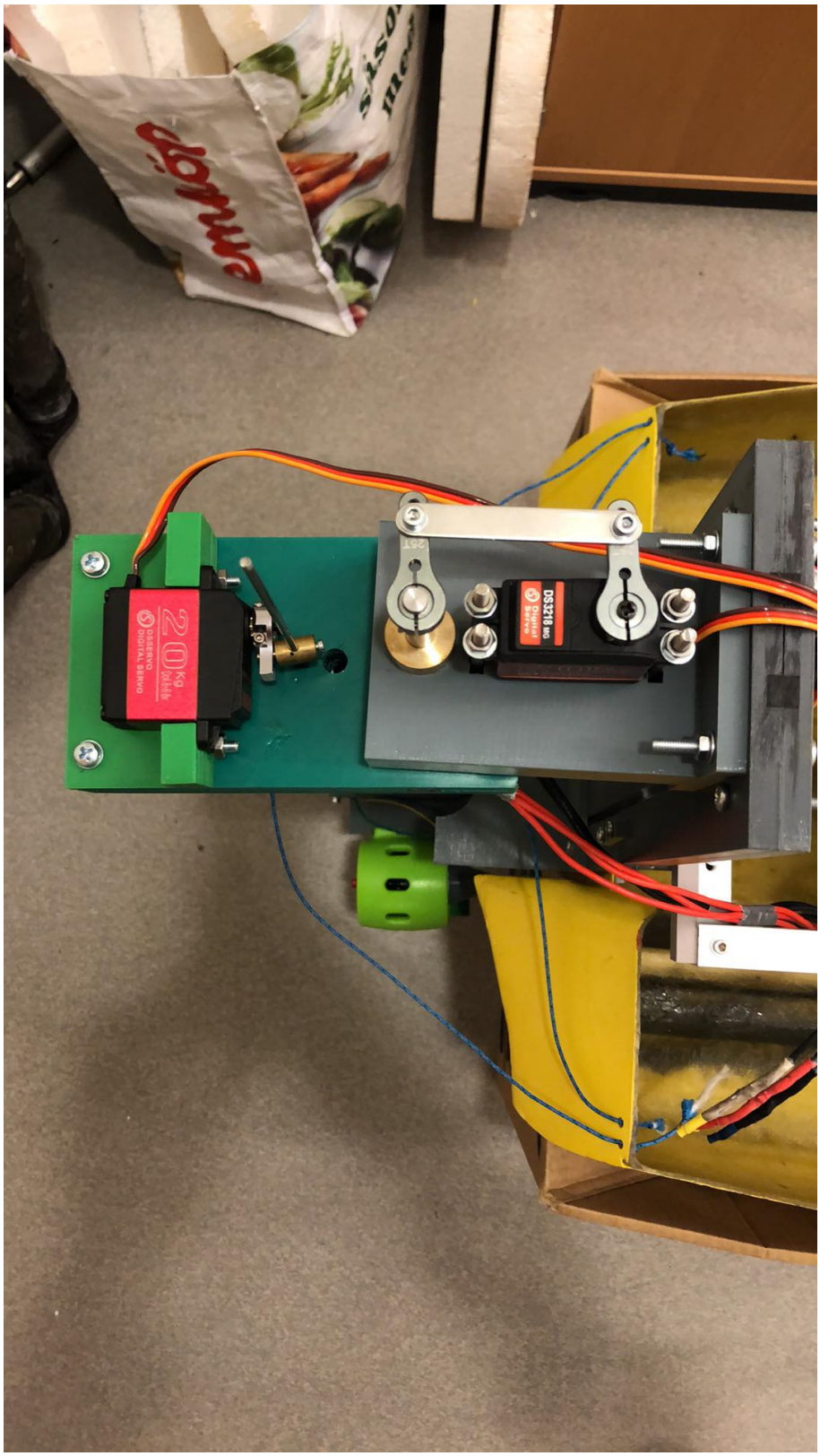

Figure C.6: Top of rudder

D

Components list

Table D.1: Components list

	Components list					
	ID	Component	Material	Amount	Printing time/unit (h)	Total printing time (h)
Frame System	1.1	Longitudinal beam	Aluminum	2	-	
	1.2	Transversal beam	Aluminum	2	-	
	1.3	Vertical bolt	Steel	4	-	
	1.4	End Piece Longitudinal	PETG	2	2,5	5
	1.5	End Piece Transversal	PETG	2	1,75	3,5
	1.6	Rail Fixation	PETG	2	7,5	15
	1.7	Strut Fixation	PETG	2	9	18
	1.8	Girder Struts	PETG	2	19	38
	1.9	Aft Spacer	PETG	1	3,25	3,25
Front Strut & Wing	2.1	Servo fixation	PETG	2	1,75	3,5
	2.2	Top strut	PETG	2	11,25	22,5
	2.3	Strut module	PETG	8	10,5	84
	2.4	Center wing module	PETG	4	6,5	26
	2.5	Wing module	PETG	8	3,3	26,4
	2.6	Wing end	PETG	4	3	12
	2.7	Top t-joint	Steel	2	-	
	2.8	Fitting	Carbon fiber	4	-	
	2.9	Push rod guidance	Carbon fiber	2	-	
	2.10	Stiffener	Carbon fiber	2	-	
	2.11	Bottom t-joint	Steel	2	-	
	2.12	Stiffener	Carbon fiber	4	-	
	2.13	Stiffener	Carbon fiber	2	-	
	2.14	Bolt	Steel	2	-	
Rudder & rear Wing	3.1	Vertical rail system	PETG	1	36	36
	3.2	Rudder fixation	PETG	1	9	9
	3.3	Girder rudder	PETG	1	7,5	7,5
	3.4	Rudder Top	PETG	1	10,25	10,25
	3.5	Servo fixation	PETG	1	1,75	1,75
	3.6	Strut module	PETG	4	10,5	42
	3.7	Center wing	PETG	2	4,5	9
	3.8	Wing end	PETG	2	3	6
	3.9	Propulsion fixation	PETG	1	1,5	1,5
	3.10	Vertical stiffener - rail system	Carbon fiber	2		
	3.11	Top cross joint	Steel	1		
	3.12	Fitting	Carbon fiber	2		
	3.13	O-ring	Steel	1		
	3.14	Stiffener	Carbon fiber	1		
	3.15	Push rod guidance	Carbon fiber	1		
	3.16	Bottom cross joint	Steel	1		
	3.17	Fitting	Carbon fiber	1		
	3.18	Stiffener	Carbon fiber	1		
	3.19	Stiffener	Carbon fiber	1		
	3.20	Bolt	Steel	1		
					SUM	380,15

E

Mission Planner parameter list

Table E.1: Mission Plannner parameter list

Parameter	Value	Parameter	Value
BRD_PWM_COUNT	8	SERVO3_MIN	1100
BRD_SAFETY_MASK	Check everything	SERVO3_TRIM	1100
BRD_SAFETY_ENABLE	0	SERVO3_MAX	2200
BRD_SAFETY_OPTION	2	SERVO4_FUNCTION	21 (rudder)
RC_PROTOCOL	uncheck 'all' ->check everything	SERVO4_MIN	1100
RC1_OPTION	0	SERVO4_TRIM	1500
RC2_OPTION	0	SERVO4_MAX	1900
RC3_OPTION	0	SERVO5_FUNCTION	77 (left elevon)
RC4_OPTION	0	SERVO5_MIN	800
RC5_OPTION	0	SERVO5_TRIM	1500
RC6_OPTION	0	SERVO5_MAX	2200
FLTMODE_CH	5	SERVO05_REVERSED	0-1 (Check for orientation on the wing)
FLTMODE1	0 (Manuel)	SERVO6_FUNCTION	78 (right elevon)
FLTMODE2	Not used	SERVO6_MIN	800
FLTMODE3	Not Used	SERVO6_TRIM	1500
FLTMODE4	6	SERVO6_MAX	2200
FLTMODE5	Not used	SERVO06_REVERSED	0-1 (Check for orientation on the wing)
FLTMODE6	2	SERVO7_FUNCTION	0
SERVO1_FUNCTION	70 (throttle)	SERVO7_MIN	1100
SERVO1_MIN	1100	SERVO7_TRIM	1500
SERVO1_TRIM	1100	SERVO7_MAX	1900
SERVO1_MAX	2200	RNGFND_TYPE	30
SERVO2_FUNCTION	19 (elevator)	RNFND1_MAX	450
SERVO2_MIN	800	RNFND1_MIN	25
SERVO2_TRIM	1350	RNGFND_STOP_PIN	58 (Aux1)
SERVO2_MAX	1900	RNGFND_PIN	59 (Aux2)
SERVO02_REVERSED	0-1 (Check for orientation on the wing)	ALT_HOLD_FBWCM	25 (dependent on desired ride height)
SERVO3_FUNCTION	70 (throttle)		

F
CFD results

F.1 CFD files list

Table F.1: CFD simulations file list

Simulation file	AoA (deg)	Speed (m/s)	Depth (mm)
Calm water			
Calm_water_AoA2_D8_V2_comparison_study.sim	2	2	8
Calm_water_AoA2_D12_V2_comparison_study.sim	2	2	12
Calm_water_AoA4_D8_V2_comparison_study.sim	4	2	8
Calm_water_AoA4_D12_V2_comparison_study.sim	4	2	12
Calm_water_AoA6_D8_V2_comparison_study.sim	6	2	8
Calm_water_AoA6_D12_V2_comparison_study.sim	6	2	12
Calm_water_AoA2_D8_V3_comparison_study.sim	2	3	8
Calm_water_AoA2_D12_V3_comparison_study.sim	2	3	12
Calm_water_AoA4_D8_V3_comparison_study.sim	4	3	8
Calm_water_AoA4_D12_V3_comparison_study.sim	4	3	12
Calm_water_AoA6_D8_V3_comparison_study.sim	6	3	8
Calm_water_AoA6_D12_V3_comparison_study.sim	6	3	12
Calm_water_AoA2_D8_V4_comparison_study.sim	2	4	8
Calm_water_AoA2_D12_V4_comparison_study.sim	2	4	12
Calm_water_AoA4_D8_V4_comparison_study.sim	4	4	8
Calm_water_AoA4_D12_V4_comparison_study.sim	4	4	12
Calm_water_AoA6_D8_V4_comparison_study.sim	6	4	8
Calm_water_AoA6_D12_V4_comparison_study.sim	6	4	12
Waves			
Waves_AoA12_D8_V3_comparison_study.sim	12	3	8
Water surface interaction			
AS5046_Surface_interaction_AOA4_D1c.sim	4	4	1c
AS5046_Surface_interaction_AOA4_D4c.sim	4	4	4c
AS5046_Surface_interaction_AOA4_D05c.sim	4	4	0.5c
AS5046_Surface_interaction_AOA4_D15c.sim	4	4	1.5c
AS5046_Surface_interaction_AOA8_D1c.sim	8	4	1c
AS5046_Surface_interaction_AOA8_D4c.sim	8	4	4c
AS5046_Surface_interaction_AOA8_D05c.sim	8	4	0.5c
AS5046_Surface_interaction_AOA8_D15c.sim	8	4	1.5c
AS5046_Surface_interaction_AOA_8_D1c.sim	-8	4	1c
AS5046_Surface_interaction_AOA_8_D4c.sim	-8	4	4c
AS5046_Surface_interaction_AOA_8_D05c.sim	-8	4	0.5c
AS5046_Surface_interaction_AOA_8_D15c.sim	-8	4	1.5c

F.2 Water surface interaction

Table F.2: Surface interaction study CFD results for AoA = 8^o

Speed : 4 m/s | AoA = 8^o				
Depth	CD	CL	Lift (N)	Drag (N)
0.5c	0.045	0.41	35.28	3.85
1c	0.05	0.48	41.11	4.31
1.5c	0.05	0.5	42.63	4.34
4c	0.05	0.5	43.44	4.32

Table F.3: Surface interaction study CFD results for AoA = 4^o

Speed : 4 m/s | AoA = 4^o				
Depth	CD	CL	Lift (N)	Drag (N)
0.5c	0.027	0.23	19.45	2.36
1c	0.029	0.26	22.51	2.53
1.5c	0.03	0.27	23.23	2.56
4c	0.03	0.28	23.88	2.56

Table F.4: Surface interaction study CFD results for AoA = -8^o

Speed : 4 m/s | AoA = -8^o				
Depth	CD	CL	Lift (N)	Drag (N)
0.5c	0.0396	-0.33	-28.16	3.41
1c	0.041	-0.36	-30.84	3.52
1.5c	0.041	-0.37	-32.14	3.56
4c	0.04	-0.37	-31.64	3.46

F.3 Front wing with strut - Calm water

```
clc
clear all
close all
% This script analyses the data from the CFD comparison simulations
% performed on the 26-05-2022.
```

```
%% Data
% All data are extracted independently from each .sim file
% The csv files are set up: Lift(1), CL(2), Drag(3), CD(4)

AoA = [2,4,6]; % Angle of Attack
% AoA = 2
AoA2_D8_V2 = importdata('AoA2_D8_V2.csv');
AoA2_D8_V3 = importdata('AoA2_D8_V3.csv');
AoA2_D8_V4 = importdata('AoA2_D8_V4.csv');
AoA2_D12_V2 = importdata('AoA2_D12_V2.csv');
AoA2_D12_V3 = importdata('AoA2_D12_V3.csv');
AoA2_D12_V4 = importdata('AoA2_D12_V4.csv');
% AoA = 4
AoA4_D8_V2 = importdata('AoA4_D8_V2.csv');
AoA4_D8_V3 = importdata('AoA4_D8_V3.csv');
AoA4_D8_V4 = importdata('AoA4_D8_V4.csv');
AoA4_D12_V2 = importdata('AoA4_D12_V2.csv');
AoA4_D12_V3 = importdata('AoA4_D12_V3.csv');
AoA4_D12_V4 = importdata('AoA4_D12_V4.csv');
% AoA = 6
AoA6_D8_V2 = importdata('AoA6_D8_V2.csv');
AoA6_D8_V3 = importdata('AoA6_D8_V3.csv');
AoA6_D8_V4 = importdata('AoA6_D8_V4.csv');
AoA6_D12_V2 = importdata('AoA6_D12_V2.csv');
AoA6_D12_V3 = importdata('AoA6_D12_V3.csv');
AoA6_D12_V4 = importdata('AoA6_D12_V4.csv');

%% Clean up
% As vortix shedding is occuring in the simulations and no clear
% convergence is achieved, the mean value of the convergence area is
% extracted as the converged value.

val_cl = 5000; % clean up point

% AoA=2
AoA2_D8_V2 = AoA2_D8_V2([end-val_cl:end],:);
AoA2_D8_V2_mean = mean(AoA2_D8_V2);
AoA2_D8_V3 = AoA2_D8_V3([end-val_cl:end],:);
AoA2_D8_V3_mean = mean(AoA2_D8_V3);
AoA2_D8_V4 = AoA2_D8_V4([end-val_cl:end],:);
AoA2_D8_V4_mean = mean(AoA2_D8_V4);

% Speciel treatment for this case
AoA2_D12_V2_mean_L = mean(AoA2_D12_V2([1000:1849],1));
AoA2_D12_V2_mean_CL = mean(AoA2_D12_V2([1000:1849],2));
AoA2_D12_V2_mean_D = mean(AoA2_D12_V2([1000:1849],3));
AoA2_D12_V2_mean_CD = mean(AoA2_D12_V2([1000:end],4));
AoA2_D12_V2_mean = [AoA2_D12_V2_mean_L,AoA2_D12_V2_mean_CL,...
                    AoA2_D12_V2_mean_D,AoA2_D12_V2_mean_CD];

AoA2_D12_V3 = AoA2_D12_V3([end-val_cl:end],:);
AoA2_D12_V3_mean = mean(AoA2_D12_V3);
AoA2_D12_V4 = AoA2_D12_V4([end-val_cl:end],:);
AoA2_D12_V4_mean = mean(AoA2_D12_V4);

% AoA=4
```

```
AoA4_D8_V2 = AoA4_D8_V2([end-val_cl:end],:);
AoA4_D8_V2_mean = mean(AoA4_D8_V2);
AoA4_D8_V3 = AoA4_D8_V3([end-val_cl:end],:);
AoA4_D8_V3_mean = mean(AoA4_D8_V3);
AoA4_D8_V4 = AoA4_D8_V4([end-val_cl:end],:);
AoA4_D8_V4_mean = mean(AoA4_D8_V4);
AoA4_D8_V4_mean(2)=AoA4_D8_V4_mean(2)/4; % Wrong reference speed in .sim
AoA4_D8_V4_mean(4)=AoA4_D8_V4_mean(4)/4; % Wrong reference speed in .sim

AoA4_D12_V2 = AoA4_D12_V2([end-val_cl:end],:);
AoA4_D12_V2_mean = mean(AoA4_D12_V2);
AoA4_D12_V3 = AoA4_D12_V3([end-val_cl:end],:);
AoA4_D12_V3_mean = mean(AoA4_D12_V3);
AoA4_D12_V4 = AoA4_D12_V4([end-val_cl:end],:);
AoA4_D12_V4_mean = mean(AoA4_D12_V4);

%AoA=6
AoA6_D8_V2 = AoA6_D8_V2([end-val_cl:end],:);
AoA6_D8_V2_mean = mean(AoA6_D8_V2);
AoA6_D8_V3 = AoA6_D8_V3([end-val_cl:end],:);
AoA6_D8_V3_mean = mean(AoA6_D8_V3);
AoA6_D8_V4 = AoA6_D8_V4([end-val_cl:end],:);
AoA6_D8_V4_mean = mean(AoA6_D8_V4);

AoA6_D12_V2 = AoA6_D12_V2([end-val_cl:end],:);
AoA6_D12_V2_mean = mean(AoA6_D12_V2);
AoA6_D12_V3 = AoA6_D12_V3([end-val_cl:end],:);
AoA6_D12_V3_mean = mean(AoA6_D12_V3);
AoA6_D12_V4 = AoA6_D12_V4([end-val_cl:end],:);
AoA6_D12_V4_mean = mean(AoA6_D12_V4);

%% Tables
i = 1; % Lift
MF = 2;  % Multiplication factor (for full wing lift and drag)
table([AoA2_D12_V2_mean(i);AoA4_D12_V2_mean(i)*MF;AoA6_D12_V2_mean(i)*MF],...
[AoA2_D12_V3_mean(i)*MF;AoA4_D12_V3_mean(i)*MF;AoA6_D12_V3_mean(i)*MF],...
[AoA2_D12_V4_mean(i)*MF;AoA4_D12_V4_mean(i)*MF;AoA6_D12_V4_mean(i)*MF],...
[AoA2_D8_V2_mean(i)*MF;AoA4_D8_V2_mean(i)*MF;AoA6_D8_V2_mean(i)*MF],...
[AoA2_D8_V3_mean(i)*MF;AoA4_D8_V3_mean(i)*MF;AoA6_D8_V3_mean(i)*MF],...
[AoA2_D8_V4_mean(i)*MF;AoA4_D8_V4_mean(i)*MF;AoA6_D8_V4_mean(i)*MF])

i = 2; % CL
table([AoA2_D12_V2_mean(i);AoA4_D12_V2_mean(i);AoA6_D12_V2_mean(i)],...
[AoA2_D12_V3_mean(i);AoA4_D12_V3_mean(i);AoA6_D12_V3_mean(i)],...
[AoA2_D12_V4_mean(i);AoA4_D12_V4_mean(i);AoA6_D12_V4_mean(i)],...
[AoA2_D8_V2_mean(i);AoA4_D8_V2_mean(i);AoA6_D8_V2_mean(i)],...
[AoA2_D8_V3_mean(i);AoA4_D8_V3_mean(i);AoA6_D8_V3_mean(i)],...
[AoA2_D8_V4_mean(i);AoA4_D8_V4_mean(i);AoA6_D8_V4_mean(i)])

i = 3; % Drag
table([AoA2_D12_V2_mean(i);AoA4_D12_V2_mean(i)*MF;AoA6_D12_V2_mean(i)*MF],...
[AoA2_D12_V3_mean(i)*MF;AoA4_D12_V3_mean(i)*MF;AoA6_D12_V3_mean(i)*MF],...
[AoA2_D12_V4_mean(i)*MF;AoA4_D12_V4_mean(i)*MF;AoA6_D12_V4_mean(i)*MF],...
[AoA2_D8_V2_mean(i)*MF;AoA4_D8_V2_mean(i)*MF;AoA6_D8_V2_mean(i)*MF],...
[AoA2_D8_V3_mean(i)*MF;AoA4_D8_V3_mean(i)*MF;AoA6_D8_V3_mean(i)*MF],...
[AoA2_D8_V4_mean(i)*MF;AoA4_D8_V4_mean(i)*MF;AoA6_D8_V4_mean(i)*MF])
```

```
i = 4; % CL
table([AoA2_D12_V2_mean(i);AoA4_D12_V2_mean(i);AoA6_D12_V2_mean(i)],...
[AoA2_D12_V3_mean(i);AoA4_D12_V3_mean(i);AoA6_D12_V3_mean(i)],...
[AoA2_D12_V4_mean(i);AoA4_D12_V4_mean(i);AoA6_D12_V4_mean(i)],...
[AoA2_D8_V2_mean(i);AoA4_D8_V2_mean(i);AoA6_D8_V2_mean(i)],...
[AoA2_D8_V3_mean(i);AoA4_D8_V3_mean(i);AoA6_D8_V3_mean(i)],...
[AoA2_D8_V4_mean(i);AoA4_D8_V4_mean(i);AoA6_D8_V4_mean(i)])

%% Plot
FS = 24; % Fontsize
LW = 3;  % LineWidth
MF = 2;  % Multiplication factor (for full wing lift and drag)
MS = 20; % MarkerSize
%% Lift
i = 1;
figure(i)
% subplot(2,2,i) % For subplotting
plot(AoA,[AoA2_D8_V2_mean(i)*MF,AoA4_D8_V2_mean(i)*MF,...
AoA6_D8_V2_mean(i)*MF],'LineWidth',LW,'LineStyle',...
'-','Marker','o','Markersize',MS,'Color','#0072BD'); hold on
plot(AoA,[AoA2_D12_V2_mean(i)*MF,AoA4_D12_V2_mean(i)*MF,...
AoA6_D12_V2_mean(i)*MF],'LineWidth',LW,'LineStyle',...
'--','Marker','o','Markersize',MS,'Color','#0072BD'); hold on
plot(AoA,[AoA2_D8_V3_mean(i)*MF,AoA4_D8_V3_mean(i)*MF,...
AoA6_D8_V3_mean(i)*MF],'LineWidth',LW,'LineStyle',...
'-','Marker','*','Markersize',MS,'Color','#D95319'); hold on
plot(AoA,[AoA2_D12_V3_mean(i)*MF,AoA4_D12_V3_mean(i)*MF,...
AoA6_D12_V3_mean(i)*MF],'LineWidth',LW,'LineStyle',...
'--','Marker','*','Markersize',MS,'Color','#D95319'); hold on
plot(AoA,[AoA2_D8_V4_mean(i)*MF,AoA4_D8_V4_mean(i)*MF,...
AoA6_D8_V4_mean(i)*MF],'LineWidth',LW,'LineStyle',...
'-','Marker','+','Markersize',MS,'Color','#77AC30'); hold on
plot(AoA,[AoA2_D12_V4_mean(i)*MF,AoA4_D12_V4_mean(i)*MF,...
AoA6_D12_V4_mean(i)*MF],'LineWidth',LW,'LineStyle',...
'--','Marker','+','Markersize',MS,'Color','#77AC30'); hold on
legend('d=80 mm - V=2 m/s','d=120 mm - V=2 m/s',...
'd=80 mm - V=3 m/s','d=120 mm - V=3 m/s',...
'd=80 mm - V=4 m/s','d=120 mm - V=4 m/s',...
'Location','northwest')
grid minor
title('Lift vs. AoA')
xlabel('AoA')
ylabel('Lift (N)')
set(gca,'Fontsize',FS,'Fontweight','bold')

%% Lift coeffcient
i = 2;
figure(i) % For independent plot
% subplot(2,2,i) % For subplotting
plot(AoA,[AoA2_D8_V2_mean(i),AoA4_D8_V2_mean(i),...
AoA6_D8_V2_mean(i)],'LineWidth',LW,'LineStyle',...
'-','Marker','o','Markersize',MS,'Color','#0072BD'); hold on
plot(AoA,[AoA2_D12_V2_mean(i),AoA4_D12_V2_mean(i),...
AoA6_D12_V2_mean(i)],'LineWidth',LW,'LineStyle',...
'--','Marker','o','Markersize',MS,'Color','#0072BD'); hold on
```

```
plot(AoA,[AoA2_D8_V3_mean(i),AoA4_D8_V3_mean(i),...
AoA6_D8_V3_mean(i)],'LineWidth',LW,'LineStyle',...
'-','Marker','*','Markersize',MS,'Color','#D95319'); hold on
plot(AoA,[AoA2_D12_V3_mean(i),AoA4_D12_V3_mean(i),...
AoA6_D12_V3_mean(i)],'LineWidth',LW,'LineStyle',...
'--','Marker','*','Markersize',MS,'Color','#D95319'); hold on
plot(AoA,[AoA2_D8_V4_mean(i),AoA4_D8_V4_mean(i),...
AoA6_D8_V4_mean(i)],'LineWidth',LW,'LineStyle',...
'-','Marker','+','Markersize',MS,'Color','#77AC30'); hold on
plot(AoA,[AoA2_D12_V4_mean(i),AoA4_D12_V4_mean(i),...
AoA6_D12_V4_mean(i)],'LineWidth',LW,'LineStyle',...
'--','Marker','+','Markersize',MS,'Color','#77AC30'); hold on
legend('d=80 mm - V=2 m/s','d=120 mm - V=2 m/s',...
'd=80 mm - V=3 m/s','d=120 mm - V=3 m/s',...
'd=80 mm - V=4 m/s','d=120 mm - V=4 m/s',...
'Location','northwest')
grid minor
title('C_L vs. AoA')
xlabel('AoA')
ylabel('C_L')
set(gca,'Fontsize',FS,'Fontweight','bold')

%% Drag
i = 3;
figure(i) % For independent plot
% subplot(2,2,i) % For subplotting
plot(AoA,[AoA2_D8_V2_mean(i)*MF,AoA4_D8_V2_mean(i)*MF,...
AoA6_D8_V2_mean(i)*MF],'LineWidth',LW,'LineStyle',...
'-','Marker','o','Markersize',MS,'Color','#0072BD'); hold on
plot(AoA,[AoA2_D12_V2_mean(i)*MF,AoA4_D12_V2_mean(i)*MF,...
AoA6_D12_V2_mean(i)*MF],'LineWidth',LW,'LineStyle',...
'--','Marker','o','Markersize',MS,'Color','#0072BD'); hold on
plot(AoA,[AoA2_D8_V3_mean(i)*MF,AoA4_D8_V3_mean(i)*MF,...
AoA6_D8_V3_mean(i)*MF],'LineWidth',LW,'LineStyle',...
'-','Marker','*','Markersize',MS,'Color','#D95319'); hold on
plot(AoA,[AoA2_D12_V3_mean(i)*MF,AoA4_D12_V3_mean(i)*MF,...
AoA6_D12_V3_mean(i)*MF],'LineWidth',LW,'LineStyle',...
'--','Marker','*','Markersize',MS,'Color','#D95319'); hold on
plot(AoA,[AoA2_D8_V4_mean(i)*MF,AoA4_D8_V4_mean(i)*MF,...
AoA6_D8_V4_mean(i)*MF],'LineWidth',LW,'LineStyle',...
'-','Marker','+','Markersize',MS,'Color','#77AC30'); hold on
plot(AoA,[AoA2_D12_V4_mean(i)*MF,AoA4_D12_V4_mean(i)*MF,...
AoA6_D12_V4_mean(i)*MF],'LineWidth',LW,'LineStyle',...
'--','Marker','+','Markersize',MS,'Color','#77AC30'); hold on
legend('d=80 mm - V=2 m/s','d=120 mm - V=2 m/s',...
'd=80 mm - V=3 m/s','d=120 mm - V=3 m/s',...
'd=80 mm - V=4 m/s','d=120 mm - V=4 m/s',...
'Location','northwest')
grid minor
title('Drag vs. AoA')
xlabel('AoA')
ylabel('Drag (N)')
set(gca,'Fontsize',FS,'Fontweight','bold')

%% Drag coeffcient
i = 4;
```

```
figure(i) % For independent plot
% subplot(2,2,i) % For subplotting
plot(AoA,[AoA2_D8_V2_mean(i),AoA4_D8_V2_mean(i),...
AoA6_D8_V2_mean(i)],'LineWidth',LW,'LineStyle',...
'-','Marker','o','Markersize',MS,'Color','#0072BD'); hold on
plot(AoA,[AoA2_D12_V2_mean(i),AoA4_D12_V2_mean(i),...
AoA6_D12_V2_mean(i)],'LineWidth',LW,'LineStyle',...
'--','Marker','o','Markersize',MS,'Color','#0072BD'); hold on
plot(AoA,[AoA2_D8_V3_mean(i),AoA4_D8_V3_mean(i),...
AoA6_D8_V3_mean(i)],'LineWidth',LW,'LineStyle',...
'-','Marker','*','Markersize',MS,'Color','#D95319'); hold on
plot(AoA,[AoA2_D12_V3_mean(i),AoA4_D12_V3_mean(i),...
AoA6_D12_V3_mean(i)],'LineWidth',LW,'LineStyle',...
'--','Marker','*','Markersize',MS,'Color','#D95319'); hold on
plot(AoA,[AoA2_D8_V4_mean(i),AoA4_D8_V4_mean(i),...
AoA6_D8_V4_mean(i)],'LineWidth',LW,'LineStyle',...
'-','Marker','.','Markersize',MS,'Color','#77AC30'); hold on
plot(AoA,[AoA2_D12_V4_mean(i),AoA4_D12_V4_mean(i),...
AoA6_D12_V4_mean(i)],'LineWidth',LW,'LineStyle',...
'--','Marker','.','Markersize',MS,'Color','#77AC30'); hold on
legend('d=80 mm - V=2 m/s','d=120 mm - V=2 m/s',...
'd=80 mm - V=3 m/s','d=120 mm - V=3 m/s',...
'd=80 mm - V=4 m/s','d=120 mm - V=4 m/s',...
'Location','northwest')
grid minor
title('C_D vs. AoA')
xlabel('AoA')
ylabel('C_D')
set(gca,'Fontsize',FS,'Fontweight','bold')

%% Comparison between CFD and experimental results
close all
FS = 24;
LW = 3;
MS = 12;
V = [2,3,4];
% 6 deg
exp_L_AoA6_D12 = [18.02,41.84,77.07];
exp_L_AoA6_D8 = [15.75,38.34,71.69];
exp_CL_AoA6_D12 = [0.282 0.291 0.301];
exp_CL_AoA6_D8 = [0.246 0.266 0.280];
exp_D_AoA6_D12 = [3.85 8.31 14.93];
exp_D_AoA6_D8 = [3.61 7.67 13.83];
exp_CD_AoA6_D12 = [0.060 0.058 0.058 ];
exp_CD_AoA6_D8 = [0.056 0.053 0.054];

%%
i= 1;
figure(i)
% subplot(2,2,i) % Lift
plot(V,exp_L_AoA6_D8,'LineWidth',LW,'LineStyle',...
'-','Marker','+','Markersize',MS,'Color','#0072BD'); hold on

plot(V,[AoA6_D8_V2_mean(i)*MF,AoA6_D8_V3_mean(i)*MF,...
        AoA6_D8_V4_mean(i)*MF],'LineWidth',LW,'LineStyle',...
'--','Marker','o','Markersize',MS,'Color','#0072BD'); hold on
```

```
plot(V,exp_L_AoA6_D12,'LineWidth',LW,'LineStyle',...
'-','Marker','+','Markersize',MS,'Color','#D95319'); hold on

plot(V,[AoA6_D12_V2_mean(i)*MF,AoA6_D12_V3_mean(i)*MF,...
        AoA6_D12_V4_mean(i)*MF],'LineWidth',LW,'LineStyle',...
'--','Marker','o','Markersize',MS,'Color','#D95319'); hold on

legend('d=80 mm - exp','d=80 mm - cfd',...
       'd=120mm - exp','d=120mm - cfd',...
       'Location','northwest')
grid minor
title('CFD/experimental 6 deg results comparison: Lift vs. velocity')
xlabel('Velocity (m/s)')
ylabel('Lift (N)')
set(gca,'Fontsize',FS,'Fontweight','bold')
%%
i= 2;
figure(i)
% subplot(2,2,i) % Lift coefficient
plot(V,exp_CL_AoA6_D8,'LineWidth',LW,'LineStyle',...
'-','Marker','+','Markersize',MS,'Color','#0072BD'); hold on

plot(V,[AoA6_D8_V2_mean(i),AoA6_D8_V3_mean(i),...
        AoA6_D8_V4_mean(i)],'LineWidth',LW,'LineStyle',...
'--','Marker','o','Markersize',MS,'Color','#0072BD'); hold on

plot(V,exp_CL_AoA6_D12,'LineWidth',LW,'LineStyle',...
'-','Marker','+','Markersize',MS,'Color','#D95319'); hold on

plot(V,[AoA6_D12_V2_mean(i),AoA6_D12_V3_mean(i),...
        AoA6_D12_V4_mean(i)],'LineWidth',LW,'LineStyle',...
'--','Marker','o','Markersize',MS,'Color','#D95319'); hold on

legend('d=80 mm - exp','d=80 mm - cfd',...
       'd=120mm - exp','d=120mm - cfd',...
       'Location','northwest')
grid minor
title('CFD/experimental 6 deg results comparison: C_L vs. velocity')
xlabel('Velocity (m/s)')
ylabel('C_L (-)')
set(gca,'Fontsize',FS,'Fontweight','bold')
%%
i= 3;
figure(i)
% subplot(2,2,i) % drag
plot(V,exp_D_AoA6_D8,'LineWidth',LW,'LineStyle',...
'-','Marker','+','Markersize',MS,'Color','#0072BD'); hold on

plot(V,[AoA6_D8_V2_mean(i)*MF,AoA6_D8_V3_mean(i)*MF,...
        AoA6_D8_V4_mean(i)*MF],'LineWidth',LW,'LineStyle',...
'--','Marker','o','Markersize',MS,'Color','#0072BD'); hold on

plot(V,exp_D_AoA6_D12,'LineWidth',LW,'LineStyle',...
'-','Marker','+','Markersize',MS,'Color','#D95319'); hold on
```

```
plot(V,[AoA6_D12_V2_mean(i)*MF,AoA6_D12_V3_mean(i)*MF,...
        AoA6_D12_V4_mean(i)*MF],'LineWidth',LW,'LineStyle',...
'--','Marker','o','Markersize',MS,'Color','#D95319'); hold on

legend('d=80 mm - exp','d=80 mm - cfd',...
       'd=120mm - exp','d=120mm - cfd',...
       'Location','northwest')
grid minor
title('CFD/experimental 6 deg results comparison: Drag vs. velocity')
xlabel('Velocity (m/s)')
ylabel('Drag (N)')
set(gca,'Fontsize',FS,'Fontweight','bold')
%%
i= 4;
figure(i)
% subplot(2,2,i) % drag coefficient
plot(V,exp_CD_AoA6_D8,'LineWidth',LW,'LineStyle',...
'-','Marker','+','Markersize',MS,'Color','#0072BD'); hold on

plot(V,[AoA6_D8_V2_mean(i),AoA6_D8_V3_mean(i),...
        AoA6_D8_V4_mean(i)],'LineWidth',LW,'LineStyle',...
'--','Marker','o','Markersize',MS,'Color','#0072BD'); hold on

plot(V,exp_CD_AoA6_D12,'LineWidth',LW,'LineStyle',...
'-','Marker','+','Markersize',MS,'Color','#D95319'); hold on

plot(V,[AoA6_D12_V2_mean(i),AoA6_D12_V3_mean(i),...
        AoA6_D12_V4_mean(i)],'LineWidth',LW,'LineStyle',...
'--','Marker','o','Markersize',MS,'Color','#D95319'); hold on

legend('d=80 mm - exp','d=80 mm - cfd',...
       'd=120mm - exp','d=120mm - cfd',...
       'Location','northwest')
grid minor
title('CFD/experimental 6 deg results comparison: C_D vs. velocity')
xlabel('Velocity (m/s)')
ylabel('C_D (-)')
set(gca,'Fontsize',FS,'Fontweight','bold')
```

Table F.5: CFD simulation lift results of wing with strut

	Lift (N)					
	Depth : 120 mm			Depth : 80 mm		
AoA (deg)	2 m/s	3 m/s	4 m/s	2 m/s	3 m/s	4 m/s
2	1.73	2.37	1.21	2.97	2.16	1.17
4	9.68	16.50	25.51	8.88	15.86	24.95
6	15.70	30.93	52.70	14.70	29.93	51.50

Table F.6: CFD simulation drag results of wing with strut

	Drag (N)					
	Depth : 120 mm			Depth : 80 mm		
AoA (deg)	2 m/s	3 m/s	4 m/s	2 m/s	3 m/s	4 m/s
2	1.69	7.31	12.64	3.15	6.86	11.87
4	3.67	7.95	13.71	3.43	7.40	12.80
6	4.13	8.91	15.47	3.83	8.32	14.46

Table F.7: CFD simulation lift coefficient results of wing with strut

	C_L					
	Depth : 120 mm			Depth : 80 mm		
AoA (deg)	2 m/s	3 m/s	4 m/s	2 m/s	3 m/s	4 m/s
2	0.054	0.016	0.005	0.046	0.015	0.005
4	0.152	0.115	0.100	0.140	0.110	0.098
6	0.246	0.215	0.206	0.230	0.208	0.202

Table F.8: CFD simulation drag coefficient results of wing with strut

	C_D					
	Depth : 120 mm			Depth : 80 mm		
AoA (deg)	2 m/s	3 m/s	4 m/s	2 m/s	3 m/s	4 m/s
2	0.053	0.051	0.050	0.049	0.048	0.046
4	0.058	0.055	0.054	0.054	0.051	0.050
6	0.065	0.062	0.061	0.060	0.058	0.057

F.4 Front wing with strut - Waves

```
clc
clear all
close all
% This script analyses the data from the CFD wave comparison simulation
% performed on the 26-05-2022.
%% Data
% All data are extracted independently the .sim file
% The csv file is set up: Lift(1), CL(2), Drag(3), CD(4)
```

```
Waves_AoA12_D8_V3 = importdata('Waves_AoA12_D8_V3.csv');

%% Clean up
val_cl = 3000; % Clean up point

Waves_AoA12_D8_V3 = Waves_AoA12_D8_V3([end-val_cl:end],:);
Waves_AoA12_D8_V3_mean = mean(Waves_AoA12_D8_V3);

%% Table
MF = 2;  % Multiplication factor (for full wing lift and drag)
table([Waves_AoA12_D8_V3_mean(1)*MF,Waves_AoA12_D8_V3_mean(2),...
       Waves_AoA12_D8_V3_mean(3)*MF,Waves_AoA12_D8_V3_mean(4)])
```

G

Star CCM+ Macro for PID setup

```
package macro;
import java.io.*;
import java.util.*;
import java.text.SimpleDateFormat;
import java.lang.Math;
import star.common.*;
import star.base.neo.*;
import star.meshing.*;
import star.vis.*;
import star.base.report.*;
import star.sixdof.*;
import star.flow.*;

public class singlePid extends StarMacro {

public void execute() {

    // Get simulation handle
    Simulation simulation_0 = getActiveSimulation();

    // Get simulation file name
    String cname = simulation_0.getPresentationName();

    // Initialize solution
    Solution solution_0 = simulation_0.getSolution();
        solution_0.initializeSolution();

    // Get report handles for PID controller
    ExpressionReport oldLiftCoefficientErrorReport = ((ExpressionReport)...
    simulation_0.getReportManager().getReport("old_error_lift"));
    ExpressionReport liftCoefficientErrorReport = ((ExpressionReport)...
    simulation_0.getReportManager().getReport("error_lift"));

    // Set oldLiftCoefficientErrorReport to 0 for initialisation
    oldLiftCoefficientErrorReport.setDefinition(Double.toString(0));

        // Define timeCrit for stopping at certain time
    boolean timeCrit;

    // Run simulation while not converged
    do {
            // Step simulation
```

```
        simulation_0.getSimulationIterator().step(1);

        // Save old pitch error value
        oldLiftCoefficientErrorReport.setDefinition ...
        (Double.toString(liftCoefficientErrorReport.getReportMonitorValue()));

            // Check for convergence
            timeCrit = simulation_0.getSolverStoppingCriterionManager() ...
            .getSolverStoppingCriterion("Maximum Physical Time").getIsSatisfied();

    }
    while (!timeCrit);
    }
}
```

H

Data analysis - Experimental results

H.1 Bare hull

```
%% Drag of the bare hull
clc
clear all
close all
% Data extraction
% 2m/s with bare hull
data=hdf5info(['TOW-Proj19830907-Ser001-Test003-Run006.hdf5']);

Drag=hdf5read(data.GroupHierarchy.Groups(1).Datasets(2));
Time=hdf5read(data.GroupHierarchy.Groups(7).Datasets(1));
Speed=hdf5read(data.GroupHierarchy.Groups(1).Datasets(3));

%selecting relevant values
Drag=Drag(1200:size(Drag));
Time4=Time(1200:size(Time))-Time(1200);

% 3m/s with bare hull
data1=hdf5info(['TOW-Proj19830907-Ser001-Test003-Run007.hdf5']);

Drag1=hdf5read(data1.GroupHierarchy.Groups(1).Datasets(2));
Time1=hdf5read(data1.GroupHierarchy.Groups(7).Datasets(1));
Speed1=hdf5read(data1.GroupHierarchy.Groups(1).Datasets(3));


% 4m/s with bare hull
data2=hdf5info(['TOW-Proj19830907-Ser001-Test003-Run008.hdf5']);

Drag2=hdf5read(data2.GroupHierarchy.Groups(1).Datasets(2));
Time2=hdf5read(data2.GroupHierarchy.Groups(7).Datasets(1));
Speed2=hdf5read(data2.GroupHierarchy.Groups(1).Datasets(3));

%selecting relevant values
Drag2=Drag2(1200:size(Drag2));
Time2=Time2(1200:size(Time2))-Time(1200);

% 5m/s with bare hull
data3=hdf5info(['TOW-Proj19830907-Ser001-Test003-Run009.hdf5']);
```

```
Drag3=hdf5read(data3.GroupHierarchy.Groups(1).Datasets(2));
Time3=hdf5read(data3.GroupHierarchy.Groups(7).Datasets(1));
Speed3=hdf5read(data3.GroupHierarchy.Groups(1).Datasets(3));

% Determination of the means

%Drag
Mean_Drag = mean(Drag);
Mean_Drag_1 = mean(Drag1);
Mean_Drag_2 = mean(Drag2);
Mean_Drag_3 = mean(Drag3);

%Creation arrays means
MD=[];
MD1=[];
MD2=[];
MD3=[];
i=0;
for i=1:size(Time)
    MD(i)=Mean_Drag;
    MD1(i)=Mean_Drag_1;
    MD2(i)=Mean_Drag_2;
    MD3(i)=Mean_Drag_3;
end
% Plotting
%Drag
figure(6)
plot(Time4, Drag,'LineWidth',2); hold on
plot(Time1, Drag1,'LineWidth',2); hold on
plot(Time2, Drag2,'LineWidth',2); hold on
plot(Time3, Drag3,'LineWidth',2); hold on
plot(Time,MD,'color','k','Linewidth',1.5); hold on
plot(Time,MD1,'color','k','Linewidth',1.5); hold on
plot(Time,MD2,'color','k','Linewidth',1.5); hold on
plot(Time,MD3,'color','k','Linewidth',1.5); hold on
title('Resistance - bare hull');
legend('2m/s','3m/s','4m/s', '5m/s');
xlabel('Time (s)');
ylabel('Drag (N)'); hold on
set(gca,'FontSize',24,'FontWeight','bold')
grid minor
```

H.2 Bare hull with rudder

```
%% Tow with rudder
clc
clear all
close all
% Data extraction
data5=hdf5info(['TOW-Proj19830907-Ser001-Test003-Run005.hdf5']);

Drag5=hdf5read(data5.GroupHierarchy.Groups(1).Datasets(2));
```

```
Time5=hdf5read(data5.GroupHierarchy.Groups(7).Datasets(1));

%selcting relevant values
Drag5=Drag5(1200:size(Drag5));
Time5=Time5(1200:size(Time5))-Time5(1200);

% Taking the mean
Mean_Drag5=mean(Drag5);

for i=1:size(Time5)
    MD5(i)=Mean_Drag5;
end
% Plotting
figure(5)
plot(Time5, Drag5,'LineWidth',2); hold on
plot(Time5,MD5,'color','k','Linewidth',1.5); hold on
title('Resistance - bare hull and rudder w. motors ');
legend('Drag');
xlabel('Time (s)');
ylabel('Drag (N)'); hold on
set(gca,'FontSize',24,'FontWeight','bold')
grid minor
```

H.3 Bollard pull test with dual thruster setup

```
clc
clear all
close all
% Data extraction
data=hdf5info(['TOW-Proj19830907-Ser001-Test003-Run004.hdf5']);
Thrust4=hdf5read(data.GroupHierarchy.Groups(1).Datasets(2));
Time4=hdf5read(data.GroupHierarchy.Groups(7).Datasets(1));

% Taking the mean
Mean_Thrust4=mean(Thrust4);

%for i=1:size(Time)
 %   MT(i)=Mean_Thrust;
%end

% Plotting
figure(4)
plot(Time4, Thrust4,'LineWidth',2); hold on
%plot(Time,MT,'color','k','Linewidth',1.5); hold on
title('Bollard pull - dual thruster setup ');
legend('Thrust');
xlabel('Time (s)');
ylabel('Thrust (N)'); hold on
set(gca,'FontSize',24,'FontWeight','bold')
grid minor
```

H.4 Data sets from towing tank tests

Table H.1: Data sets from towing tank test of front wing

Data set	AoA (deg)	Speed (m/s)	Depth (mm)
Calm Water			
TOW-Proj40209757-Ser001-Test001-Run001.hdf5	Calibration		
TOW-Proj40209757-Ser001-Test001-Run002.hdf5	5.94	2	120
TOW-Proj40209757-Ser001-Test001-Run003.hdf5	5.94	3	120
TOW-Proj40209757-Ser001-Test001-Run004.hdf5	5.94	4	120
TOW-Proj40209757-Ser001-Test001-Run005.hdf5	Calibration		
TOW-Proj40209757-Ser001-Test001-Run006.hdf5	5.94	2	80
TOW-Proj40209757-Ser001-Test001-Run007.hdf5	5.94	3	80
TOW-Proj40209757-Ser001-Test001-Run008.hdf5	5.94	4	80
TOW-Proj40209757-Ser001-Test001-Run009.hdf5	3.17	2	120
TOW-Proj40209757-Ser001-Test001-Run010.hdf5	3.17	3	120
TOW-Proj40209757-Ser001-Test001-Run011.hdf5	3.17	4	120
TOW-Proj40209757-Ser001-Test001-Run012.hdf5	3.17	2	80
TOW-Proj40209757-Ser001-Test001-Run013.hdf5	3.17	3	80
TOW-Proj40209757-Ser001-Test001-Run014.hdf5	3.17	4	80
TOW-Proj40209757-Ser001-Test001-Run015.hdf5	7.49	2	120
TOW-Proj40209757-Ser001-Test001-Run016.hdf5	7.49	3	120
TOW-Proj40209757-Ser001-Test001-Run017.hdf5	7.49	4	120
TOW-Proj40209757-Ser001-Test001-Run018.hdf5	7.49	2	80
TOW-Proj40209757-Ser001-Test001-Run019.hdf5	7.49	3	80
TOW-Proj40209757-Ser001-Test001-Run020.hdf5	7.49	4	80
TOW-Proj40209757-Ser001-Test001-Run021.hdf5	9.28	2	120
TOW-Proj40209757-Ser001-Test001-Run022.hdf5	9.28	3	120
TOW-Proj40209757-Ser001-Test001-Run023.hdf5	9.28	4	120
TOW-Proj40209757-Ser001-Test001-Run024.hdf5	9.28	2	80
TOW-Proj40209757-Ser001-Test001-Run025.hdf5	9.28	3	80
TOW-Proj40209757-Ser001-Test001-Run026.hdf5	9.28	4	80
TOW-Proj40209757-Ser001-Test001-Run027.hdf5	12.02	2	120
TOW-Proj40209757-Ser001-Test001-Run028.hdf5	12.02	3	120
TOW-Proj40209757-Ser001-Test001-Run029.hdf5	12.02	4	120
TOW-Proj40209757-Ser001-Test001-Run030.hdf5	12.02	2	80
TOW-Proj40209757-Ser001-Test001-Run031.hdf5	12.02	3	80
TOW-Proj40209757-Ser001-Test001-Run032.hdf5	12.02	4	80
TOW-Proj40209757-Ser001-Test001-Run033.hdf5	0.34	2	120
TOW-Proj40209757-Ser001-Test001-Run034.hdf5	0.34	3	120
TOW-Proj40209757-Ser001-Test001-Run035.hdf5	0.34	4	120
TOW-Proj40209757-Ser001-Test001-Run036.hdf5	0.34	2	80
TOW-Proj40209757-Ser001-Test001-Run037.hdf5	0.34	3	80
TOW-Proj40209757-Ser001-Test001-Run038.hdf5	0.34	4	80
Wave test			
TOW-Proj40209757-Ser001-Test001-Run039.hdf5	12.02	3	80
TOW-Proj40209757-Ser001-Test001-Run040.hdf5	12.02	3	80

H.5 Front wing towing tank test - Calm water

```
clc
clear all
close all

% Data extraction

data1=hdf5info(['TOW-Proj40209757-Ser001-Test001-Run002.hdf5']);
Drag1=hdf5read(data1.GroupHierarchy.Groups(3).Datasets(1));
Lift1=hdf5read(data1.GroupHierarchy.Groups(3).Datasets(2));
Time1=hdf5read(data1.GroupHierarchy.Groups(5).Datasets(1));
Speed1=hdf5read(data1.GroupHierarchy.Groups(1).Datasets(1));


data2=hdf5info(['TOW-Proj40209757-Ser001-Test001-Run003.hdf5']);
Drag2=hdf5read(data2.GroupHierarchy.Groups(3).Datasets(1));
Lift2=hdf5read(data2.GroupHierarchy.Groups(3).Datasets(2));
Time2=hdf5read(data2.GroupHierarchy.Groups(5).Datasets(1));
Speed2=hdf5read(data2.GroupHierarchy.Groups(1).Datasets(1));

data3=hdf5info(['TOW-Proj40209757-Ser001-Test001-Run004.hdf5']);
Drag3=hdf5read(data3.GroupHierarchy.Groups(3).Datasets(1));
Lift3=hdf5read(data3.GroupHierarchy.Groups(3).Datasets(2));
Time3=hdf5read(data3.GroupHierarchy.Groups(5).Datasets(1));
Speed3=hdf5read(data3.GroupHierarchy.Groups(1).Datasets(1));

% Determination of the means
%Drag
Mean_Drag_1 = mean(Drag1);
Mean_Drag_2 = mean(Drag2);
Mean_Drag_3 = mean(Drag3);
%Lift
Mean_Lift_1 = mean(Lift1);
Mean_Lift_2 = mean(Lift2);
Mean_Lift_3 = mean(Lift3);
%Creation arrays means
MD1=[];
MD2=[];
MD3=[];
ML1=[];
ML2=[];
ML3=[];
i=0;
for i=1:size(Time1)
    MD1(i)=Mean_Drag_1;
    MD2(i)=Mean_Drag_2;
    MD3(i)=Mean_Drag_3;
    ML1(i)=Mean_Lift_1;
    ML2(i)=Mean_Lift_2;
    ML3(i)=Mean_Lift_3;
end
```

```
% Plotting
%Drag
figure(1)
plot(Time1, Drag1); hold on
plot(Time2, Drag2); hold on
plot(Time3, Drag3); hold on
plot(Time1,MD1,'color','k','Linewidth',1.5); hold on
plot(Time1,MD2,'color','k','Linewidth',1.5); hold on
plot(Time1,MD3,'color','k','Linewidth',1.5); hold on
title('Drag: depth=12cm ,  ');
legend('2m/s','3m/s','4m/s');
xlabel('Time (s)');
ylabel('Drag (N)'); hold on
%Lift
figure(2)
plot(Time1, Lift1); hold on
plot(Time2, Lift2); hold on
plot(Time3, Lift3); hold on
plot(Time1,ML1,'color','k','Linewidth',1.5); hold on
plot(Time1,ML2,'color','k','Linewidth',1.5); hold on
plot(Time1,ML3,'color','k','Linewidth',1.5); hold on
title('Lift: d=12cm , h=44.74mm ');
legend('2m/s','3m/s','4m/s')
xlabel('Time (s)')
ylabel('Lift (N)')
```

H.6 Front wing towing tank test - Waves

```
%% Time adaptation for wave results
clc
clear all
close all
% Data extraction

%data=hdf5info(['TOW-Proj40209757-Ser001-Test001-Run039.hdf5']);
data=hdf5info(['TOW-Proj40209757-Ser001-Test001-Run040.hdf5']);
Drag=hdf5read(data.GroupHierarchy.Groups(3).Datasets(1));
Lift=hdf5read(data.GroupHierarchy.Groups(3).Datasets(2));
Time=hdf5read(data.GroupHierarchy.Groups(5).Datasets(1));
Speed=hdf5read(data.GroupHierarchy.Groups(1).Datasets(1));

%Reduction of data set
D=Drag(275:size(Drag));
L=Lift(275:size(Lift));
T=Time(275:size(Time));
S=Speed(275:size(Speed));

% Determination of the means
%Drag
Mean_Drag = mean(D);
%Lift
Mean_Lift = mean(L);
```

```
% Speed
Mean_Speed = mean(Speed);
%Creation arrays means
MD=[];
ML=[];
MS=[];
i=0;
for i=1:size(Time)
    MD(i)=Mean_Drag;
    MS(i)=Mean_Speed;
    ML(i)=Mean_Lift;
end
% Plotting
%Lift
figure(1)
subplot(2,1,1)
plot(T, L,'Linewidth',3); hold on
plot(Time,ML,'color','k','Linewidth',3); hold on
grid minor
title('Lift: depth=80mm , AoA=12.02deg ');
set(gca,'FontSize',24,'FontWeight','bold')
legend('3m/s')
xlabel('Time (s)')
ylabel('Lift (N)')
%Drag
subplot(2,1,2)
plot(T, D,'Linewidth',3); hold on
plot(Time,MD, 'color','k','Linewidth',3); hold on
grid minor
title('Drag: depth=80mm , AoA=12.02deg ');
set(gca,'FontSize',24,'FontWeight','bold')
legend('3m/s');
xlabel('Time (s)');
ylabel('Drag (N)'); hold on
```

H.7 Sonar study

```
clc
clear all
close all
% Data analysis of the sonar study. Test setup done independently
% of SSPA's carriage.
% Sonar connected to Mission Planner (MP) and data extracted from MP.

%% Data
% Calm water
sonar_calm_water_data = load('calm water.tlog.mat');
sonar_calm_water = ...
timeseries(sonar_calm_water_data.distance_mavlink_rangefinder_t([21:end],2),...
        [sonar_calm_water_data.distance_mavlink_rangefinder_t([21:end],1)-...
        sonar_calm_water_data.distance_mavlink_rangefinder_t(21,1)]*...
        10^3*60);
```

```
mean_sonar_calm_water = mean(sonar_calm_water);

% Waves #1
sonar_waves_1 = load('sonar in waves 1.tlog.mat');
sonar_waves_1 =...
timeseries(sonar_waves_1.distance_mavlink_rangefinder_t(:,2),...
        [sonar_waves_1.distance_mavlink_rangefinder_t(:,1)-...
        sonar_waves_1.distance_mavlink_rangefinder_t(1,1)]*10^3*60);
mean_sonar_waves_1 = mean(sonar_waves_1);

% Waves #2
sonar_waves_2 = load('sonar in waves 2.tlog.mat');
sonar_waves_2 =...
timeseries(sonar_waves_2.distance_mavlink_rangefinder_t([21:end],2),...
        [sonar_waves_2.distance_mavlink_rangefinder_t([21:end],1)-...
        sonar_waves_2.distance_mavlink_rangefinder_t(21,1)]*10^3*60);
mean_sonar_waves_2 = mean(sonar_waves_2);

%% Plotting
LW = 3; % Line Width
FS = 24; % Font size

figure(1)
plot(sonar_calm_water,'LineWidth',LW)
hold on
yline(mean_sonar_calm_water,'Color','k','LineWidth',LW)
grid minor
ylabel('Distance to water surface (m)')
set(gca,'FontSize',FS,'FontWeight','bold')
title('Sonar reading - Calm water')

figure(2)
subplot(2,1,1)
plot(sonar_waves_1,'LineWidth',LW)
hold on
yline(mean_sonar_waves_1,'Color','k','LineWidth',LW)
grid minor
ylabel('Distance (m)')
set(gca,'FontSize',FS,'FontWeight','bold')
title('Sonar reading - Waves #1')
subplot(2,1,2)
plot(sonar_waves_2,'LineWidth',LW)
hold on
yline(mean_sonar_waves_2,'Color','k','LineWidth',LW)
grid minor
ylabel('Distance (m)')
set(gca,'FontSize',FS,'FontWeight','bold')
title('Sonar reading - Waves #2')
```

H.8 Field test - Manual flight mode

```
clc
```

```
close all
clear all
format shorte
% This file analyses the data from the field test done on 17-05-2022 of
% the foiling boat for the manual flight mode.

%% Data
load('2022-05-17 14-28-35.tlog.mat')

% Velocity
vel = vel_mavlink_gps_raw_int_t(:,2);
vel = timeseries(vel/100, ...
    [vel_mavlink_gps_raw_int_t(:,1)-...
    vel_mavlink_gps_raw_int_t(1,1)]*10^3*60);

% Throttle
throttle =...
timeseries(servo1_raw_mavlink_servo_output_raw_t(:,2), ...
    [servo1_raw_mavlink_servo_output_raw_t(:,1)-...
    servo1_raw_mavlink_servo_output_raw_t(1,1)]*10^3*60);

% Left elevon
left_elevon =...
timeseries(servo5_raw_mavlink_servo_output_raw_t(:,2), ...
    [servo5_raw_mavlink_servo_output_raw_t(:,1)-...
    servo5_raw_mavlink_servo_output_raw_t(1,1)]*10^3*60);

% Right elevon
right_elevon =...
timeseries(servo6_raw_mavlink_servo_output_raw_t(:,2), ...
    [servo6_raw_mavlink_servo_output_raw_t(:,1)-...
    servo6_raw_mavlink_servo_output_raw_t(1,1)]*10^3*60);

% Elevator
elevator =...
timeseries(servo2_raw_mavlink_servo_output_raw_t(:,2), ...
    [servo2_raw_mavlink_servo_output_raw_t(:,1)-...
    servo2_raw_mavlink_servo_output_raw_t(1,1)]*10^3*60);

% Roll
roll_rad = roll_mavlink_attitude_t(:,2);
roll_deg = timeseries(roll_rad * 180/pi, ...
    [roll_mavlink_attitude_t(:,1)-...
    roll_mavlink_attitude_t(1,1)]*10^3*60);

% Pitch
pitch_rad = pitch_mavlink_attitude_t(:,2);
pitch_deg = timeseries(pitch_rad * 180/pi, ...
    [pitch_mavlink_attitude_t(:,1)-...
    pitch_mavlink_attitude_t(1,1)]*10^3*60);


%% Plotting
LW = 3; % Line Width
FS = 24; % Font size
```

```
% Velocity
figure(1)
subplot(2,1,1)
plot(vel,'LineWidth',LW)
hold on
title('Velocity')
ylabel('Velocity (m/s)')
grid minor
set(gca,'FontSize',FS,'FontWeight','bold')

subplot(2,1,2)
plot(throttle,'LineWidth',LW)
hold on
title('Throttle pulsations')
ylabel('Pulses (μs)')
grid minor
set(gca,'FontSize',FS,'FontWeight','bold')

% Motions
figure(2)
subplot(2,1,1)
plot(roll_deg,'LineWidth',LW)
hold on
plot(pitch_deg,'LineWidth',LW)
hold on
yline(0,'Color','k','LineWidth',LW)
title('Pitch and roll angle')
ylabel('Angle (deg)')
grid minor
legend('Roll','Pitch','Location','best')
set(gca,'FontSize',FS,'FontWeight','bold')

subplot(2,1,2)
plot(left_elevon,'LineWidth',LW)
hold on
plot(right_elevon,'LineWidth',LW)
hold on
plot(elevator,'LineWidth',LW)
title('Elevon and elevator pulsations')
ylabel('Pulses (μs)')
grid minor
legend('Left elevon', 'Right elevon','Elevator','Location','best')
set(gca,'FontSize',FS,'FontWeight','bold')
```

H.9 Field test - Stabilization flight mode

```
clc
close all
clear all
format shorte
% This file analyses the data from the field test done on 17-05-2022 of
% the foiling boat for the stabilization flight mode.
```

```
%% Data
load('2022-05-17 14-40-24.tlog.mat')

% Velocity
vel = vel_mavlink_gps_raw_int_t([1:550],2);
vel = timeseries(vel/100, ...
    [vel_mavlink_gps_raw_int_t([1:550],1)-...
    vel_mavlink_gps_raw_int_t(1,1)]*10^3*60);

% Throttle
throttle =...
timeseries(servo1_raw_mavlink_servo_output_raw_t([1:542],2),...
    [servo1_raw_mavlink_servo_output_raw_t([1:542],1)-...
    servo1_raw_mavlink_servo_output_raw_t(1,1)]*10^3*60);

% Left elevon
left_elevon =...
timeseries(servo5_raw_mavlink_servo_output_raw_t([1:542],2),...
    [servo5_raw_mavlink_servo_output_raw_t([1:542],1)-...
    servo5_raw_mavlink_servo_output_raw_t(1,1)]*10^3*60);

% Right elevon
right_elevon =...
timeseries(servo6_raw_mavlink_servo_output_raw_t([1:542],2),...
    [servo6_raw_mavlink_servo_output_raw_t([1:542],1)-...
    servo6_raw_mavlink_servo_output_raw_t(1,1)]*10^3*60);

% Elevator
elevator =...
timeseries(servo2_raw_mavlink_servo_output_raw_t([1:542],2),...
    [servo2_raw_mavlink_servo_output_raw_t([1:542],1)-...
    servo2_raw_mavlink_servo_output_raw_t(1,1)]*10^3*60);

% Roll
roll_rad = roll_mavlink_attitude_t([1:1050],2);
roll_deg = timeseries(roll_rad * 180/pi, ...
    [roll_mavlink_attitude_t([1:1050],1)-...
    roll_mavlink_attitude_t(1,1)]*10^3*60);

% Pitch
pitch_rad = pitch_mavlink_attitude_t([1:1050],2);
pitch_deg = timeseries(pitch_rad * 180/pi, ...
    [pitch_mavlink_attitude_t([1:1050],1)-...
    pitch_mavlink_attitude_t(1,1)]*10^3*60);


%% Plotting
LW = 3; % Line Width
FS = 24; % Font size

% Velocity
figure(1)
subplot(2,1,1)
plot(vel,'LineWidth',LW)
hold on
```

```
title('Velocity')
ylabel('Velocity (m/s)')
grid minor
set(gca,'FontSize',FS,'FontWeight','bold')

subplot(2,1,2)
plot(throttle,'LineWidth',LW)
hold on
title('Throttle pulsations')
ylabel('Pulses (μs)')
grid minor
set(gca,'FontSize',FS,'FontWeight','bold')

% Motions
figure(2)
subplot(2,1,1)
plot(roll_deg,'LineWidth',LW)
hold on
plot(pitch_deg,'LineWidth',LW)
hold on
yline(0,'Color','k','LineWidth',LW)
title('Pitch and roll angle')
ylabel('Angle (deg)')
grid minor
legend('Roll','Pitch','Location','best')
set(gca,'FontSize',FS,'FontWeight','bold')

subplot(2,1,2)
plot(left_elevon,'LineWidth',LW)
hold on
plot(right_elevon,'LineWidth',LW)
hold on
plot(elevator,'LineWidth',LW)
title('Elevon and elevator pulsations')
ylabel('Pulses (μs)')
grid minor
legend('Left elevon', 'Right elevon','Elevator','Location','best')
set(gca,'FontSize',FS,'FontWeight','bold')
```

H.10 Workshop inclining test

```
clc
close all
clear all
format shorte
% This file analyses the data from the workshop inclining test done on
% 20-05-2022 of the foiling boat
%% Data - Roll Test
load('2022-05-20 08-23-14.tlog.mat'); %

% Data clean up
x_act = length(servo5_raw_mavlink_servo_output_raw_t(:,2))/2 -0.5;
```

```
x_mot = length(pitch_mavlink_attitude_t(:,2))/2 -0.5;

% Left elevon
left_elevon =...
timeseries(servo5_raw_mavlink_servo_output_raw_t([x_act:end],2),...
    [servo5_raw_mavlink_servo_output_raw_t([x_act:end],1)...
    -servo5_raw_mavlink_servo_output_raw_t(x_act,1)]*10^3*60);

% Right elevon
right_elevon =...
timeseries(servo6_raw_mavlink_servo_output_raw_t([x_act:end],2),...
    [servo6_raw_mavlink_servo_output_raw_t([x_act:end],1)...
    -servo6_raw_mavlink_servo_output_raw_t(x_act,1)]*10^3*60);

% Elevator
elevator =...
timeseries(servo2_raw_mavlink_servo_output_raw_t([x_act:end],2),...
    [servo2_raw_mavlink_servo_output_raw_t([x_act:end],1)...
    -servo2_raw_mavlink_servo_output_raw_t(x_act,1)]*10^3*60);

% Roll
roll_rad = roll_mavlink_attitude_t([x_mot:end],2);
roll_deg = timeseries(roll_rad * 180/pi, ...
    [roll_mavlink_attitude_t([x_mot:end],1)...
    -roll_mavlink_attitude_t(x_mot,1)]*10^3*60);

% Pitch
pitch_rad = pitch_mavlink_attitude_t([x_mot:end],2);
pitch_deg = timeseries(pitch_rad * 180/pi, ...
    [pitch_mavlink_attitude_t([x_mot:end],1)...
    -pitch_mavlink_attitude_t(x_mot,1)]*10^3*60);


%% Plotting
LW = 3; % Line Width
FS = 24; % Font size

% Motions
figure(1)
subplot(2,1,1)
plot(roll_deg,'LineWidth',LW)
hold on
plot(pitch_deg,'LineWidth',LW)
hold on
yline(0,'Color','k','LineWidth',LW)
title('Pitch and roll angle')
ylabel('Angle (deg)')
grid minor
legend('Roll','Pitch','Location','best')
set(gca,'FontSize',FS,'FontWeight','bold')

subplot(2,1,2)
plot(left_elevon,'LineWidth',LW)
hold on
plot(right_elevon,'LineWidth',LW)
hold on
```

```
plot(elevator,'LineWidth',LW)
title('Elevon and elevator pulsations')
ylabel('Pulses (μs)')
grid minor
legend('Left elevon', 'Right elevon','Elevator','Location','best')
set(gca,'FontSize',FS,'FontWeight','bold')

%% Data - Pitch Test
load('2022-05-20 08-36-05.tlog.mat');

% Data clean up
x_act = length(servo5_raw_mavlink_servo_output_raw_t(:,2))/4 -0.25;
x_mot = length(pitch_mavlink_attitude_t(:,2))/4 -0.25;

% Left elevon
left_elevon =...
timeseries(servo5_raw_mavlink_servo_output_raw_t([x_act:end],2),...
    [servo5_raw_mavlink_servo_output_raw_t([x_act:end],1)...
    -servo5_raw_mavlink_servo_output_raw_t(x_act,1)]*10^3*60);

% Right elevon
right_elevon =...
timeseries(servo6_raw_mavlink_servo_output_raw_t([x_act:end],2),...
    [servo6_raw_mavlink_servo_output_raw_t([x_act:end],1)...
    -servo6_raw_mavlink_servo_output_raw_t(x_act,1)]*10^3*60);

% Elevator
elevator =...
timeseries(servo2_raw_mavlink_servo_output_raw_t([x_act:end],2), ...
    [servo2_raw_mavlink_servo_output_raw_t([x_act:end],1)...
    -servo2_raw_mavlink_servo_output_raw_t(x_act,1)]*10^3*60);

% Roll
roll_rad = roll_mavlink_attitude_t([x_mot:end],2);
roll_deg = timeseries(roll_rad * 180/pi, ...
    [roll_mavlink_attitude_t([x_mot:end],1)...
    -roll_mavlink_attitude_t(x_mot,1)]*10^3*60);

% Pitch
pitch_rad = pitch_mavlink_attitude_t([x_mot:end],2);
pitch_deg = timeseries(pitch_rad * 180/pi, ...
    [pitch_mavlink_attitude_t([x_mot:end],1)...
    -pitch_mavlink_attitude_t(x_mot,1)]*10^3*60);


%% Plotting
LW = 3; % Line Width
FS = 24; % Font size

% Motions
figure(2)
subplot(2,1,1)
plot(roll_deg,'LineWidth',LW)
hold on
plot(pitch_deg,'LineWidth',LW)
hold on
```

```
yline(0,'Color','k','LineWidth',LW)
title('Pitch and roll angle')
ylabel('Angle (deg)')
grid minor
legend('Roll','Pitch','Location','best')
set(gca,'FontSize',FS,'FontWeight','bold')

subplot(2,1,2)
plot(left_elevon,'LineWidth',LW)
hold on
plot(right_elevon,'LineWidth',LW)
hold on
plot(elevator,'LineWidth',LW)
title('Elevon and elevator pulsations')
ylabel('Pulses (μs)')
grid minor
legend('Left elevon', 'Right elevon','Elevator','Location','best')
set(gca,'FontSize',FS,'FontWeight','bold')
```

I

Front wing towing tank test results

Table I.1: Mean lift value generated from towing tank test sample of the main wing at different depth

	Lift (N)					
	Depth : 120 mm			Depth : 80 mm		
AoA (deg)	2 m/s	3 m/s	4 m/s	2 m/s	3 m/s	4 m/s
0.33	0.47	2.87	5.3	-0.27	0.68	3.87
3.17	9.63	22.78	42.5	9.21	22.41	42.62
5.94	18.02	41.84	77.07	15.75	38.34	71.69
7.5	23.35	53.29	98.03	20.78	50.4	93.06
9.28	29.54	67.55	120.62	26.48	63	115.52
12.02	37.5	83.88	148.7	33.58	79.11	142

Table I.2: Calculated lift coefficients based on the towing tank tests

	Lift coefficient - C_L					
	Depth : 120 mm			Depth : 80 mm		
AoA (deg)	2m/s	3m/s	4m/s	2m/s	3m/s	4m/s
0.33	0.007	0.020	0.021	-0.004	0.005	0.015
3.17	0.150	0.158	0.166	0.144	0.156	0.166
5.94	0.282	0.291	0.301	0.246	0.266	0.280
7.5	0.365	0.370	0.383	0.325	0.35	0.364
9.28	0.462	0.469	0.471	0.414	0.437	0.451
12.02	0.586	0.582	0.581	0.525	0.549	0.555

Table I.3: Mean drag value generated from towing tank test sample of the main wing at different depth

	Drag (N)					
	Depth : 120 mm			Depth : 80 mm		
AoA (deg)	2 m/s	3 m/s	4 m/s	2 m/s	3 m/s	4 m/s
0.33	3.22	6.46	10.92	2.97	5.95	10.18
3.17	3.56	7.2	12.45	3.31	6.73	11.76
5.94	3.85	8.31	14.93	3.61	7.67	13.83
7.5	4.72	9.82	17.58	4.4	9.24	16.46
9.28	5.64	11.72	20.77	5.27	10.95	19.62
12.02	6.99	14.39	26.09	6.42	13.44	24.52

Table I.4: Calculated drag coefficients based on the towing tank tests

	Drag coefficient - C_D					
	Depth : 120 mm			Depth : 80 mm		
AoA (deg)	2 m/s	3 m/s	4 m/s	2 m/s	3 m/s	4 m/s
0.33	0.050	0.045	0.043	0.046	0.041	0.040
3.17	0.056	0.05	0.049	0.052	0.047	0.046
5.94	0.060	0.058	0.058	0.056	0.053	0.054
7.5	0.074	0.068	0.069	0.069	0.064	0.064
9.28	0.088	0.081	0.081	0.082	0.076	0.077
12.02	0.109	0.010	0.102	0.100	0.093	0.096

DEPARTMENT OF MECHANICS & MARITIME SCIENCES
CHALMERS UNIVERSITY OF TECHNOLOGY
Gothenburg, Sweden
www.chalmers.se

CHALMERS
UNIVERSITY OF TECHNOLOGY